THERMAL CONDUCTIVITY OF NUCLEAR FUEL AND ITS DEGRADATION BY PHYSICAL AND CHEMICAL BURNUP

A Thesis Submitted to the College of
Graduate and Postdoctoral Studies

In Partial Fulfillment of the Requirements
For the Degree of Master of Science

In the Department of Physics and Engineering Physics
University of Saskatchewan
Saskatoon

By

DOTUN JOHN OLADIMEJI

Permission to Use

In presenting this thesis in partial fulfillment of the requirements for a Postgraduate degree from the University of Saskatchewan, I agree that the Libraries of this University may make it freely available for inspection. I further agree that permission for copying of this thesis/dissertation in any manner, in whole or in part, for scholarly purposes may be granted by the professor or professors who supervised my thesis work or, in their absence, by the Head of the Department or the Dean of the College in which my thesis work was done. It is understood that any copying or publication or use of this thesis/dissertation or parts thereof for financial gain shall not be allowed without my written permission. It is also understood that due recognition shall be given to me and to the University of Saskatchewan in any scholarly use which may be made of any material in my thesis.

Requests for permission to copy or to make other uses of materials in this thesis/dissertation in whole or part should be addressed to:

Head of the Department of Physics and Engineering Physics,
University of Saskatchewan,
116 Science Place,
Saskatoon, Saskatchewan S7N 5E2,
Canada.

OR

The Dean
College of Graduate and Postdoctoral Studies,
University of Saskatchewan,
107 Administration Place,
Saskatoon, Saskatchewan S7N 5A2,
Canada.

Abstract

Nuclear fuel performance during reactor operation has been studied using both atomic scale simulation and experimental procedure in order to investigate how nuclear fission process affects both the physical state and the chemistry of the fuel. Attention has been drawn to the consequences of nuclear exposure after Fukushima nuclear accident, as it relates to the impact of modern reactor design and nuclear fuel performance. With the recognition of the inherent risks associated with pure uranium oxide (UO_2) fuel reactors, there is a need to study nuclear fuel with a view to highlighting their susceptibility to reactor accident, hence, developing an accident tolerant fuel. In this work, cerium oxide (CeO_2) has been deployed as a surrogate material for UO_2 fuel due to their uniquely similar physicochemical behaviors as fuel materials during operations of nuclear reactors. CeO_2 is, however, non-radioactive.

The nuclear reactor safety analysis revealed that thermal conductivity is an important property of nuclear fuel because it controls fuel operating temperature and therefore influences its safety. In line with this assertion, two key areas of focus have been identified in this investigation: i) degradation of thermal conductivity by structural and fission products in nuclear fuel and ii) the fuel microstructural evolution due to dissolved fission product. The former has been carried out using molecular dynamics (MD) simulations and analytical models over the full range of temperature of interest while the latter was carried out using both experimental procedure and MD simulations.

MD simulations of the structural and thermal properties of CeO_2 as a representative of UO_2 fuel were carried out using Large-scale Atomic/Molecular Massively Parallel Simulator (LAMMPS) code. The thermal expansion, thermal conductivity, and oxygen ion diffusion were calculated using classical ionic potential models. During these processes, verification of methods was done to establish the best potential for CeO_2. The many-body ionic potential in the Embedded Atom Method (EAM) and two-body force field potentials were used to predict lattice parameters and thermal conductivity.

Nuclear fuel efficiency changes during reactor operation because of irradiation process. Fission products like fission gas bubble, pores, cracks, dissolved and precipitated fission product buildup in the fuel matrix. The effect of physical burnup such as porosity on the thermophysical properties

of CeO_2 was simulated using a large system with thousands of atoms. Pores were induced on the large CeO_2 system by carefully removing an appropriate number of atoms in proper proportion to mimic porosity evolution. Lattice parameter and the thermal conductivity were calculated at a different percentage of porosity for CeO_2. This calculation relates the degradation of thermal conductivity with a number of pores and increasing temperature.

In irradiated oxide fuels (UO_2 and PuO_2), several fission products (FP) are produced and they take various chemical states depending on the conditions of the fuel. Some FPs dissolve as oxides in the fuel matrix. Structural and thermal properties of Ce_3ZrO_8, a solid solution material formed when Zirconium Oxide (ZrO_2) dissolved in CeO_2 matrix, were predicted. This calculation indicates the effect of chemical burnup in nuclear fuel as the thermal conductivity of CeO_2 was degraded as it forms a solid solution with ZrO_2. Xenon (Xe) and Krypton (Kr) are fission gases that collect in pores created in irradiation fuel matrix. The effect of fission gas bubbles like Xe and Kr, a component of chemical burnup, on the thermophysical properties of CeO_2 was simulated by strategically placing Xe and Kr atoms separately in pores created in CeO_2 to form CeO_2-Xe and CeO_2-Kr systems. The structure and thermal properties of CeO_2-Xe and CeO_2-Kr systems were investigated using Buckingham pair potentials for fission gases.

At extremely high temperature, where the condition of the fuel becomes unstable, some activities will start to occur in the fuel lattice. These activities contribute to the failure of the fuel to recover quickly during the loss of coolant accident. To better understand the condition of the fuel at high temperatures, the diffusion of atoms in the CeO_2 lattice is studied using molecular dynamics. This study clearly reveals the movement between the cerium (Ce) and oxygen (O) at high temperatures and suggest that O atoms break bond at a temperature relatively close to the melting temperature.

Spark Plasma Sintering (SPS) is a novel sintering technology capable of sintering diverse materials near 100% theoretical densities. CeO_2 and Ce_3ZrO_8 were synthesized using SPS for experimental analysis. The composition and the microstructure of the as-sintered pellets were characterized via X-ray Diffraction (XRD), Energy Dispersive Spectroscopy (EDS) and Electron Backscatter Diffraction (EBSD). These techniques were used on both CeO_2 and Ce_3ZrO_8 pellet samples to understand the structure, crystal orientation and phase disparity of the two materials. The thermal conductivity of the pellets at different porosity was measured using Direct Laser Flash (DLF) method. The porosity of the samples was studied using the Archimedes principle.

Acknowledgement

Whatever I do, whether in words or deeds, I do it all in the name of the Lord Jesus, giving thanks to God the Father through him. I will always thank my God because of His grace given to me in Christ Jesus. For in Him I have been enriched in every way, with all kinds of speech and with all knowledge to complete this work.

I sincerely appreciate my supervisors, my beloved Dr. Barbara Szpunar and Prof. Jerzy Szpunar, for giving me the rare opportunity and their unending patience to work under their supervision. These few years I have worked with you have widened my understanding and expanded my knowledge in all aspects of life. You guys are more than supervisors, you are parents. My heart cannot thank you enough for believing in me and providing me with the golden opportunity. I would like to also thank my committee members, chairman Prof. Rob Powel, Prof. Alexandre Koustov and Prof. Masoud Ghezelbash for taking the time to read my work and make necessary corrections.

I am especially grateful to my good friend, Adedapo Joseph Adegun, who has been there for me since my undergraduate days. Your unalloyed support which is innumerable over the years has been a source of joy to me. You are more than a friend and you are more than a brother, you are God sent. Thanks for always being there in the times that I have needed you. I am forever indebted to you and I will not try to repay because I know I cannot repay all. I just pray God will be with you always.

I appreciate the assistance of my colleagues in the computational group, Ravi Siripurapu, Linu Malakkal, and Jayangani Ranasinghe, for your supports and suggestions. I love you guys and will always love to work with you all the time. I would like to thank my senior friends, Ericmoore Jossou and Dr. Ubong Eduok, for their constant brotherly love and academic support. You guys are the best.

A special note of appreciation to the pastorate and ministers of RCCG Grace Sanctuary, Saskatoon for their spiritual and moral guidance. Particularly to the Odeyemi's family, I say very big thank you for everything they have done for me since my first day here. Thanks for being my family

here. I will also like to appreciate my family back home for their prayers at all time. The completion of this work would not have been possible without their endless love and faith in me.

I acknowledge access to high-performance supercomputers, Compute Canada (Westgrid and CalculQuebec), and Plato at the University of Saskatchewan. I appreciate the support of the Physics and Engineering Physics computer technical, Dave McColl, for his undivided attention and support at all time. I gratefully acknowledge the financial support of Canadian Natural Sciences and Engineering Research Council (NSERC), Canada Research Chair program and the Department of Physics and Engineering Physics, University of Saskatchewan.

with great love and respect, this one is for my jewel, Victoria Oladimeji.

Table of Contents

List of Tables

List of Figures

List of abbreviations and symbols

Abbreviation	Definition
3D	Three Dimensional
ATF	Accident Tolerant Fuels
BTE	Boltzmann Transport Equation
BWR	Boiling Water Reactor
CANDU	CANada Deuterium Uranium
DFT	Density Functional Theory
DFPT	Density Functional Perturbation Theory
DLF	Discovery Laser Flash
EAM	Embedded Atom Method
EBSD	Electron Backscatter Diffraction
EDS	Energy Dispersive Spectroscopy
FCC	Face Centered Cubic
GFR	Gas-cooled Fast Reactor
GIF	Generation IV international forum
GULP	General Utility Lattice Program
HCACF	Heat Current Autocorrelation Function
IAEA	International Atomic Energy Agency
IFC	Interatomic Force Constants
INES	International Nuclear Event Scale
LAMMPS	Large-scale Atomic/Molecular Massively Parallel Simulator
LDA	Local Density Approximation
LFR	Lead-Cooled Fast Reactor
LWR	Light Water Reactor
MEDEA	Materials Exploration and Design Analysis
MD	Molecular Dynamics
MPI	Message Passing Interface
MSD	Mean Square Displacement

MSR	Molten Salt Reactor
NVE	Number of atoms, Volume and Energy
NVT	Number of atoms, Volume and Temperature
NPT	Number of atoms, Pressure and Temperature
NRX	Nuclear Research eXperimental
ORNL	Oak Ridge National Laboratory
PBC	Periodic Boundary Conditions
PDF	Powder Diffraction File
PDOS	Partial Density of States
PWR	Pressurized Water Reactor
QE	Quantum Espresso
QHA	Quasi-Harmonic Approximation
RHR	Residual Heat Removal
SCWR	Super-Critical Water-Cooled Reactor
SEM	Scanning Electron Microscope
SFR	Sodium-cooled Fast Reactor
SPS	Spark plasma Sintering
TDOS	Total Density of States
USSR	Union of Soviet Socialist Republics
VHTR	Very-High-Temperature Reactor
XRD	X-ray Diffraction

Symbols	Definition
σ	Stress
ε	Strain
Y	Young's Modulus
η	Poisson's ratio
B	Bulk Modulus
G	shear modulus
D	Diffusion coefficient
D_o	maximum diffusion coefficient
K	Kelvin
Å	Angstroms
ps	Pico seconds
fs	Femto seconds
GPa	Giga Pascal
MPa	Mega Pascal
R	Universal gas constant
E_A	Activation energy
K	Proportionality constant
FM	Maxwell-Eucken factor
^oC	Degree Celsius
W	Walt
m	Meter
K_L	Thermal conductivity
F_i	Force
V	Potential energy

a	Acceleration
$\mathbf{r}$	Position
$\boldsymbol{v}$	Velocity
t	Time
T	Temperature
P	Pressure
U_{ij}	Total energy
φ	Coulombic contribution
Q	Charge
G	Embedding energy
ρ^a	Atomic electron density
E[n]	Universal energy functional
$\rho(\omega)$	Density of states
k_B	Boltzmann constant
$\hbar\omega$	Energy of phonons
F_o	Total free energy
α	Thermal expansion
C_p	Heat capacity
$\gamma\ (T)$	Grüneisen parameter
$\theta(T)$	Debye temperature
f	Scaling function
P	Rate of heat flow
Δx	Thickness
A	Cross-sectional area
eV	Electron volt

CHAPTER 1

INTRODUCTION

1.1 Nuclear Power

The world's infrastructures run largely on electricity which involves all energy harnessed from every energy source available for human civilization. The demand for clean energy, especially the need for continuous, reliable supply of electricity on a large scale, is rapidly increasing. The quest to meet this insatiable energy demand justifies the need for fossil fuels and nuclear power. Generating electricity by fossil fuel has lots of detrimental impacts on the environment, and this is a major challenge. A source of potential energy is identified and converted into useful kinetic energy in many forms of energy production. Energy is generated by fossil fuel source via combustion, usually involving the conversion of chemical potential energy into kinetic energy (e.g. heat). In hydroelectric systems, energy is generated from the gravitational potential energy of bodies of water. Nuclear energy is the only fully developed technology available that can provide electricity cheaply, without generating harmful greenhouse gases [1]. The desired nuclear release is also accompanied by enormous heat generation. Nuclear power releases energy stored within the nucleus of an atom, which generates heat within the reactor that can be utilized in much the same way as in any conventional power plant. Nuclear reactors inhibit the nuclear fission process to generate heat by splitting a heavy atom into smaller atoms and repeating this process for numerous times through a chain reaction. In most nuclear power station, the radioactive uranium bundle heats up water into steam, at the nuclear reactor core, and the jet of steam is used to rotate the turbine, in turn generating electricity. Figure 1.1 is a simple schematic example of a nuclear power plant where heat generated by fission process is removed from the reactor by coolant in the primary loop then used to generate steam in the secondary loop. In this setup, the reactor core is completely separated from the secondary loop to avoid radioactive material being transported from the containment building to the conventional island. Apart from replacing coal and natural gas for electricity production, nuclear energy also plays an important role in hydrogen generation, production of radioisotopes, marine propulsion and in providing clean water. The first generation of nuclear power reactors around the globe was designed not only to produce electricity but also produce plutonium for military purposes [2]. The current nuclear reactors that are classified as Generation III or less have low thermal efficiency due to their low operating temperature.

Therefore, various countries had initiated an international collaboration during the Generation IV International Forum (GIF) to develop the next generation nuclear reactor [3]. In 2002, GIF selected six reactor technologies among about hundreds of concepts reviewed. The selection of these technologies was made based on the criterion of providing clean, safe and cost-effective energy on a sustainable basis. The technologies are Gas-cooled Fast Reactor (GFR), Very-High-Temperature Reactor (VHTR), Sodium-cooled Fast Reactor (SFR), Lead-Cooled Fast Reactor (LFR), the Molten Salt Reactor (MSR) and Super-Critical Water-Cooled Reactor (SCWR). Independent of the interest from other developed nations, Canada has signed for research involving SCWR; an idea that is now considered as a natural evolution of the Canadian nuclear system concept due to the availability of the current CANada Deuterium Uranium (CANDU) reactor. The concept design also includes a fuel channel design for core outlet temperatures [4].

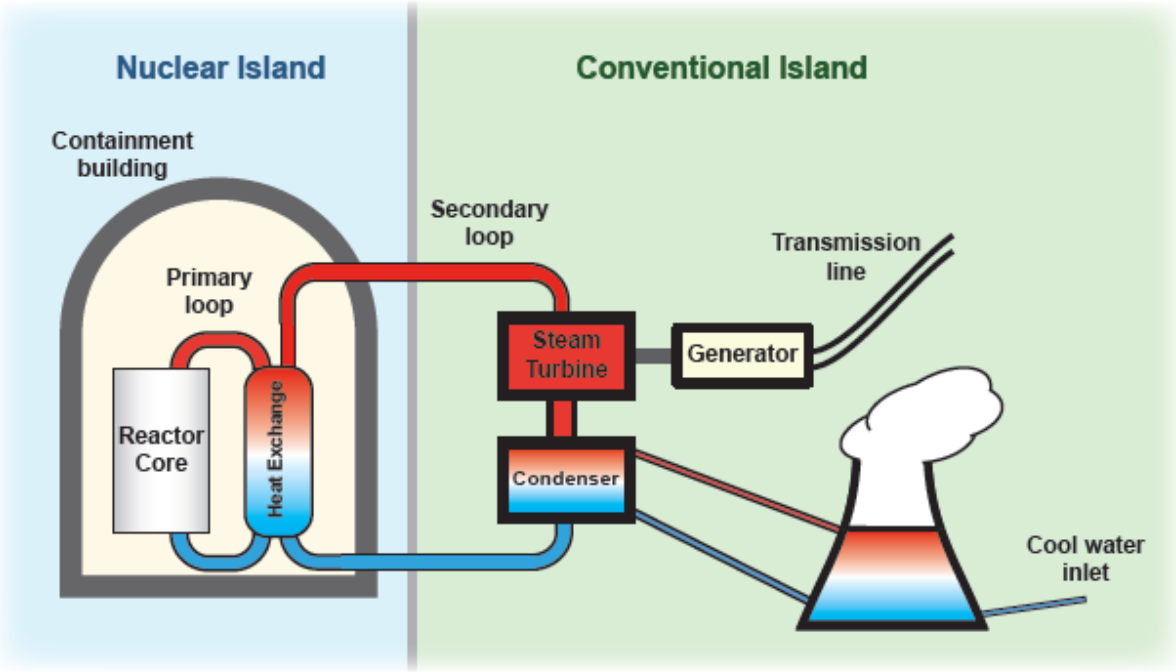

Figure 1.1: A simple illustrative diagram of a nuclear power station where the secondary loop extracts heat from the primary loop. The extracted heat is supplied to the steam turbine which powers an electric generator [5].

Nuclear reactor designs, operations, materials, and fuels are the major factors that dictate nuclear reactor safety. Most nuclear reactor accidents that occurred in recent time would have been prevented by improving one of the aforementioned factors. The improvement of nuclear reactor design over the years has fostered operation efficiency and safety of man and his environments. In recent time, attention has been shifted to improving nuclear reactor fuel as a means of preventing a nuclear accident. This is accomplished by studying the properties of nuclear fuel and the operations of nuclear reactors towards the production of safer nuclear fuel for present and future generation of nuclear reactors. When a nuclear reactor is in service, its fuel properties are significantly altered (alternatively called "fuel burnup"), due to inherent fission and reactor conditions. These conditions justify fuel performance and effectively limit the safety of both fuel and nuclear reactor. In this thesis, a step forward majorly focused on the deterioration of nuclear fuels during the operation of nuclear reactors will be studied. The nuclear industry is constantly evolving having to face new challenges and incorporate new technology. This chapter intends to introduce a variety of subjects, such as nuclear reactors, nuclear fission, nuclear fuels and nuclear accidents, which are the foundation on which this work is built.

1.2 Nuclear Reactor

In 1953, when nuclear fission reactors were becoming popular, two scientists; George W. Wetherill and Mark G. Inghram of the University of California and University of Chicago respectively discovered that some uranium deposits might have once acted as a natural version of the nuclear fission reactors [6]. In May 1972, a worker at a nuclear fuel processing plant in France noticed something suspicious when he was conducting a routine analysis of uranium derived from a seemingly ordinary source of ore [6]. The material under study contained three isotopes uranium-238, the most abundant variety; uranium-234 (U-234), the rarest; and uranium-235 (U-235), the isotope that is coveted because it can sustain a nuclear chain reaction. These samples came from the Oklo deposit in Gabon, a former French colony in west equatorial Africa, and U-235 constituted just 0.717 percent of the ore. Analysis showed that U-235 ore from at least one part of the mine was some 200 kilograms less. This amount unaccounted for was enough to make nuclear bombs. For weeks, specialists at the French Atomic Energy Commission (CEA) remained perplexed. About nineteen years earlier, a prediction was published that uranium ore body may undergo self-sustained fission and that seems like the answer the French specialists were looking

for. Paul K. Kuroda, a chemist from the University of Arkansas, calculated what it would take for a uranium ore body to spontaneously undergo self-sustained fission. In this process, a stray neutron causes a U-235 nucleus to break down, which produces more neutrons, causing others of these atoms to split apart in a nuclear chain reaction. Kuroda's first condition was that the size of the uranium deposit should exceed the average length that fission-inducing neutrons travel, about two-thirds of a meter. This requirement helps to ensure that the neutrons given off by one fission event are absorbed by another uranium atom before escaping from the uranium vein.

The first artificial nuclear reactor was constructed on December 2, 1942, when a Chicago-based scientist first initiated a self-sustaining and controlled nuclear chain reaction by removing a cadmium coated control rod from Chicago Pile 1 [2,7]. George Weil, supervised by Enrico Fermi and Leo Szilard, made history, under an abandoned sports ground at the University of Chicago, as he allowed the first artificial chain reaction to begin. Witnessing this was a small group of scientists who looked on for about thirty minutes before the neutron-absorbing cadmium rods were pushed back in, gently bringing the first man-made fission reaction to an end. The neutron activity from the unshielded pile containing 400 tons of graphite, 6 tons of uranium metal and 50 tons of uranium oxide, as shown in Figure 1.2, was carefully monitored by Fermi.

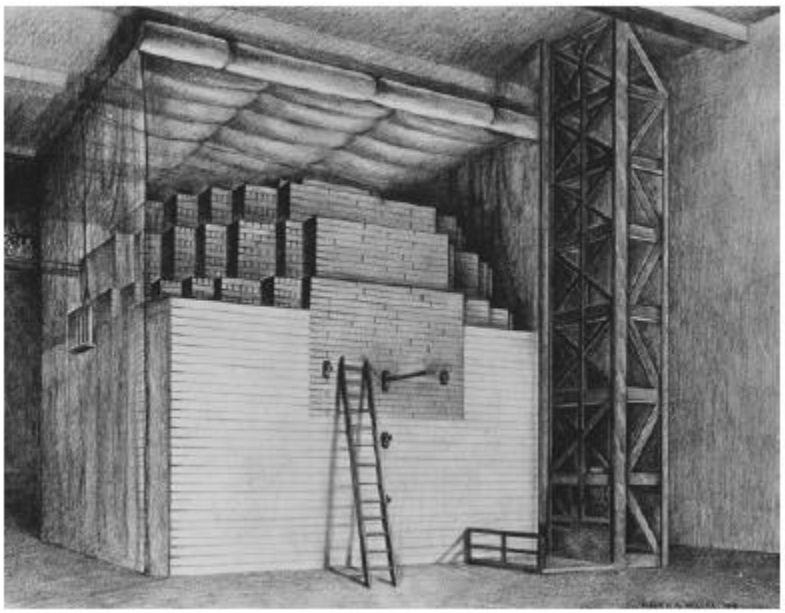

Figure 1.2: Architect's drawing of the Chicago Pile 1 [8]

The initiation of chain reaction is a necessary condition to release significant proportions of energy from uranium, which means every fission reaction must trigger at least one further reaction to maintain a continuous flow of fission reactions in the reactor. U-235 is an important material for such fission reaction as the fission of U-235 creates 2 or 3 neutrons on average [9]. Conventional reactors have several ways in which they ensure a bias towards fission of U-235. Materials used in reactor fuel cladding, such as Zircalloy, are typically neutrons transparent and these materials are selected to reduce the loss of parasitic neutron. High energy neutrons, which are too fast to cause fission, are slowed down by moderators to velocities that are more likely to cause fission of U-235. The rate of fission reactions can be increased by the enrichment of uranium, which increases the U-235 to Uranium-238 (U-238) ratio. Also, at the reactor boundaries, environmental neutron leakage is minimized by using neutron reflectors

After Chicago Pile 1, a broad range of nuclear reactor design was developed over the years to alleviate energy release via chain reactions. Early nuclear reactors are non-commercial and research based reactors; currently, nuclear reactors are classified by generations spanning from Generation I-IV reactors. Generation I reactors are research reactors, non-commercial power reactors and these are the early prototypes of nuclear power reactors. The current group of nuclear power plants is classified as Generation III or less. However, these reactors are not as energy efficient as they can be because the operating temperatures are relatively low. Currently, a group of countries, including Canada, have initiated an international collaboration to develop the next generation of nuclear reactors called Generation IV. Reactors that use water to cool and moderate nuclear reactors, known as Light Water Reactor (LWR), make up much of power reactors globally. Boiling Water Reactor (BWR) and Pressurized Water Reactor (PWR) are the two major types of electricity generating Light Water Reactor (LWR). Currently, the thermal efficiency of nuclear reactors is in the range 30% - 35%, and with the new reactors, which are the Generation IV reactors, such efficiency will be increased to 45% - 50%.

Gas-cooled Fast Reactor (GFR), Very-High-Temperature Reactor (VHTR), Sodium-cooled Fast Reactor (SFR), Lead-cooled Fast Reactor (LFR), Molten Salt Reactor (MSR), and SuperCritical Water-cooled Reactor (SCWR) are the six major reactors to be developed. The primary goals of these reactor types are to improve nuclear safety, minimize waste and to reduce the cost to build and run such plant. This chapter will provide a brief description of each nuclear reactor concept.

Gas-cooled Fast Reactor (GFR) is a fast-neutron-spectrum reactor, which also features closed fuel cycle for efficient conversion of fertile uranium and the running of actinides. Through thermochemical processes, GFR can be used to produce electricity and co-generation of hydrogen. Different types of gases with low neutron capture cross sections can be used as coolants. The most suitable coolant is helium gas with inlet and outlet temperatures of 490^{o}C and 850^{o}C respectively. A typical GFR is presented in Figure 1.3.

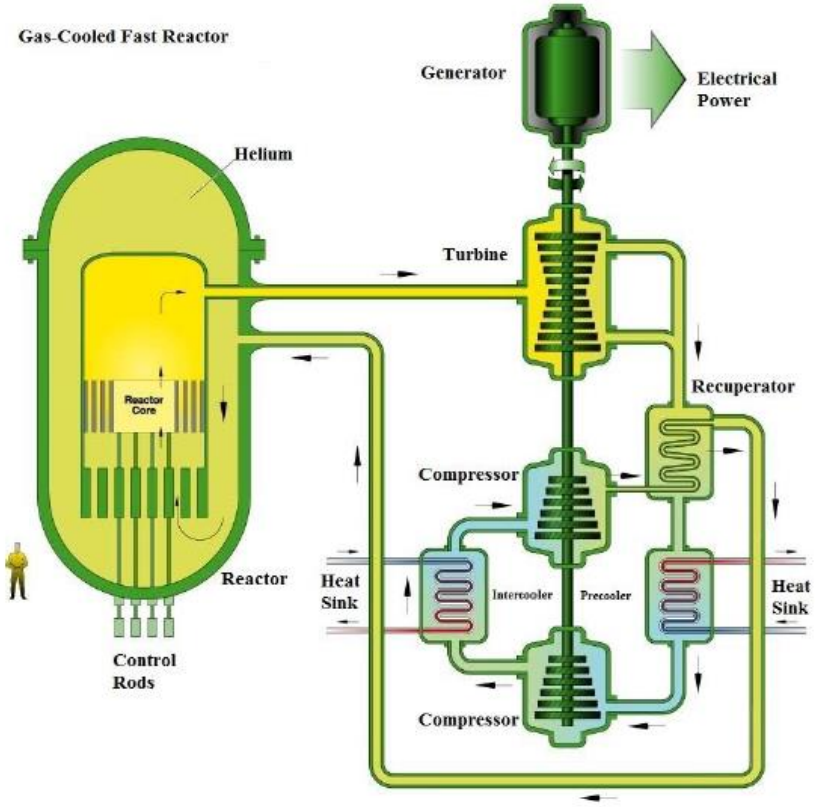

Figure 1.3: Schematic diagram of Gas-Cooled Fast Reactor [10]

Since GFR operates on high energy fast neutrons, using a moderator to slow down those neutrons is unnecessary. The fast-moving neutrons can move freely without a moderator. This design of reactor can use thorium as fuel, apart from uranium, which is unsuitable for Light Water Reactors (LWR). The GFR's fast spectrum is empowered to use available fissile and fertile materials [10]. The net plant efficiency of GFR is 48% with a direct Brayton cycle.

The Very-High-Temperature Reactor (VHTR) system is designed to be a high-efficiency system that can supply heat [11]. VHTR is a thermal-neutron-spectrum reactor which may incorporate electricity generating equipment to meet cogeneration needs. The ultimate purpose of this nuclear-reactor design is the cogeneration of hydrogen through thermochemical processes. VHTR uses graphite as moderator and helium, with inlet and outlet temperatures of 640^{o}C and 1000^{o}C respectively, as a coolant. Apart from offering a broad range of heat applications, VHTR also has the flexibility to adopt uranium/plutonium fuel cycles and offers enhanced waste minimization. VHTR design, presented in Figure 1.4, will offer a thermal efficiency above 50%.

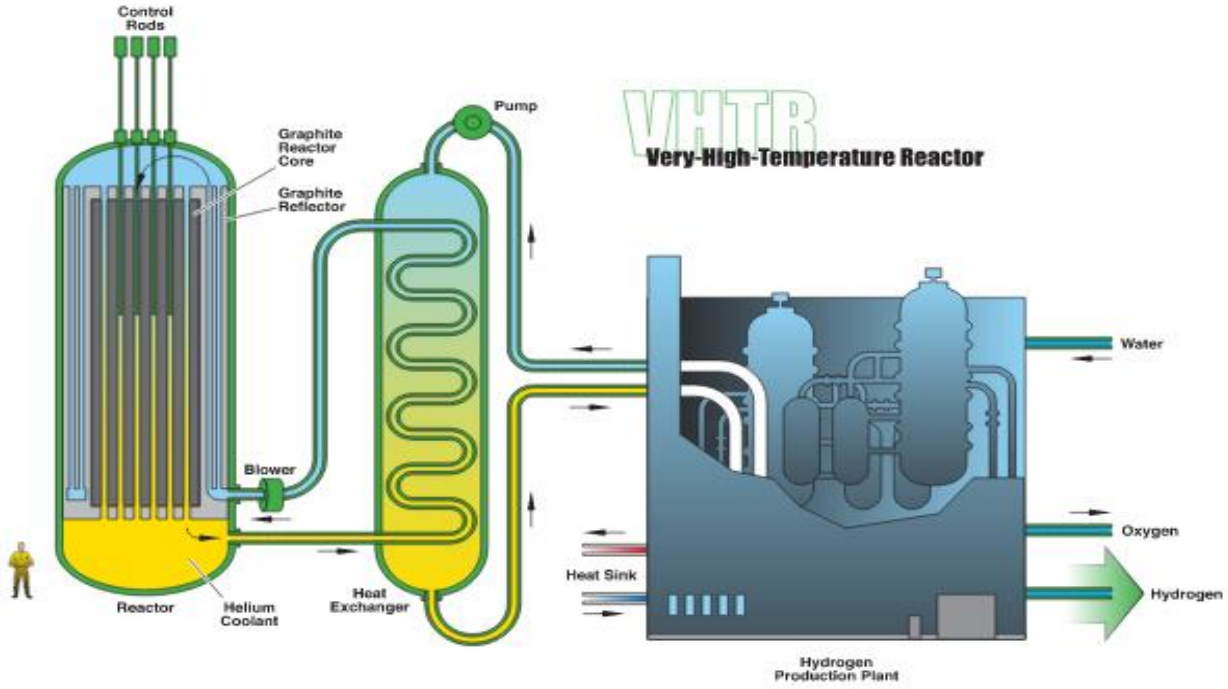

Figure 1.4: Schematic diagram of Very-High-Temperature Reactor (VHTR) [11]

Sodium-Cooled Fast Reactor (SFR) system, like GFR, has a closed fuel cycle for efficient management of actinides and conversion of fertile uranium. The SFR permits the management of high-level wastes and, in particular, management of plutonium and other actinides. Important safety features of the system include a long thermal response time, an efficient cooling system, a primary system that operates near atmospheric pressure, and an intermediate sodium system between the radioactive sodium, which located in the primary system, and the water and steam in

the power plant. SFR uses liquid sodium as its coolant with an outlet temperature between 530°C and 550°C at atmospheric pressure. Figure 1.5 is a schematic diagram of SFR.

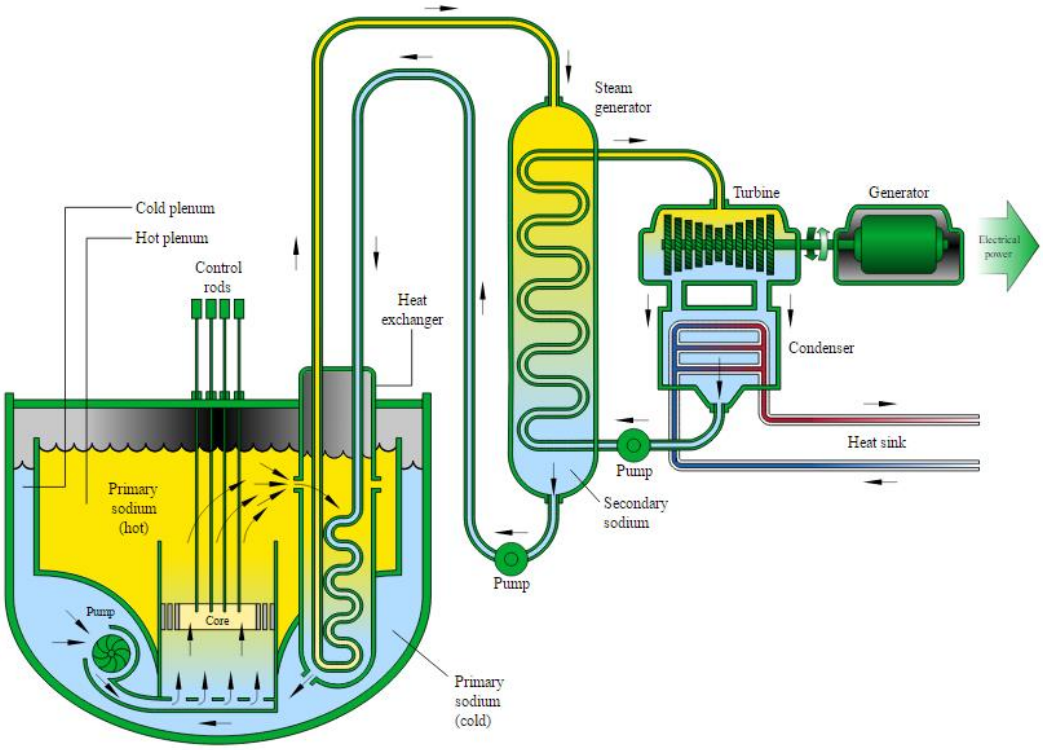

Figure 1.5: Schematic diagram of Sodium-Cooled Fast Reactor (SFR) [12]

A good advantage of liquid metal coolants is that despite the low specific heat, Sodium has a melting and boiling point of 371K and 1156K respectively, allowing a total temperature range of 785K of heat difference between solid and vapor states. This allows the absorption of significant heat in the liquid phase. The high thermal conductivity property effectively creates a reservoir of heat capacity which provides thermal inertia against overheating [13]. With innovations to decrease capital cost, the SFR can serve markets for electricity. The SFR's fast neutron spectrum also makes it possible to use fissile and fertile materials (including depleted uranium), though the primary choices of fuel for SFR are oxides and metallic fuels [12].

Lead-cooled Fast Reactor (LFR) is a small factory-built turnkey plant operating on a closed fuel cycle with a very long refueling interval of about 15 to 20 years, cassette core or replaceable reactor

module. Its features are designed to cope with market opportunities for electricity production on small grids, and for developing countries that may not wish to deploy indigenous fuel cycle infrastructure to support their nuclear energy systems [14]. LFR is a fast-neutron-spectrum reactor which uses lead or lead-bismuth, with the outlet temperature of about 480°C - 567°C at atmospheric pressure, as its coolant. The primary choice of fuel is a nitride fuel.

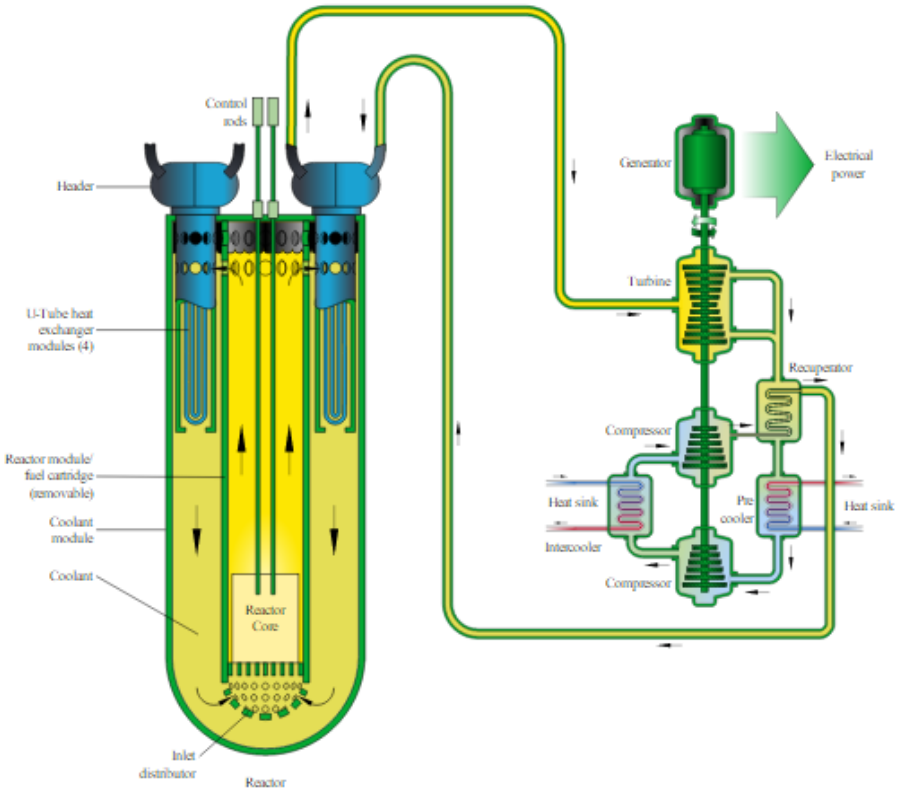

Figure 1.6: Schematic diagram of Lead-Cooled Fast Reactor (LFR) [14]

The Molten-Salt Reactor (MSR) was built during the 1960s, at the Oak Ridge National Laboratory (ORNL), as an experimental reactor [15]. MSR is a thermal-neutron-spectrum reactor, which uses a molten fluoride salt with dissolved uranium. Figure 1.7 shows the MSR design where the left side of the reactor contains the fuel salt, dissolved uranium in a mixture of molten fluoride salt. The fission process stabilizes itself, as fuel salt expansion pushes some of the fuel into the circulation loop which in turn decreases the fission rate, once the fuel salt reaches a temperature around 700°C. Unlike in conventional reactors, the fuel salt also acts as a coolant to the reactor as it is circulated through a heat exchanger where it will be cooled by another molten salt loop that is

radioactive fuel and fission products free. The inlet temperature of the coolant is 565°C while the outlet temperature reaches 700°C.

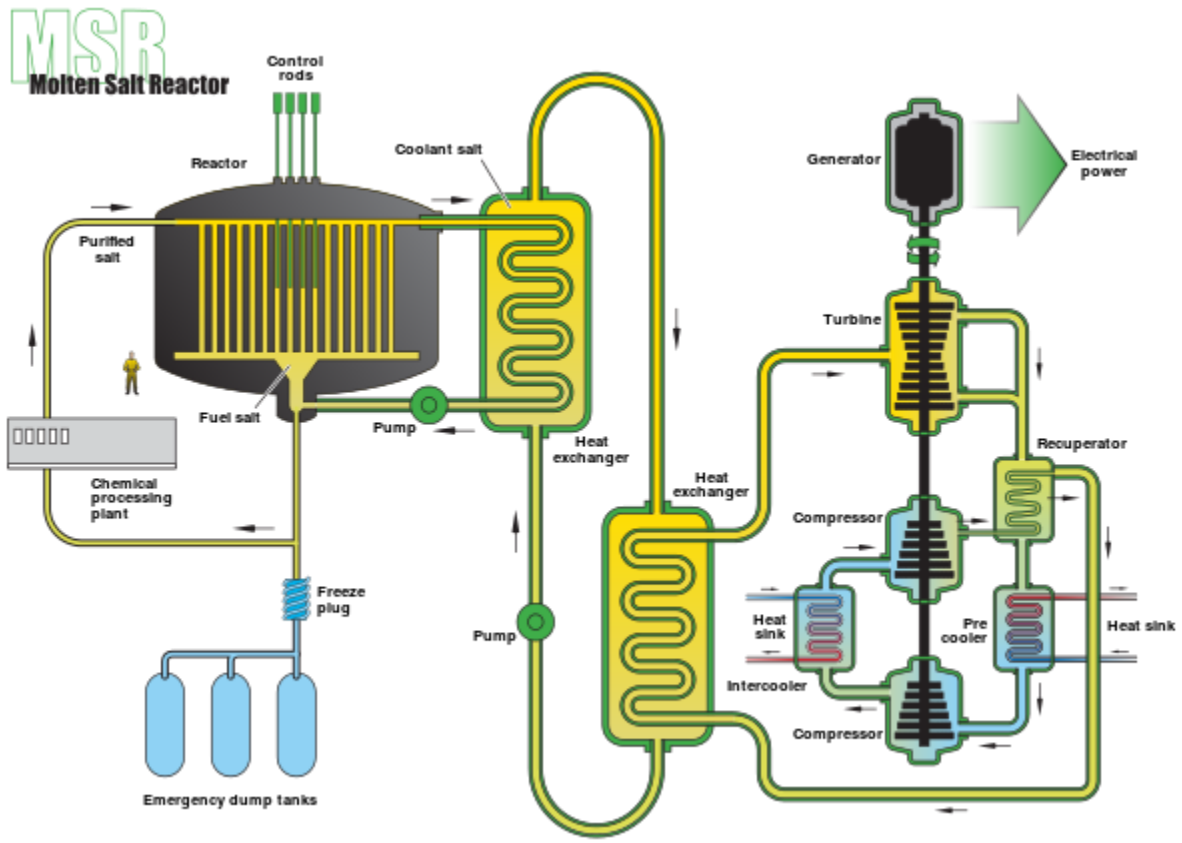

Figure 1.7: Schematic diagram of Molten-Salt Reactor (MSR) [16]

However, the outlet temperature of the fuel salt mixture can even increase to 850°C and at such temperature co-generation of hydrogen can be considered as an option. The thermal efficiency of the plant is between 45 and 50% [16]. The molten design of MSRs makes the most interesting part of the reactor. With such design of MSRs, the reactor core cannot melt and, as such, the reactor is considered very safe. An overheating cannot happen in MSR because the heat should melt a freeze plug at the bottom of the reactor and the liquid fuel salt will be drained into the emergency cooling tanks where it will be cooled and solidified. This automatic process needs neither an operator reaction nor other emergency backup power for safe operation. Even an external human engineered damage of an MSR, that can happen during a terrorist attack, cannot cause any serious release of radioactivity. The fuel salts for MSRs function at normal atmospheric pressure, so a

crack of the reactor containment vessel would just leak out the liquid fuel which would then solidify as it is cooled [17].

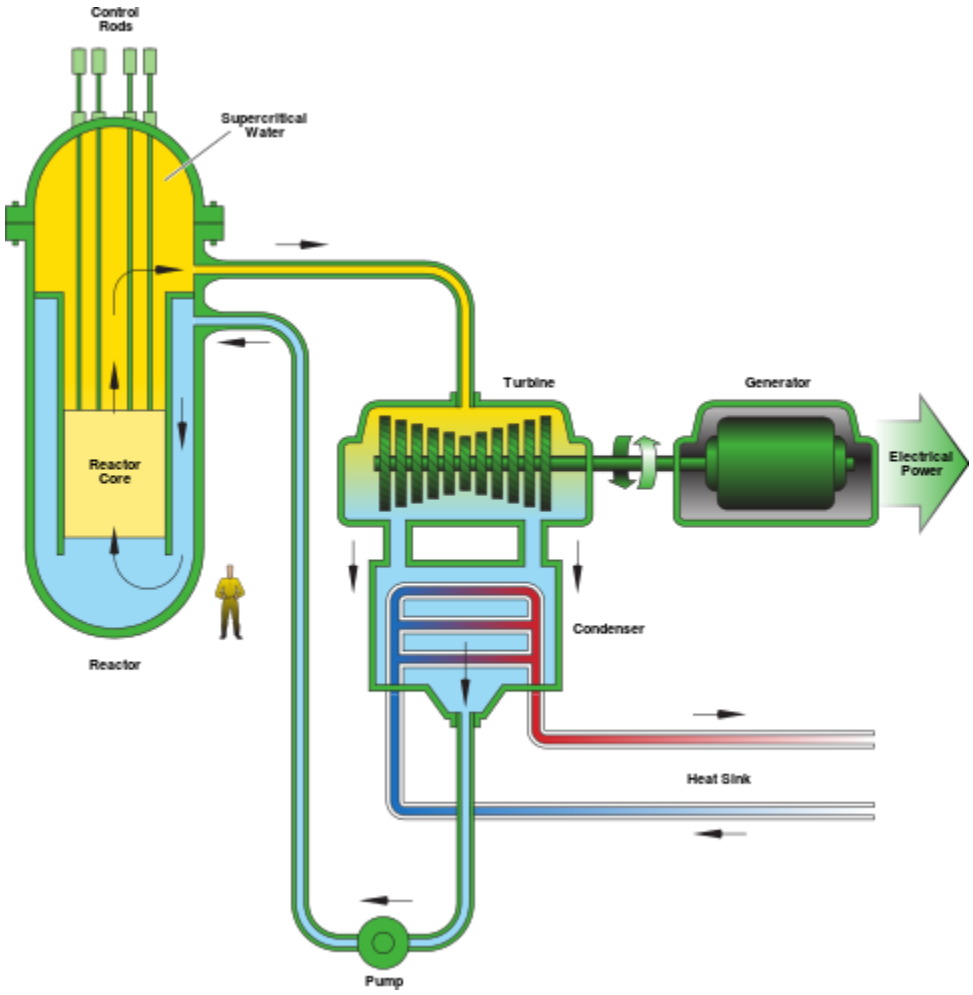

Figure 1.8: Schematic diagram of SuperCritical Water-cooled Reactor (SCWR) [16]

SuperCritical Water-Cooled Reactor (SCWR), which is mostly designed as light water reactor (LWR) that operates at supercritical pressure, can either have a thermal-neutron spectrum or fast-neutron spectrum depending on its core design. The difference between thermal and fast versions of the reactor is primarily the amount of moderator material in the SCWR core. SCWRs are high-temperature and high-pressure water-cooled reactors, which uses the supercritical water as its outlet coolant and light water as its moderator and operate above the thermodynamic critical point of water which is at 374°C temperature and 22.1 MPa pressure. The operating pressure of SCWR is 25 MPa and the outlet temperature of the coolant is 625°C [16]. The thermal efficiency of SCWRs supersedes that of LWR which is known to be around 33% to 35%. SCWRs thermal

efficiency can approach a level of 44%, hence, offering a unique advantage compared to the LWR. The primary choice of fuel for SCWR will be the traditional LWR fuel which is an oxide fuel although a metallic fuel may be considered as the secondary choice.

Canada is known for her CANDU reactor but has taken up research on a much more passive safe and accident tolerant SCWR based on the existing CANDU configuration. The concept deployed incorporate significant advances in thermal efficiency, fuel cycle sustainability, and relative cost of energy. The most interesting ability of the reactor is its walk-away safety concept, making it an accident tolerant reactor [18]. Geneneration IV reactors are believed to be the future nuclear reactors having enhanced safety and proliferation resistant properties. The goal is to introduce the first reactors in service by 2040 or earlier [19].

1.3 Nuclear Fission

During the final stage of second world war, in 1945, two nuclear bombs were dropped in Japan. The Atomic-bomb campaign was considered as a sure and quick way to bring the war to an end with a minimum number of casualties. However, this was also a large scale nuclear fission experiment [20]. Like the Atomic-bomb, nuclear fission is the main process generating nuclear energy in a nuclear reactor. A heavy nucleus must first interact with a neutron before any nuclear fission process is initiated. The energy from this process makes use of varying binding energies of the atom. A typical distribution of fission product yield is presented in Figure 1.9 where the atomic mass of fission products is plotted against the percentage yield in a fuel composed of 65% Uranium (U) and 35% Plutonium (Pu).

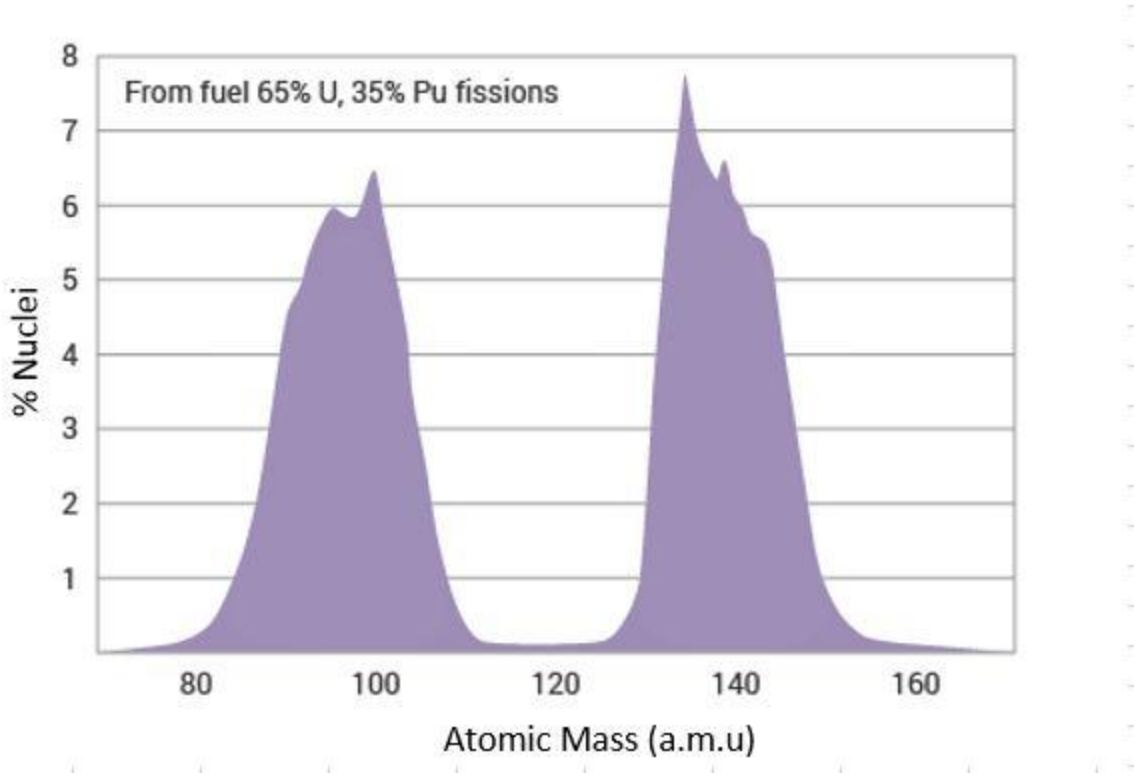

Figure 1.9: Distribution of Fission Product across the periodic table [21]

Spontaneous fission can occur, but the transmutation of a large nucleus through neutron capture greatly increases the activation of the nuclear fission process. Fission may also occur when a heavy nucleus like U-235 capture a thermal neutron, the captured neutron is added to the U-235 nucleus to form a new compound nucleus Uranium-236 (U-236) which is relatively unstable and is likely to break into two fragments. The new nucleus may decay into a different nuclide as shown in Figure 1.10. The neutrons produced from this event can be recaptured by another heavy nucleus and then go on to produce additional fission process, hence maintaining the fission chain reaction [22]. Energy is generally released as the heavy nucleus (fuel) splits into two smaller nuclei. Energy generated, 85% of which is represented as the kinetic energy of the fission fragments, is converted to heat. Neutrons are mostly the important candidates that sustain and serve as the control system of the fission chain reaction. The amount of energy released is controlled by the number of delayed neutrons released. The longest traveling delayed neutrons can only last 56 seconds [21]. The chain reaction is always balanced at criticality, that is the number of neutrons produced in fission remains constant which in turn keep the amount of power generated constant. During fission process, some neutrons are absorbed, some cause fission and some are leaked out of the system.

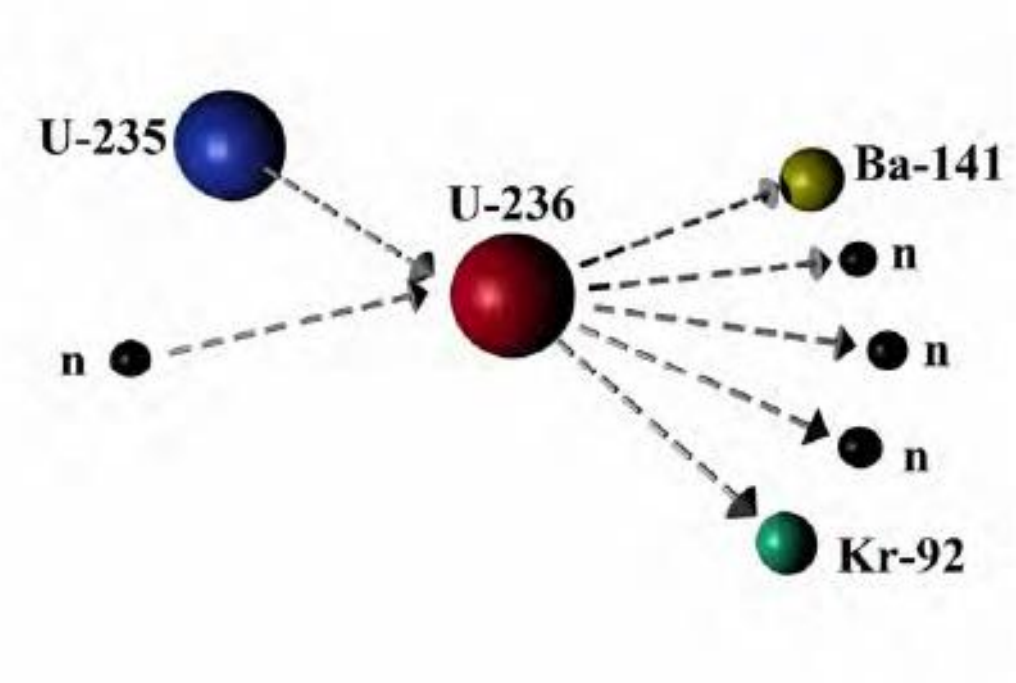

Figure 1.10: Fission process involving a U-235 nucleus capturing a neutron to produce three neutrons, Barium-141 and Krypton-92 [23]

All these neutrons are well accounted for and the rate of power production is regulated by changing their balance so that the number of neutrons present is either increased or reduced. However, energy is generated in fuel during fission processes through mass (m) conversion as predicted by Einstein's mass-energy equivalence relationship [24]. The total rest masses of all fission products, after fission has occurred, is smaller than that of the fissile species and this small amount of missing mass is associated with the binding energy which is released during the fission process [21].

$$^{235}_{92}U + {}^{1}_{0}n \rightarrow {}^{141}_{56}Ba + {}^{92}_{36}Kr + 3{}^{1}_{0}n \quad (170\ MeV) \tag{1.1}$$

Equation (1.1) above shows conservation of nucleons, that is 235 + 1 = 141 + 92 + 3, but the energy released is known to be equivalent to the small loss in atomic mass. However, the fission products (Ba and Kr) will further decay and form more stable isotopes with the emission of β particles which makes the fission product highly radioactive. This radioactivity depends solely on time as it decreases over a period. Although, about 6% of the reactor core heat mostly originates from radioactive decay of fission products [21]. Nuclear fission is the basic phenomenon that generates energy in the core of a nuclear reactor, however, a few nuclear accidents in nuclear

reactors occurred as result of an inability to immediately shut down nuclear fission process during unexpected reactor failures. Nuclear fission process, which was normally quite tame and easy to control, could suddenly go nervous and cause a nuclear accident. This may cause harm of a devastating proportion due to a combination of unpredicted mechanical failures, human error and/or natural disaster.

1.4 Nuclear Accident

Series of nuclear reactor accidents have occurred, starting from 1952 in Chalk River to 2011 at Fukushima, Japan. The majority of these accidents, which have a serious environmental impact, were initiated or caused by either human error or natural disasters. These accidents are exclusively rated on the International Nuclear Event Scale (INES) of the International Atomic Energy Agency (IAEA). The nuclear accident of 1952 involving the Canada's Nuclear Research eXperimental (NRX) reactor at Chalk River, Ontario was caused due to human error. The NRX research nuclear reactor became operational in 1947, after nearly three years of development and construction, and was then the most powerful general-purpose research reactor in the world [20]. The NRX research reactor, which had its cylindrical aluminum reactor vessel in a squat flattened design and used heavy water as a moderator, was used for developing radiation therapy to treat cancer, materials measurement and production of medical isotopes. The NRX accident was a typical nuclear disaster that was caused by several bad decisions from the facility operators. The four valves containment pressure system in the cooling system was opened by the operators which prompted an explosion that demolished the NRX reactor core [25]. An operator, during his routine check, inappropriately corrected a wrongly positioned bank of compressed air bypass valve handle. In doing so, he had applied compressed air to the underside of four shutdown rods which blew them out of the core. With three of the shutdown rods stuck in the out position and other few wrong instructions from the reactor supervisor, the reactor went supercritical causing a chain reaction with power doubling every 2 seconds. Tones of nuclear fission particles were released into the atmosphere along with one million gallons of water containing thousands of curies of various radioactive fission products after a series of hydrogen gas explosions had occurred due to the closure of shutdown rods not fully descended. This event brought about the world's first nuclear reactor core meltdown and first hydrogen explosion [26]. The NRX reactor was rebuilt after the accident and its diagram is

presented in Figure 1.11. This accident was small, but it was a harbinger of things to come, these events would happen again, perhaps on a larger and even more dangerous scale.

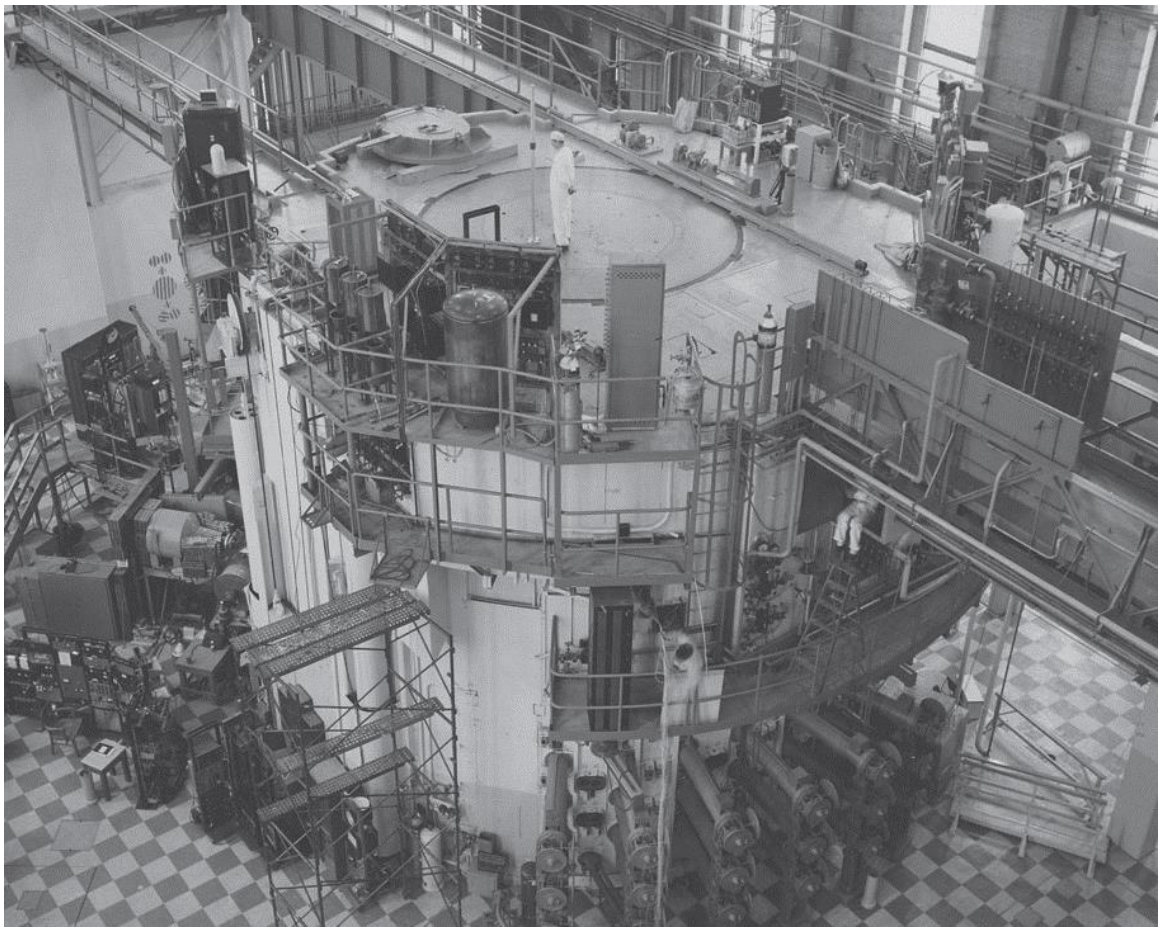

Figure 1.11: A photo of the rebuilt NRX heavy-water reactor in Chalk River, Canada after the 1952 accident [27]

After the 1952 nuclear reactor accident in Chalk River, series of other accidents occurred but they were nothing to be compared to the Chernobyl nuclear disaster. In its quest to dominate and modernize the economic sector, the Union of Soviet Socialist Republics (USSR) deemed it fit to construct powerful nuclear power plants which will serve the goals of producing electricity and nuclear bombs. These goals were met simultaneously by employing the RBMK water-cooled graphite-moderated reactor concept, a reactor design that uses blocks of solid graphite as the neutron moderator and water as its coolant. Chernobyl, an ancient town in the Byelorussian-Ukrainian woodlands in the then USSR, was a good location for this concept and without wasting much time by 1986 Chernobyl already had four of these nuclear reactors completed and online

with two additional reactors still under construction [20]. During a scheduled safety experiment between the late night of 25th April and early morning of 26th April 1986, the serious accident occurred when reactor 4 exploded. Prior to the safety experiment, there was a concern that there would be a delay between having lost power from the generator, in the case of an emergency reactor shutdown while power production is going on, and starting the backup generator. So USSR had scheduled a safety experiment for reactor 4 to find out how long the steam turbine would continue generating electricity once the flow of steam is cut off [28]. The experiment sequence, which started at 1:00 pm on April 25 with the entry of control rods in the core of the nuclear reactor, was delayed when a call came in from the electrical load dispatcher reporting that demand for electricity in Kiev seemed to be peaking at that moment. Later at night, they were able to resume the power-down and the aim was to level out at 1500 megawatts. The operators had earlier disconnected the system power regulation by disabling the local automatic control system for the experiment and it became an enormous work for the reactor control engineer to keep the flux profile balanced as the power dropped. The operators juggled the controls as things were getting wild by trying to balance the neutrons which were crowded on one side of the reactor and scarce on the other side. During this struggle, the reactor power drastically slid down from 1500 megawatts to 30 megawatts and the Xenon poisoning, a phenomenon where excessive Xenon-135 atoms were produced to knock down fission neutrons, was activated. The power is to remain at 1500 megawatts to carry out the safety experiment. The operators were making sure that was the case by manually removing the control rods to unleash the reserve reactivity and raise the power back to where it should be. Almost all the control rods have been removed, leaving the nuclear reactor in an unsafe and extremely unstable condition, when the operator in the control room pushed the last button to start the experiment. At that time, the power had rapidly increased beyond normal and the operators never noticed on time. After the reactor had gone supercritical the control rods were loosed, using the emergency power reduction system, but they did not respond because the controls were already deformed by heat and at that moment the operators disconnected them to allow the control rods fall by gravity. There was a deep rumble and the entire building began to shake, as the nuclear fuel disintegrated and the reactor started melting [20]. Instantly, two big explosions rocked the Chernobyl reactor 4 blowing through the air the walls of the reactor room, nuclear fuel, and radioactive dust. The radioactive material released during this accident is

estimated to be 200 times larger than that of the Hiroshima and Nagasaki atomic bombs and the accident was rated level 7 on the INES scale [28].

It was as though the worst had happened, and we thought we had seen it all in Chernobyl, until it happened again and now at Fukushima, Japan. The accident at Fukushima in 2011 was caused by natural disaster, an earthquake and a tsunami disabled the power supply and the cooling system of three nuclear reactors that were in operation. There were six (6) BWR reactors at Fukushima Daiichi power plant and about four (4) of the reactors were damaged during this accident [29]. Fukushima Daiichi Unit 1, 2 and 3 were in operation when the Great East Japan Earthquake (2011 Tohoku) of magnitude 9.0 struck on 11 March 2011. All the nuclear reactors in operation at that moment shut down automatically when the quake hit. The quake did considerable damage, disabling all six external power supply sources to the Residual Heat Removal (RHR) system cooling pumps, but the large tsunami it created caused a very much more damage. After a nuclear reactor shutdown, the reactor core would continuously produce about 1.5% of their nominal thermal power which will generate enough heat to melt the reactor core, depending on the nuclear fuel, if not cooled by an external heat exchanger. Since the external power supply was disabled by the earthquake, the emergency diesel generators in the basements of the turbine building started up and power the heat remover RHR system for about one hour until the tsunami wave hit the power station which was built near a beach. The two tsunamis that hit the power station took all the available power supply with them drowning the diesel generators, cooling system, and batteries located in the basement of the turbine building. The reactors in Unit 1 to 3 were put in a terrible situation, although, unit 3 had battery power for about 30 hours. A lot of steam began to build up in the reactor vessels housing the reactor core since there is no outside heat exchanger to remove heat from the reactor. The steam was then released into the dry primary containment to react with the reactor cladding which was made from zirconium alloy. The very hot zirconium cladding oxidized quickly, detaching all available oxygen atoms from the steam to form zirconium oxide (ZrO_2), to produce hydrogen gas. A hydrogen explosion hit the unit 1 reactor building, blowing off the roof and cladding, after the hydrogen mixed with air and ignited [20,29].

After accident report shows that the Fukushima Daiichi accident could have been avoided if a different nuclear fuel was used in the nuclear reactor. The loss of coolant has led to nuclear fuel meltdown due to low thermal conductivity of the fuel, thus questioning the safety of reactor with

UO_2 fuel. Nuclear fuel with high thermal conductivity would have dissipated heat faster to the sink thus reducing the centerline temperature and preventing the subsequent melting of the fuels. After Fukushima accident, the major focus of nuclear researchers has been on the development of accident tolerant fuel and the major characteristic of such fuels is high conductivity that will allow the reactor core to withstand the loss of coolant for a longer period.

1.5 Nuclear Fuel

1.5.1 Uranium Dioxide (UO_2) Fuel

Most nuclear reactors are powered by traditional nuclear fuel known as uranium dioxide (UO_2) fuel. UO_2 powder is compressed/sintered to form fuel pellets which are bundled into a fuel rod and inserted into the nuclear reactor. Nuclear fuels are classified into two categories; metallic fuels and ceramic fuels. Metallic fuels have a higher thermal conductivity, which is quite an advantage over ceramic fuel, but suffer from the low melting point, high-temperature oxidation and often undergo phase changes. The phase of metallic fuels changes with temperature, which also results in a volume change of the fuel. Furthermore, fuel swelling is common in metallic fuel when exposed to neutron flux and this, in turn, creates an adverse effect on the fuel's thermal efficiency. Uranium, plutonium, and thorium are the most common metallic fuels. On the contrary, ceramic fuels have several good characteristics and important properties. Low thermal conductivity fuel, high thermal conductivity fuel, and enhanced thermal conductivity fuel can be manufactured. Low thermal conductivity UO_2 fuel is the most commonly used fuel type in commercial nuclear reactors but the recent accident in Fukushima clearly illustrate the risk associated with the present design of reactor based on low thermal conductivity fuel and justifies research towards high thermal conductivity and enhanced thermal conductivity fuel. Notwithstanding, investigating the factors undermining the performance of present UO_2 fuel is an important research towards developing Accident Tolerant Fuels (ATF). Furthermore, there is an interest in using Thorium dioxide (ThO_2) as fuel in nuclear reactors because thorium is widely distributed in nature and approximately three times as abundant as uranium [30]. Thorium itself is a fertile material and must be used with a driver fuel like UO_2 for the production of neutrons to help to start the thorium cycle. Currently, UO_2 fuel is used in PWRs, BWRs, and CANDU reactors, however, UO_2 is not suitable for SCWR but can be used as a component of enhanced thermal conductivity fuel [31,32].

Nuclear fuel's thermal conductivity is an important property that affects the fuel behavior at an operating temperature and also influences its safety under specific conditions. The thermal conductivity of UO_2 fuel is about 3 W m^{-1} K^{-1} within the operating temperature range of nuclear reactors and therefore its centerline temperature is considered high. Despite low thermal conductivity, UO_2 is chemically stable and has a high melting point. Additionally, UO_2 does not react with water within the nuclear reactors operating temperatures and the crystal structure of UO_2 retains most of the fission products even at high burn-up [33]. UO_2 fuel has a very stable structural property and its thermal conductivity decreases as temperature increases. Also, changes in fuel thermal conductivity occur during irradiation as a result of fission gas bubble formation, pores, cracks, dissolved and precipitated fission product buildup. The thermal conductivity of UO_2 fuel in nuclear reactor deteriorates with increasing burnup, a number of defects, and temperature [34]. The nuclear fission is the main energy-generating process in the reactor but the fission process also affects both the physical state and the chemistry of the fuel. After a few years of irradiation in the nuclear reactor, each atom in the nuclear fuel will experience a few thousand displacements from its lattice position, most displaced atoms usually return to a normal lattice position. However, some defects do not recombine, causing accumulations of point and extended defects in the fuel [35]. In irradiated oxide fuels, several fission products (FPs) are produced and they represent various chemical elements depending on the conditions of the fuel. The compounds composed of FPs would affect significantly the fuel characteristics. Therefore, the behavior of FPs under irradiation and the properties of their compounds are very important for the evaluation of the fuel performance.

1.5.2 Accident Tolerant Fuel (ATF)

ATFs are fuels with enhanced thermal conductivity, which can withstand the loss of coolant for a long period of time by allowing faster dissipation of heat, hence, lowering the centerline temperature and preventing the fuel melting. ATFs comprise of two major fuels; metallic and composite fuel. Uranium Nitride (UN), Uranium diboride (UB_2) and Uranium Silicide (U_3Si_2) are some of the candidate metallic fuels proposed to be used in the nuclear reactor. The attribute of such fuels is high thermal conductivity which is as a result of their electronic contribution to this important property. Metallic fuels seem promising but are limited by their low melting point, high-temperature oxidation and fuel swelling. Looking at the limitations of the proposed metallic fuels,

there is a need for further research to develop composite fuels. Composite fuels are proposed to be made by adding other fuel materials with high thermal conductivity to UO_2 and ThO_2 nuclear fuels to form an enhanced thermal conductivity fuel. This fuel will possess high thermal conductivity and the high melting point which are the important properties of a good reactor fuel. Apart from fast dissipation of heat and lowering the centerline fuel temperature, the composite fuel will consequently prevent the melting of a reactor core, minimizes oxidation of cladding and related hydrogen production to prevent any explosion. Additionally, the composite fuels will allow reduction of the thermal gradients and thermal stresses that contribute to cracking, thereby increasing the longevity of the fuel. Some preliminary investigations have been conducted to evaluate the possible advantage of composite fuel over the present UO_2 fuel. The scope here is to briefly analyze the thermal properties of ThO_2 fuel composites in order to improve thermal conductivity and propose safer fuel for present and future generation of nuclear reactors.

Table 1.1 presents the thermal properties of some selected compounds which can be used for the fabrication of composite fuel. The average atomic mass, A_{av} (in u), per unit cell is listed in column two. The Lattice thermal conductivity [W $m^{-1}K^{-1}$], calculated at 400 K and 2500 K are listed in column 5 and 9 respectively. The respective a and b parameters measured in W^{-1} m K and W^{-1} m units respectively are shown in columns 3-4. Debye temperature (θ in K), thermal expansion coefficient (α, in K^{-1}), Young's modulus (Y in GPa) and the minimal thermal conductivity, (k_{min} in $Wm^{-1}K^{-1}$), are listed in subsequent columns as indicated. The observations presented in this Table can be used as a guild line in selecting materials with higher thermal properties; thermal conductivity.

Table 1.1: The thermal properties of selected compounds for composite fuel fabrication

Compound	A_{av}	a	b	k_L(400 K)	θ	$\alpha \times 10^6$	Y	k_L(2500 K)	k_{min}
SiC (cubic)	20	7.66×10^{-12}	8.73×10^{-6}	286	1179	3.24	456	45.8	3.01
SiC (hex)	20	9.55×10^{-12}	9.69×10^{-6}	258	1155	3.33	440	41.3	2.96
BeO	25	6.84×10^{-12}	3.19×10^{-5}	221	1186	6.09	339	35.4	2.47
ThO_2	88	9.25×10^{-13}	1.42×10^{-4}	17.6	434	7.68	267	2.8	1.04
CeO_2	57	2.00×10^{-12}	2.11×10^{-4}	11.8	476	9.72	216	1.9	1.19

The temperature profiles and temperature gradient as a function of the radius of an enhanced thoria fuel in an operating fuel rod are presented in Figure 1.12. ThO_2 /Silicon Carbide (SiC) (Hexagonal) composite fuel which has an order of magnitude higher thermal conductivity was investigated. This investigation tends to look at important factors that contribute to enhancing lattice thermal conductivity of nuclear fuel which will be helpful in developing a safer fuel. It is assumed that the fuels were fully dense and the performance of pure ThO_2 was compared with 5vol%, 10vol% and 15vol% ThO_2/ SiC composites.

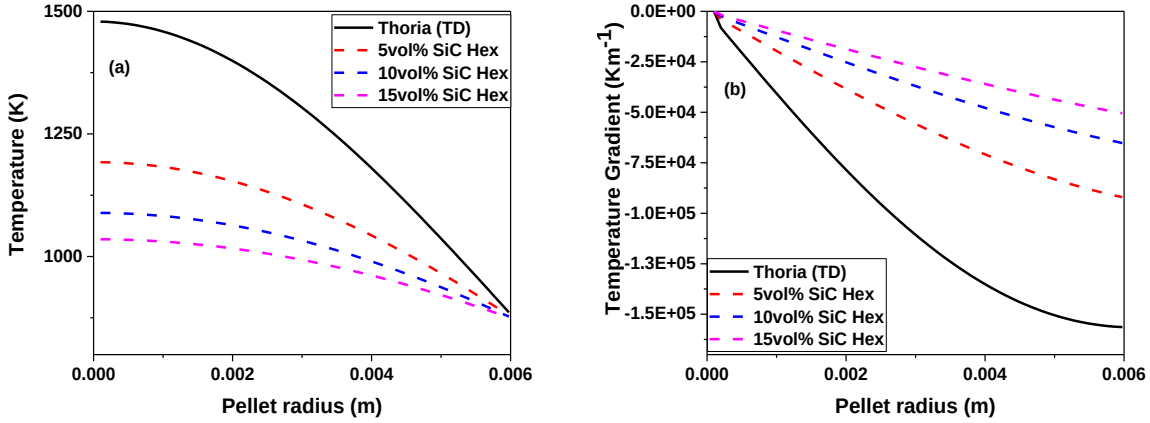

Figure 1.12**:** The predicted (a) fuel temperature Profile and (b) fuel temperature gradient for Thoria and 5vol%, 10vol%, and 15vol% SiC(Hexagonal)/ThO_2 composites, respectively

The composite fuels using high thermal conductivity materials allow a significant reduction of the central fuel line temperature and the temperature gradient within the fuel as presented in Figure 1.12. Since the addition of SiC (Hexagonal) to ThO_2 fuel bring about these reductions, it can, however, be predicted that the composite fuel would not only be safer but would also have higher longevity. However, this claim is subject to further investigation. The full investigation of this composite fuel is presented in paper 6 listed in the appendix as part of the work of the author and it is hereby not fully discussed in this thesis.

1.5.3 Uranium Dioxide (UO_2) Fuel Surrogate

Cerium Oxide (CeO_2) is a rare-earth oxide and a nonradioactive substitute material for UO_2 nuclear fuel. It is also used extensively in catalysis and fuel cell applications. CeO_2 is formed when Cerium (Ce), the most abundant of the rare-earth elements in the earth's crust, is separated from other rare-earth elements through oxidation [36] and it is also known as Ceria. Pure CeO_2 appears in pale

yellow color and has the calcium fluoride (fluorite) type structure in Face Centered Cubic (FCC) space group Fm3m over a wide range of temperature spanning from room temperature (300 K) to the melting point (2750 K) [37]. It has a lattice constant (a) of 5.411 Å. In its cubic closed-packed structural box, Ce ions occupy the vertices and faces of the unit cell and each of them is coordinated with eight Oxygen (O) ions which are arranged perfectly in the cube. In a tetrahedral arrangement, the Ce ions and O ions are paired four to one as the arrangement has each O ion surrounded by four Ce ions [38].

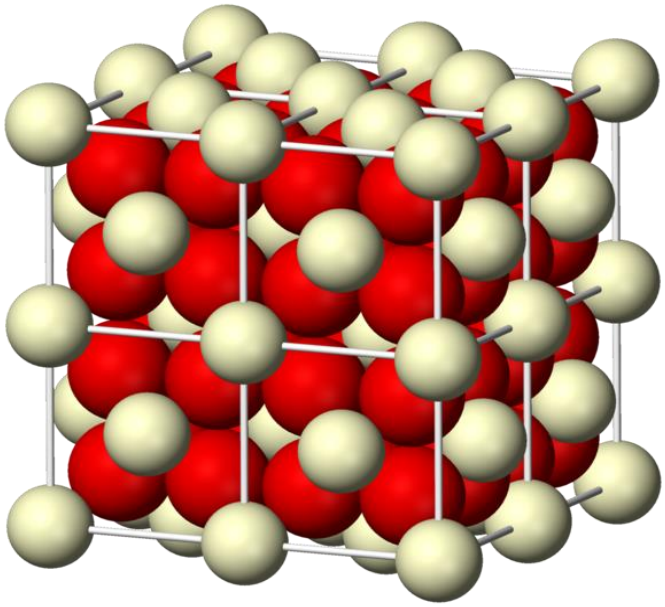

Figure 1.13: A typical fluorite type Cerium dioxide (CeO_2) structure generated by Ovito Software. The gray spheres represent Ce ions and the red spheres represent O ions

CeO_2 is used as a representative of UO_2 because they both have similar structure and properties. Both of them form crystal in a cubic fluorite phase with space group Fm3m. Ce and U cations exhibit similar charge transfer to two O anions in their hard cubic oxides. They both exhibit homologous physical, chemical, mechanical, and thermal properties. Their thermal properties are of great interest as they both respond to heat the same way. Their thermal conductivity decreases as temperature increases and their lattice parameters increase as temperature increases. Their temperature dependent thermal conductivity predominantly depends on phonon-phonon scattering with a negligible minimal electronic contribution. At 1273 K temperature, CeO_2 and UO_2 have an electronic contribution to thermal conductivity on the order of 1×10^{-3} W m^{-1} K^{-1} [39]. This

electronic contribution is below the phonon contribution in about three orders and both materials possess a positive phonon defect scattering. They both have a stable structure as they not change phase as a function of temperature but similarly change phases at high pressure [40]. CeO_2 and UO_2 break bonds at a temperature close to a melting point causing diffusion of oxygen ions in their FCC cubic structure. Apart from its non-radioactive capability which makes it a good UO_2 surrogate for experimental procedures, CeO_2 is considered as a surrogate of UO_2 because of the similar structural and thermal properties. Hence, understanding the properties of CeO_2 under extreme conditions will be meaningful for further applications of UO_2 nuclear fuel.

1.6 Thesis Objective

The objective of this thesis is to investigate the degradation of UO_2 fuel performance by structural defects and fission products, using analytical methods, molecular dynamics simulations and experimental procedure. Structural defects and fission products are the major fuel degrading conditions focused on in this work. The diffusion of atoms in the fuel lattice at extremely high temperature will be analyzed. Also, the effect of dissolved fission product on the microstructure and thermal conductivity of the fuel will be studied. Due to the radioactive nature of UO_2, and for the experimental sake, a surrogate material (CeO_2,) will be used as a representative of UO_2 fuel in this research.

This thesis is organized as follows; Chapter 2 is a literature survey of both experimental and theoretical work performed on CeO_2, ThO_2 and UO_2 nuclear fuels. It discusses the radiation condition of the nuclear reactor that affects the properties of the nuclear fuel during operations. Chapter 3 is the theoretical framework where the theories of molecular dynamics are described. Also, a general overview of all the codes and potentials used in this thesis are presented. Chapter 4 contains the analytical approach to investigating the thermal conductivity and its degradation in nuclear fuel. The results of the calculations are also presented. In Chapter 5, the properties of CeO_2 are extensively studied using molecular dynamics approach. The effect of dissolved fission product on the microstructure and thermal conductivity of CeO_2 is discussed in Chapter 6. Finally, in Chapter 7, all results obtained are summarized, conclusions are drawn and possible future work is proposed.

CHAPTER 2

LITERATURE SURVEY

2.1 Properties of nuclear fuel in nuclear reactor

During reactor operation, the fuel pellets experience significant changes in their structure and properties as fission events occur. The physical state and the chemistry of the nuclear fuel change after a few years of irradiation in the nuclear reactor. These changes affect majorly the thermal properties of the fuel which also modify the fuel performance. Nuclear fuel performance and nuclear reactor output power depend exclusively on one important thermal property; the thermal conductivity of the fuel. Thermal conductivity (K_L) is a measure of the fuel's ability to conduct heat and it is measured in watts per kelvin-meter ($W\ m^{-1}\ K^{-1}$) [41]. As the structure and composition of the fuel changes in the nuclear reactor, the thermal conductivity of the fuel is also affected and this property is either enhanced or weakened by these changes. The thermal conductivity of nuclear fuels has been studied in much depth in relation to the behavior and performance during reactor operation. Due to the importance of UO_2 in the nuclear industry, numerous experimental researches have been performed towards the provision of thermal conductivity parameters for pure UO_2. Bate *et al.* [42], Gibby *et al.* [43], Godfrey *et al.* [44], Conway *et al.* [45], Ranchi *et al.* [46], and Pang *et al*. [47] measured the variation of thermal conductivity of UO_2 as a function of temperature. Figure 2.1 shows the changes in thermal conductivity of UO_2 as a function of temperature from experimental results. The trend in experimental results suggests that the thermal conductivity of UO_2 decreases upon heating in the temperature range of 200-1400 K. Also, there have been series of theoretical predictions of lattice thermal conductivity of UO_2. Wang *et al*. [48] predicted the variation of the lattice thermal conductivity of UO_2 as a function of temperature using first principle approach while Kim *et al*. [49] studied the temperature dependence of effective lattice thermal conductivity of UO_2 using both ab-initio and classical molecular dynamics techniques.

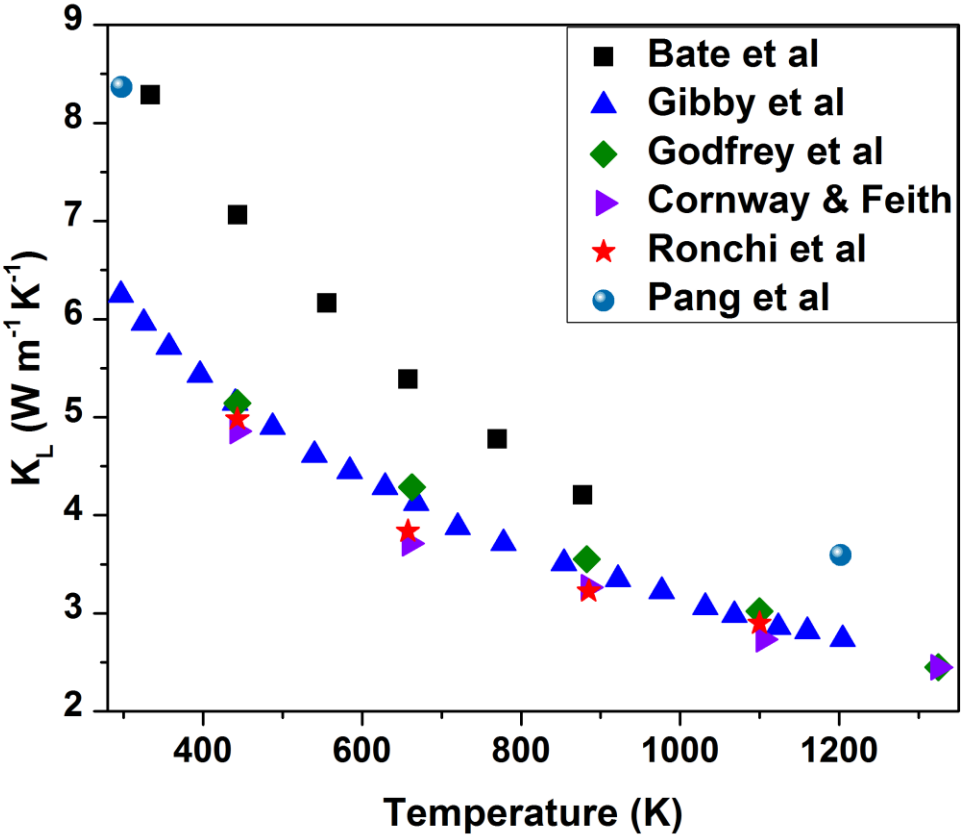

Figure 2.1: Experimental measurements of UO_2 thermal conductivity as a function of temperature [42–47]

Much effort has been made to understand the mechanisms that cause a reduction in thermal conductivity of nuclear fuel. Studying the thermal conductivity of CeO_2 under defined conditions will be meaningful for further application in UO_2 fuel as CeO_2 is often used as a surrogate of UO_2. The thermal conductivity of CeO_2 was experimentally measured by Khafizov *et al.* [50], Figure 2.2. The plot shows that like UO_2, CeO_2 also experiences a decrease in thermal conductivity values as temperature rises. The thermal conductivity of UO_2 at room temperature (300 K) is believed to be within the range of 6 W m^{-1} K^{-1} to 8.5 W m^{-1} K^{-1} as presented in Figure 2.1 while CeO_2 has thermal conductivity value of 17 W m^{-1} K^{-1} at room temperature (300 K).

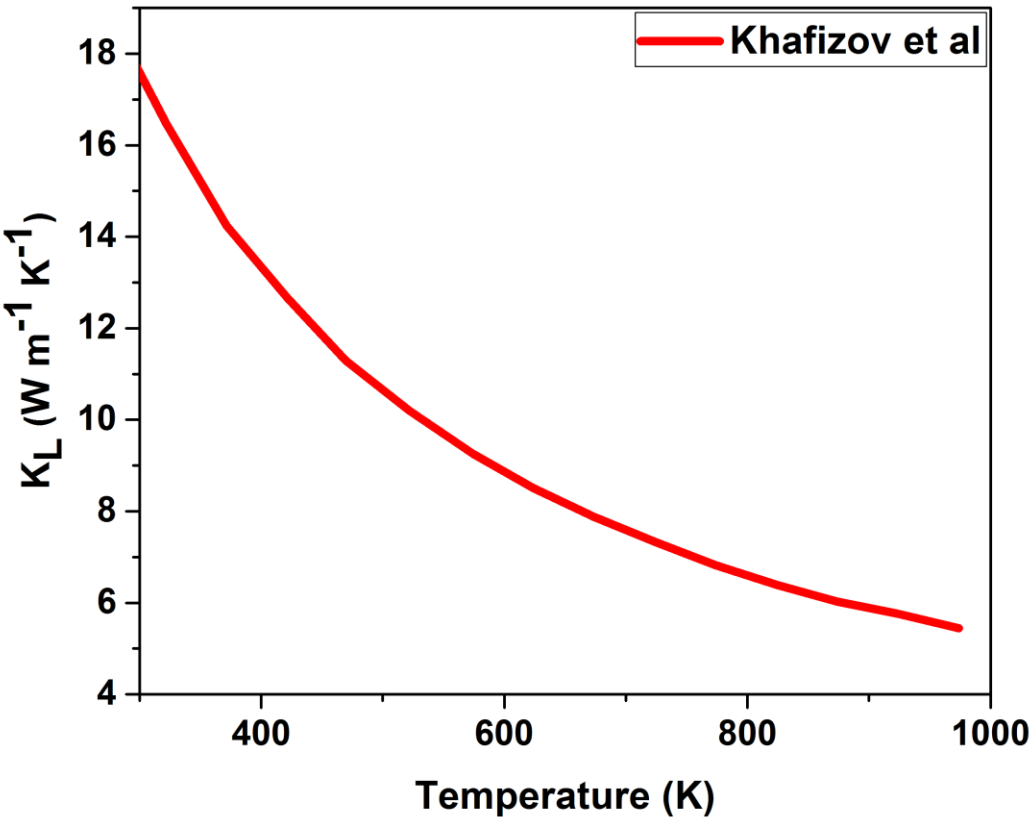

Figure 2.2: Measured thermal conductivity of CeO_2 pellet as a function of temperature by Khafizov *et al.* [50]

ThO_2 has been considered a possible replacement for UO_2 fuel in nuclear reactors due to its natural abundance and the production of lower nuclear wastes compared to that of UO_2 based fuel [51]. Apart from its relatively high occurrence, ThO_2 has high thermal conductivity value which is a good advantage over UO_2 fuel because of the risk associated with the safety of low thermal conductivity UO_2 fuel; this is a contributing risk factor associated with the safety of nuclear fuels. Low thermal conductivity fuel like UO_2 have significant demerits; one of them being the inability to completely recover during short-term nuclear reactor accident [52]. The thermal conductivity of ThO_2 has been experimentally measured by a number of researchers, but the works of Bradshaw and Mathews. [53], Moore *et al.* [54], Murabayashi *et al.* [55], Pillai *et al.* [56], Bakker *et al.* [57], and Weilbacher *et al.* [58] are presented in Figure 2.3.

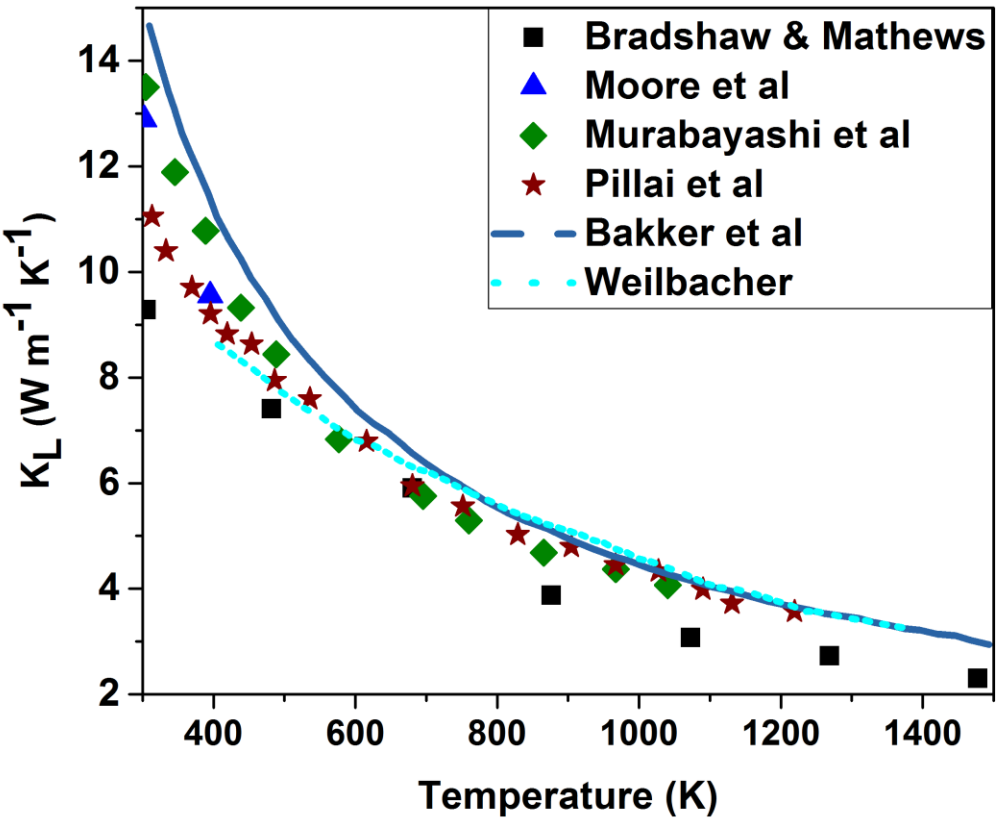

Figure 2.3: The experimentally measured thermal conductivity of ThO_2 [53–58]

2.1.1 Burnup in nuclear fuel

The structure of fuel changes with thermal conductivity as it is subjected to very harsh irradiation and thermo-mechanical environments during service. The fuel structure undergoes complex microstructural evolution as fission process creates different fission products. Rondinella *et al*. [35] describe the nuclear fuel restructuring phenomena during the nuclear reactor operation as the formation of high burnup structure in nuclear fuel. In addition to the microstructural defect caused by radiation damage, macroscopic cracking is formed in the fuel due to the thermal stresses induced by the temperature gradient. Fission product generation, bubble formation, point defect generation, cracks, swelling, embrittlement and dislocations are the common microstructural changes caused by radiation damage to fuel. Inherent changes within the fuel structure decrease its thermal conductivity, with the exception of the metallic precipitate that forms as the fuel

undergo complex processes to accommodate the newly formed species [59]. Lukuta *et al*. [34] have modeled the thermal conductivity of UO_2 fuel as a function of burnup and temperature. They develop correlation equations that considered the precipitated and dissolved fission products as the two key microstructural features of irradiated high burnup fuel. They further illustrated that the thermal conductivity of irradiated fuel matrix is not controlled by the phonon scattering as for pure UO_2 but by burnup.

2.1.2 Fission Products

According to Kleykamp [60], fission products can be classified into four groups which are also fission gases, fission product forming metallic precipitates, fission products forming oxide precipitates, and fission products dissolved as oxides in the fuel matrix. In addition, the transport behavior and the chemical state of the fission products within the fuel matrix influence important physical properties, such as thermal conductivity, swelling, creep, and melting point, of the fuel. The four categories of fission products are discussed below [60]:

1. **Fission gases –** Noble gases and other volatile elements which are highly insoluble in the UO_2 fuel matrix are known to fall into this category. These gases do not form stable secondary phases nor do they react with fission products. Br, Kr, Rb, I, Xe, Cs, and Te are some of the fission gases generated in the UO_2 fuel matrix due to fission [35] and they migrate within the fuel or create bubbles as they accumulate in pores formed within the fuel.

2. **Fission product forming metallic precipitates –** Mo, Tc, Ru, Rh, Pd, Ag, Cd, In, Sn, Sb, Se, and Te are fission product that will neither oxidize nor dissolve in the fuel matrix to form solid solutions. They however precipitate to form metallic particles in the UO_2 fuel matrices [60]. This class of fission product are insoluble in the fuel matrix and can only form a precipitate. They are known to enhance some fuel properties because of their metallic properties. Middleburg *et al*. [61] have described how Mo acts as a buffer to the hyper-stoichiometry of the fuel by reducing the solubility of many fission products in the UO_2 fuel matrix and further prevent the degradation of fuel strength by the soluble fission product.

3. **Fission product forming oxide precipitate –** Rb, Sr, Zr, Nb, Mo, Se, Te, Cs, and Ba are the fission products that form oxide precipitate because of their insoluble characteristics [60]. Additionally, these fission products exist in phases. Kleykamp *et al*. [62] reported that Ba Zr, U, and Pu are the main components belonging to the gray phase. The gray phase consists of elements that can be accommodated at two cation sites within the perovskite lattice [63] and this behavior is highly dependent on the reactor condition and history. He further stated that Bs, Sr, Cs, Mo, and Zr are the oxide precipitates forming the gray phases in high-temperature breeder reactor fuel.

4. **Dissolved oxides –** some fission products change totally the chemistry of the fuel by dissolving in the fuel matrix to form solid solutions. These fission products change the structural, physical and the thermal properties of the fuel as they modify the fuel to occupy a certain percentage of the fuel matrix. Rb, Sr, Y, Zr, Nb, La, Ce, Pr, Nd, Pm, Sm, and Eu are the fission products that are soluble in the UO_2 lattice and some new structures are formed as UO_2 accommodate these fission products. Depending on the status of the fuel, some of these fission products become insoluble at a certain percentage burn up of the fuel. Romberger *et al* [64] reported that at about 1% burnup, Zr would become insoluble in the UO_2 matrix.

2.1.3 Structural defect

The thermal conductivity of irradiated UO_2 fuel depends on the deviation from stoichiometry, the burnup, and the fractional porosity, as well as the temperature (Lucuta *et al*., 1994) [34]. Porosity is a measure of void spaces in the irradiated nuclear fuel matrix. UO_2 fuel must operate reliably for several years under extremely harsh conditions of radiation. During this period, several atoms are displaced from their original positions some of which recombined and some do not return to their initial position causing point and more complex defects in UO_2 fuel periodic structure. The positions of atoms in UO_2 fuel structure occur in repeating fixed distances which are determined by the fuel unit cell parameters but the regular patterns are interrupted by atoms missing from their regular atomic sites, causing vacancies, due to radiation damage. The number of voids or vacancies (porosity) in the UO_2 fuel is considered to play an important role among numerous factors which influence the thermal conductivity of the UO_2 fuel. Jelea *et al*. [65] studied the impact of porosity

on the thermomechanical properties of UO_2 fuel matrix using atomistic modeling. They reported that porosity modifies the thermal expansion coefficient and the elastic property of the fuel. Loeb [66] independently derived the relation which determines the effect of porosity on thermal conductivity of materials. This relation has been used by many researchers [67] but Lee *et al*. [68] observed a continuous decrease in the thermal conductivity of UO_2 as the size of pore increases and the decrease in thermal conductivity is said to be more substantial that the prediction of the analytical model proposed by Loeb.

The thermal conductivity of UO_2 is an important property of the fuel and a lot of attention have been shifted to enhancing this property because a good nuclear fuel for high-temperature application must have high melting point, good irradiation resistance, mechanical stability, and high thermal conductivity. The higher thermal conductivity of fuel will increase the power output of the nuclear reactor and prevent fuel melting during accident. As described by Szpunar *et al*. [31], high thermal conductivity of fuel will decrease the centerline temperature and temperature gradient in the fuel which will prevent central melting, enhanced fuel longevity and reduced fission gas release. Yeo *et al*. [32] illustrated that with a decrease in centerline temperature caused by the increased thermal conductivity of fuel pellet, the temperature gradient within the fuel is decreased. This also allows to reduce fission gas release and to lower a number of cracked or broken pellets due to thermal stresses.

CHAPTER 3

THEORETICAL AND EXPERIMENTAL FRAMEWORK

3.1 Molecular dynamics (MD)

Molecular dynamics (MD) simulations are a class of theoretical tool for studying the properties of assemblies of atoms in terms of their structure and the microscopic interactions between them. It is a time-dependent N-body type simulation that models the physical movement of atoms and molecules upon interaction for a fixed period of time. MD uses interatomic potentials to calculate the forces and potential energies of interacting atoms by first solving their Newton's law of motion equations to determine atomic trajectories. This is a technique where the time evolution of a set of interacting atoms in a crystal is followed by integral operation of their motion equations [69]. The interactions between particles generate forces relative to their positions while the magnitude and direction of the atomic movements are determined by the gradient of the potential energy of the atom with respect to its position. The force F_i exerted on an atom i with an atomic mass m_i and acceleration a_i within a defined system is given by

$$F_i = m_i a_i = m_i a(t) = F_i(r(t)). \tag{3.1}$$

In the above formula, r is the position of the atom. The force F_i exerted on each atom i can be expressed as the gradient of the potential energy, such that

$$F_i(r(t)) = -\nabla V_i(\mathrm{r(t)}), \tag{3.2}$$

$$-\frac{dV_i\big(r(t)\big)}{dr_i} = m_i \frac{d^2 r_i}{dt^2}\,. \tag{3.3}$$

The potential energy is a function of the atomic position of all the atoms in the system and potentials describing the interaction between atoms. In addition, the position and velocity of each atom can be used to determine the past and the future states of the system of interacting atoms once they are known. The velocities and positions of the atoms can be determined by solving their respective equations of motion (such as Equation 3.3) numerically, using the velocity Verlet integration method [70]. The velocity Verlet method uses the Taylor series expansion to

approximate the positions, velocities and the accelerations of the interacting atoms in a system by splitting a second order differential equation into two first order differential equations. The approximated quantities can be presented as

$$\boldsymbol{r}(t+\ \delta t) = \boldsymbol{r}(t) + \delta t\boldsymbol{v}(t) + \frac{\delta t^2}{2}\,\boldsymbol{a}(t) + \boldsymbol{b}(t)\delta t^3 + \ldots\ldots\ldots, \tag{3.4}$$

$$\boldsymbol{v}(t+\ \delta t) = \boldsymbol{v}(t) + \delta t\boldsymbol{a}(t) + \frac{\delta t^2}{2}\,\boldsymbol{b}(t) + \ldots\ldots\ldots, \tag{3.5}$$

$$\boldsymbol{a}(t+\ \delta t) = \boldsymbol{a}(t) + \delta t\boldsymbol{b}(t) + \ldots\ldots\ldots, \tag{3.6}$$

where **r** vector describes the position, ***v*** is the velocity and **a** is the acceleration. The unknown term ***b*** can be expressed by

$$\boldsymbol{b}(t+\ \delta t) = \boldsymbol{b}(t) + \delta t\boldsymbol{b}(t), \tag{3.7}$$

using Taylor expansion and since all other terms are known, Equations (3.4 and 3.5) can then be expressed by the velocity Verlet algorithm as

$$\boldsymbol{r}(t+\ \delta t) = \boldsymbol{r}(t) + \boldsymbol{v}(t)\delta t + \frac{1}{2}\,\boldsymbol{a}(t)\delta t^2, \tag{3.8}$$

$$\boldsymbol{v}(t+\ \delta t) = \boldsymbol{v}(t) + \tfrac{1}{2}\,[\boldsymbol{a}(t) + \boldsymbol{a}(t+\ \delta t)]\delta t, \tag{3.9}$$

respectively. The velocity Verlet algorithm yields position, velocities, and accelerations at time *t* [70,71]. This algorithm solves the Newton's equation and provides information about the positions and velocities of atoms at time *t*. This information is sufficient to determine the atomic trajectory for successive steps of movement. In this scope, Equation (3.8) is used to determine the new positions of the atoms and Equation (3.9) computes the new velocities. The trajectory obtained by molecular dynamics describes the positions, velocities, and accelerations of the atoms as they vary with time. They also provide a set of configurations by simulation of the arithmetic averages of the various instantaneous values infered by that quantity during the MD run. After an integrator, which is a finite difference scheme that moves trajectories discretely in time and describes particle positions and velocities from time t to $t+\ \delta t$, has been chosen, the time step δt also needs to be decided to guarantee the stability of the integrator. The MD simulations can be time consuming and computationally expensive because the velocity Verlet equation needs to be repeatedly solved

so that the evolution of the system can be examined with time. Simulation of the system presented here were done in time steps between 1 to 5 femtoseconds because of the computational system constraints.

During MD simulations, the temperature *T,* pressure *P,* and number of particle *N* are the main parameters that define the thermodynamic state of a system while the atomic positions and the momenta characterize the microscopic state of a system [71]. There exists a cut-off between the thermodynamic and microscopic state of a system, and these states are linked up by using the concept of the thermodynamic ensemble. An ensemble is a collection of all possible systems which have different microscopic states but have an identical thermodynamic state. It also represents all possible arrangement and momenta of a system that has a set of common extensive quantities [71]. In a thermodynamic ensemble, *T*, *P*, and *N* are the controlled thermodynamic quantities. The microcanonical ensemble (NVE), where the volume and energy of the system remain constant, is the natural choice of an ensemble of most MD simulations. However, it is inevitable that the number of atoms in the system remains the same no matter the state in which the system appears. Nevertheless, there exist different ensembles with different characteristics. The canonical ensemble (NVT) is defined by a fixed number of atoms, a fixed volume, and a fixed temperature. The NVT ensemble controls the temperature through direct temperature scaling while the volume is kept constant and it is used mostly during production runs to allow collection of data like displacement of atoms at a constant temperature. The isobaric-isothermal ensemble (NPT) is a collection of all systems whose thermodynamic state is characterized by fixed pressure, a fixed temperature and a fixed number of atoms. This ensemble is used during equilibration to control both the temperature and pressure. The temperature and pressure are kept constant as the unit cell volume is allowed to change.

In MD simulations, boundary conditions are imposed to control how particles interact within a large system of particles. Periodic boundary conditions are used to imitate the habit a bulk material and a small part of the bulk system, called unit cell, is often chosen to investigate the bulk properties of the material. The unit cell is used in such a way that it can replicate itself and be surrounded by the images of itself. The particles in the original unit cell box are repeated in each of the successive unit cells dimensions to create a super cell. The supercell box represents the bulk crystal and as the box becomes larger it creates a system which becomes closer to a true

representation of the crystal. The boundary conditions are designed in such a way that particles are allowed to interact across the boundary of the simulation box as they can exit one end of the box and re-enter from the other end.

3.1.1 Molecular dynamics flowchart

In MD simulations, there are general procedures that follow as material properties are simulated. As listed in Figure 3.1, the atomic coordinates corresponding to the bulk material structure are assigned and geometrically optimized. The geometry optimization is performed by minimizing the energy of the structure so that the final converged configuration of the structure is in the equilibrium state with zero velocities of atoms.

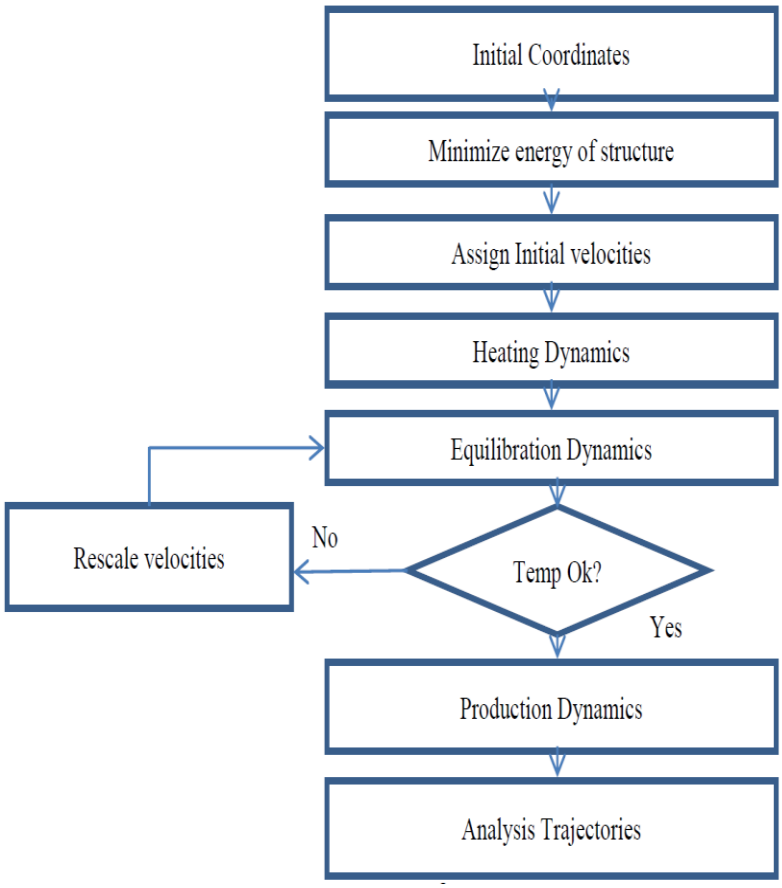

Figure 3.1: The molecular dynamics step by step simulation flowchart [72]

The converged lattice parameter is determined at the minimum energy state of the system and the calculated lattice parameter corresponds to the inter-atomic potential employed in the simulation.

The temperature of the atoms is raised to the desired level by assigning vibrational velocity to each atom so that as the atoms vibrate they can generate enough heat to raise the temperature of the system to a stabilized level. However, if the temperature in the system fluctuates too much the velocity rescale mode is applied to ascertain that a stable required temperature level is obtained. After the optimum required temperature has been achieved, the dynamics of various process parameters related to the properties of the material are then applied to the system to obtain atomic trajectories at various time steps.

3.2 Interatomic potential model

Interatomic potential plays a major role in molecular dynamics simulation. A good description of forces between interacting atoms in a system is a very important factor that characterized the ability to accurately predict the material's behavior. These potentials help predict the potential energy of a system of interacting atoms with respect to the positions of the atoms. They are translational and rotational invariant functions that do not really consider the absolute positions of atoms but only the relative positions of the interacting atoms to each other. As stated in equation (3.2), the force F_i exerted on each atom i is expressed as the gradient of the potential energy, $\nabla V_i(\mathrm{r(t)})$. Additionally, the strong exponentially attractive forces observed between N number of interacting atoms is a function of the potential energies of the atoms. Thus, the potential function V between two interacting atoms i and j at a distance r in a system of N atoms is a sum of the pairwise interactions [69,70] and it is written as

$$V\left(r_{1,\ldots\ldots\ldots}r_N\right) = \sum_i \sum_{i<j} \varphi\left(\left|r_i - r_j\right|\right), \tag{3.10}$$

where φ, a pair-potential, is the basic interaction between the nuclei of the interacting atoms and φ is a function of the distance separating the two atoms i and j. The total energy of the system can be determined by adding the independent pairwise contributions over the whole system. The pairwise interaction is described in terms of ions by short and long range Coulombic contributions. The total energy U_{ij} of the interacting ions i and j which is the summation of the short range Coulombic contribution $\varphi_{SC}(r_{ij})$ and long range Coulombic $\varphi_{LC}(r_{ij})$ [5] is given by

$$U_{ij} = \frac{1}{2}\sum_{i}\sum_{i\neq j}\varphi_{\alpha\beta}(r_{ij}), \tag{3.11}$$

$$\text{where } \varphi_{\alpha\beta}(r_{ij}) = \varphi_{SC}(r_{ij}) + \varphi_{LC}(r_{ij}), \tag{3.12}$$

and the types of the interacting atoms *i* and *j* are described as $\alpha \; and \; \beta$ respectively in Equations (3.11 and 3.12), while their interatomic separation is expressed as r_{ij}. The long range Coulombic contribution $\varphi_{LC}(r_{ij})$, which is often referred to as the Coulombic potentials, is inversely proportional to the distance separating the two interacting ions *i* and *j*,

$$\varphi_{LC}(r_{ij}) = \frac{Q_\alpha Q_\beta}{4\pi\epsilon_0 r_{ij}}, \tag{3.13}$$

where Q_α and Q_β represent the charges of the two interacting ions *i* and *j* respectively and ϵ_0 is the permittivity of free space.

There are series of approximations for short range interactions of ions. These are empirical potentials configured to approximate short range interactions based on the bonding of the system. Lennard-Jones potential, Morse potential van der Waals attractive interactions, and Buckingham repulsive interactions are the most commonly used empirical potentials for short range interactions approximations. However, to describe perfectly the behavior of atoms in metals, the interaction of atoms with their respective surrounding neighbors is considered essential. The Embedded Atom Method (EAM) is the most commonly used description of metallic systems. The Embedded Atom Method (EAM) many body interactions will be discussed briefly in the next section.

3.2.1 Embedded Atom Method (EAM)

The Embedded Atom Method (EAM) is a many-body configuration added to the pairwise interaction for the purpose of metallic system description. Daw *et al*. [73] developed this method with a view to obtaining the energy of a metal by first extracting the energy of the embedded atom. In their approach, authors embedded an atom into the local electron density provided by the remaining atoms of a metallic system and the embedding energy generated from this process is

considered to be the energy of the metal. The energy of the metallic system, where the many-body interaction is added to the pairwise description created by the electrostatic interactions between ions [74], is expressed by

$$U_{ij} = \frac{1}{2}\sum_{i}\sum_{i\neq j}\varphi_{\alpha\beta}(r_{ij}) + \sum_{i} G_i\left(\sum_{i\neq j}\rho_j^a(r_{ij})\right), \tag{3.14}$$

where the first term is the pairwise interaction, *G* is the embedding energy, and ρ^a is the spherically averaged atomic electron density. The resulting many-bodied potential ensures that the interaction between two atoms cannot be described without considering the surrounding atoms that is, each atom is embedded in a host of electron density created by the atoms in its neighborhood. The many-body potential used in this work was developed by Cooper *et al*. [5,75,76] and it employs the EAM approach for better description of material properties.

3.3 Molecular dynamics software

Computational resources used in this thesis are provided by Westgrid (West Canada Research Grid), a part of Compute Canada which provides high-performance computing resources suitable for material modeling. Westgrid provides highly efficient supercomputers that can model large system behavior with large numbers of atoms. Computational codes, like LAMMPS, GULP, and MEDEA, which apply MD principle to simulate materials properties are installed on Westgrid supercomputers. These codes/software compute Newton's motion equations as expressed in the MD principle to simulate a system of interacting atoms. The molecular dynamic codes/software used in this research work are briefly discussed in the next few sections.

3.3.1 Large-scale Atomic/Molecular Massively Parallel Simulator (LAMMPS)

LAMMPS is a classical MD code that integrates Newton's equations of motion to model systems with particles spanning from a few, to millions or billions of particles. The code, which is one of the leading forcefield-based MD codes in the world today, was developed at Sandia National Laboratories, United States and was designed to run on parallel computers that compile C++ and support MPI library [77]. LAMMPS models all collections of atoms or macroscopic particles that

fall within the three states of matter. For every LAMMPS MD calculations, an input list of initial atomic positions (coordinates) and forcefields parameter (potentials) for all atoms are required. LAMMPS is assigned with forcefields with short and long-range potentials that can model atomic systems. Soft systems like polymeric and biological systems, metallic solid-state systems and coarse-grained systems can be simulated. It imposes boundary conditions on atoms that interact via short or long-range forces to determine the type of neighbors an atom possesses in order to keep track of the nearby particles. Different physical quantities are calculated through different computational commands and such commands are provided in an input script in a language understood by the code. In the same way, LAMMPS provide output script after each calculation and such script is post processed by tools designed for various post-processing tasks.

3.3.2 Materials Exploration and Design Analysis (MEDEA)

MEDEA is a graphical visualization and atomistic-scale modeling software package for simulating materials properties. Its environment is equipped with a rich set of building and analyzing capacities with forcefields for classical simulations. Furthermore, MEDEA has a computational modular interface that is equipped with high-end computational code, like LAMMPS modules, which provides flexible calculation setups for predicting material behavior. The MEDEA LAMMPS module features a powerful flowchart interface that allows arrangement of complex calculations by connecting stages [78]. The system also automatically analyzes results, plot graphs, and conducts necessary fittings where required. MEDEA poses as the most flexible LAMMPS interface by being compatible with any LAMMPS forcefields.

3.3.3 General Utility Lattice Program (GULP)

GULP is a classical molecular dynamic computational modeling software for performing a different type of simulation on materials, for any form of matter, using boundary conditions of 0 dimension for molecules and clusters, 1 dimension for polymers, 2 dimensions for surfaces, slabs and grain boundaries, or 3 dimensions for periodic solids. The code focuses mainly on analytical solutions, using lattice dynamics method, where possible, rather than MD. A different type of forcefields can be used within GULP; the shell model is used for ionic materials, molecular mechanics is used for organic systems, the embedded atom model is used for metals and the reactive REBO potential is used for hydrocarbons [79].

3.4 Experimental technique

3.4.1 Spark Plasma Sintering (SPS)

Spark plasma sintering (SPS) is a sintering method based on high-temperature plasma (spark plasma) momentarily generated in the gaps between powder materials using the electrical discharge at the beginning of ON-OFF DC pulse energizing. The large current pulse energizing method generates four effects; spark plasma, spark impact pressure, Joule heating, and an electrical field diffusion effect. This sintering mechanism and mechanical properties of SPS sintered compact show different characteristics compared to conventional pressure assisted sintering processes. The process offers significant advantages with various kinds of new materials and consistently produces a highly dense compact in a shorter sintering time and of finer grains than conventional methods. The Cerium Oxide (CeO_2) and Cerium Zirconium Oxide (Ce_3ZrO_8) pellet sample used in this research were sintered using this technique. The CeO_2 powder was supplied by the Science Lab.com Chemical and Laboratory Equipment in Texas. CeO_2 and Ce_3ZrO_8 pellets were sintered at the University of British Columbia (Vancouver) and Queens University (Kingston), respectively.

3.4.2 Laser Flash Technique for thermal conductivity

The thermal conductivities of the pellet samples were measured using a discovery laser flash (DLF-1/EM-1300). In this method, the thermal diffusivity, a thermophysical property defined as a ratio of the thermal conductivity and the volumetric heat capacity, is first determined. With the diffusivity method, uniform irradiation of a small, disc –shaped specimen on its front face with a very short pulse of energy is applied. The time-temperature history of the rear face is recorded through high-speed data acquisition of solid-state optical sensor with the very fast thermal response, and thermal diffusivity is determined from the time-dependent thermogram of the rear face. The thermal diffusivity is given by $0.1388\ L^2/t_{1/2}$, where L is the thickness of the specimen in m, and $t_{1/2}$ is the time in seconds for the rear surface temperature to reach 50% of its maximum value. The specific heat C_p is given by, Q/ (dT.m), where Q is the energy of the pulsed laser beam, which can be determined by comparing the maximum value of temperature rise with that of the reference specimen, m is the mass of the specimen and dT is the maximum value of temperature rise. The thermal conductivity measurements in this work are conducted using the discovery laser

flash (DLF-1/EM-1300) thermal conductivity machine in the material science laboratory in the department of mechanical engineering, University of Saskatchewan.

Figure 3.2: The discovery laser flash (DLF-1/EM-1300) for thermal conductivity measurements

3.4.3 Microstructural characterization

The microstructural analysis of the pellet samples was carried out using a versatile Field Emission Scanning Electron Microscope (SEM) (Hitachi Su 6600) in the Department of Mechanical Engineering, University of Saskatchewan. The Hitachi Su 6600 model, as presented in Figure 3.3, is also equipped with an Oxford Instruments NordlysNano Electron BackScatter Diffraction (EBSD) detector that acquires diffraction patterns using AZTEC 2.0 data acquisition software. The AZTEC 2.0 software is compatible with the EBSD detector and the Oxford Instruments channel 5 post processing software. The Hitachi Su 6600 also provides imaging and Energy Dispersive Spectrometry (EDS) analysis. This capacity of the system allows different microstructural analysis

such as phase characterization, element distribution, grain size distribution and morphology of the pellet samples.

Figure 3.3: The Scanning Electron Microscope (SEM) (Hitachi Su 6600) at the material science laboratory

3.4.4 X-Ray Diffraction (XRD)

The ultimate quality diffraction data of the pellet samples were obtained using a Bruker D8 Discover X-ray diffractometer. The XRD system uses the constructive interference of monochromatic X-rays technique involving an X-ray tube, a sample holder, and an X-ray detector to analyze the structure of materials. This technique involves X-rays being generated by a cathode ray tube and directed toward the sample. These X-rays are filtered before use to produce a monochromatic radiation. This whole technique employs Bragg's Law ($n\lambda=2d\sin\theta$) as the incident rays interact with the samples to produce a constructive interference. The XRD machine

scans the sample through a range of 2θ angles and the rays diffracted by the sample are collected by the X-ray detector for analysis. This process allows to measure the phase composition, orientation of grains, crystalline structure, and stress in the specimen.

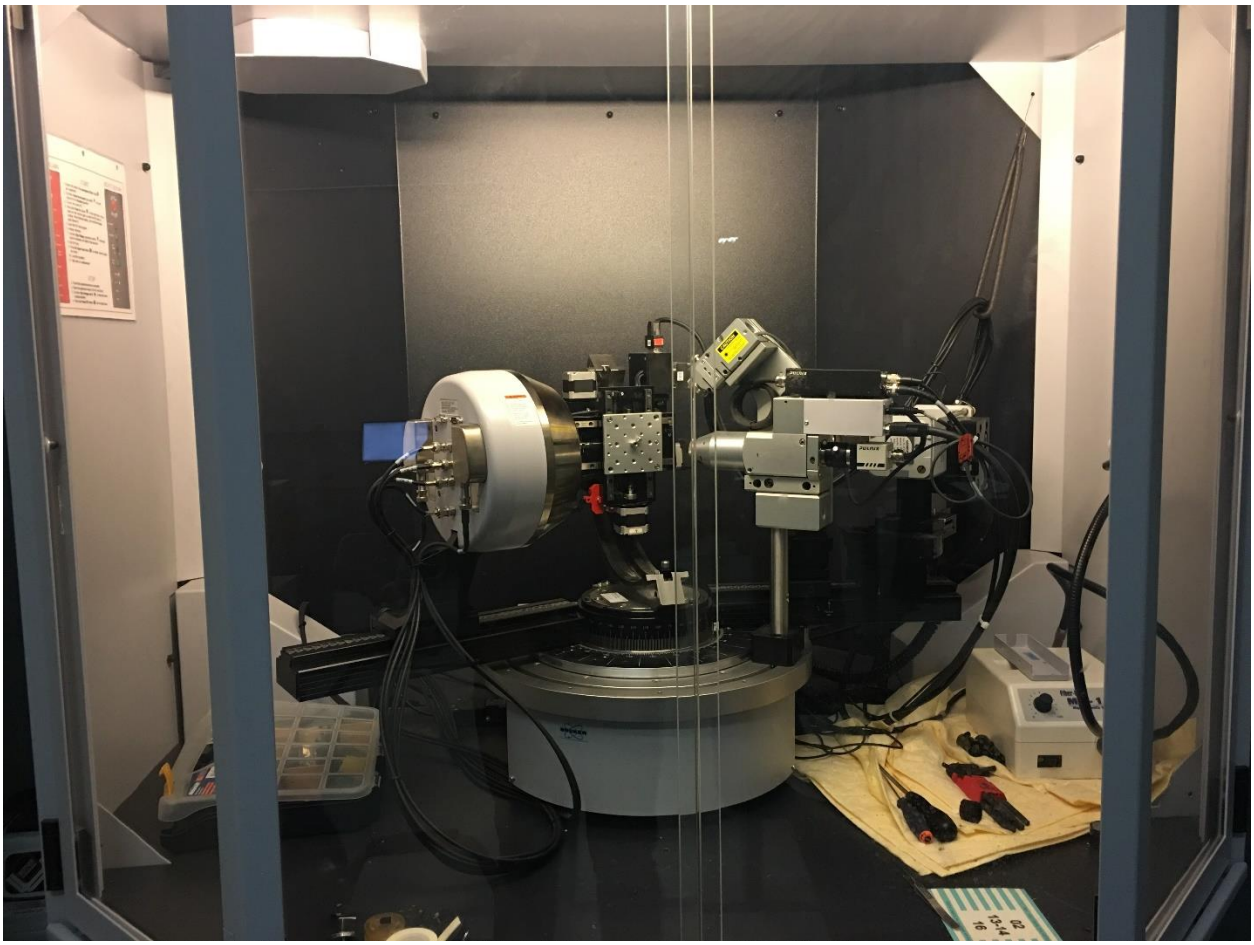

Figure 3.4: The Bruker D8 Discover X-ray diffractometer at the material science laboratory, University of Saskatchewan

3.4.5 Experimental procedure

Powdered samples were sintered using the Spark Plasma Sintering (SPS) technique. The sintering process involves the loading of powder into a die while cylindrical plugs are inserted into both ends of the die. This allows for the pressure loading after the die has been placed in a furnace. In this work, the process parameters such as the ramping rate, holding time, axial pressure and the sintering temperature were optimized to get a dense pellet. These pellet samples were later characterized for various thermal and microstructural properties as described within the flowchart shown below.

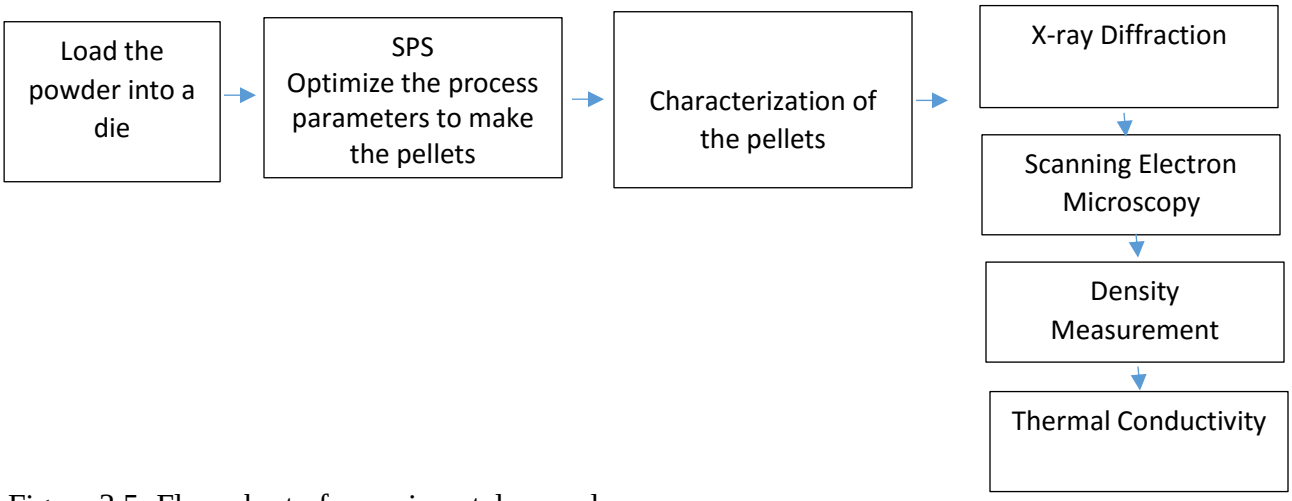

Figure 3.5: Flow chart of experimental procedure

Surface and bulk analytical techniques were deployed during the characterization of the CeO_2 and Ce_3ZrO_8 pellet samples. X-ray diffraction (XRD) was used in determining sample composition. Scanning Electron Microscopy (SEM), Energy Dispersive Spectrometry (EDS) and the Electron BackScatter Diffraction (EBSD) techniques were utilized in analyzing the particulate distribution of CeO_2 and Ce_3ZrO_8, the grain size, and the microstructural phases present in the materials, respectively. The density of the pellet was determined using the Archimedean immersion technique and the thermal conductivity was measured with the aid of a Laser flash technique. The results obtained from the experimental procedure and the computational modeling are discussed in the next chapters.

CHAPTER 4

DEGRADATION OF THERMAL CONDUCTIVITY IN NUCLEAR FUEL

4.1 Brief introduction

Thermal conductivity (K_L) is the measure of a material's ability to conduct heat. For insulators (ceramics), heat conduction takes place via one process: vibration of atoms. Before any material is subjected to heat, the atoms within it vibrate about their equilibrium position while the energy penetrates via the subatomic close to the heat source. As the atoms begin to vibrate with greater vibrational amplitude slowly farther down the material, the whole material heats up. These atomic vibrations increase as energy transfer is enhanced via collision; heat penetrates down the material until the large amplitude vibration arrives to the other end of the material. The phenomenon responsible for conduction of heat in an insulator is known to be phonon contribution (vibration of atoms). However, heat conduction can only occur in a material if there is a temperature difference between two parts of the same material [80]. The rate of heat flow P is the measure of the thermal energy flowing through the cross-sectional area of a material per unit time. That is,

$$P \propto A \frac{\Delta T}{\Delta x}, \tag{4.1}$$

$$P = \frac{\Delta Q}{\Delta t}, \tag{4.2}$$

where Δx is the thickness of the material, cross-sectional area is A, and ΔT is the temperature difference between two parts of the material. The rate of heat flow P is the amount of heat ΔQ transported through the material for a certain time Δt and it is measured in Watts (W). We can rewrite Equation (4.1) to follow the law of heat conduction by introducing a proportionality constant **K** as follows:

$$P = -\mathbf{K} A \frac{dT}{dx}, \tag{4.3}$$

where the proportionality constant **K** is the coeficient of thermal conductivity of the material (measured in W $m^{-1} K^{-1}$) while the term dT/dx is the variation of temperature with position (also referred to as temperature gradient). Thermal conductivity is an important property in materials for high-temperature applications. Different materials possess varying thermal responses; and the difference in their thermal conductivity defines the thermal responses for system subjected to heat treatment. In some materials, thermal conductivity increases with temperature, while the contrast is the case in other materials. For materials that operate at extremely high temperature, such as nuclear fuel in the nuclear reactor, their performance depends so much on their thermal conductivity and the factors that affect it. The thermal conductivity of nuclear fuels can be determined using different approaches, including but not limited to experimental procedure, computational modeling and some semi-empirical equation.

UO_2 is the traditional nuclear fuel for present generation of nuclear reactors while ThO_2 has been considered as a possible replacement for UO_2 fuel for future generation of nuclear reactors. Attention began to shift to ThO_2 as a possible safer replacement for UO_2 nuclear fuel after the Fukushima nuclear accident which clearly showed the need for a safer nuclear fuel. CeO_2 is considered as a good and flexible surrogate material for predicting structural and thermal properties of these two nuclear fuels (UO_2 or ThO_2). However, the three materials have a similar crystal structure, FCC cubic structure, and are expected to have similar responses to heat treatments with thermal conductivity decreasing as temperature increases. In this work, the thermal conductivity of CeO_2, ThO_2, and UO_2 has been investigated as a function of temperature and fraction of the fuel theoretical density or porosity using semi-empirical equations. The results of this investigation are presented in section 4.3. This chapter of the thesis is organized as follows. Section 4.1 gives a brief introduction to thermal conductivity. Section 4.2 deals with the methodology employed to investigate the materials. Section 4.3 presents the results obtained, including discussion. Finally, section 4.4 contains the summary of this chapter of the thesis.

4.2 Methodology

Theoretical research has led to improvements in equations which makes it possible to measure the thermal conductivity of nuclear fuels (UO_2 and ThO_2) and the effect of porosity on the aforementioned property of these materials using semi-empirical or correlation equations. Bakker *et al*. [57] and Popov *et al*. [81] developed semi-empirical equations for computing thermal

conductivity of ThO_2 and UO_2 nuclear fuel, respectively. These equations address the thermal conductivity of these materials as a function of temperature, and the effect of porosity is accounted for by separate equations. The recommended equation by Popov *et al*. [81] for the thermal conductivity $K_L(T)$ at temperature T (K) of 100% dense solid UO_2 is expressed as

$$K_L(T) = \left[\frac{115.8}{7.5408 + 17.692t + 3.6142t^2} + 7410.5t^{-\frac{5}{2}} \exp\left(-\frac{16.35}{t}\right)\right] [\mathrm{W\ m^{-1}\ K^{-1}}], \quad (4.4)$$

$$t = \frac{T(K)}{1000}. \quad (4.5)$$

The effect of porosity on the thermal conductivity of solid UO_2.is described by the well-known Maxwell-Eucken factor (FM)

$$FM = \frac{1 - P}{1 + 2P}. \quad (4.6)$$

The parameter P in Equation (4.6) represents the fraction of porosity in the solid UO_2 fuel. The total thermal conductivity $K_L(T)$ is multiplied by the FM factor to account for the effect of porosity after an appropriate porosity fraction P has been chosen.

The correlation equation by Bakker *et al*. [57] is used to evaluate the thermal conductivity of ThO_2 as a function of temperature, and the Bakker's expression is presented as

$$K_L(T) = \left[\frac{1}{A + BT}\right] [\mathrm{W\ m^{-1}\ K^{-1}}], \quad (4.7)$$

$$F = (1 - P)^{1.5}, \quad (4.8)$$

where A and B in Equation (4.7) are constants and they are equal to 4.20×10^{-4} mK/W and 2.25×10^{-4} m/W, respectively. The two parameters A and B are independent of the temperature T but are associated with the contribution of phonon defects (A) and phonon-phonon (B) scattering to the

mean path. Equation (4.8) accounts for the effect of porosity on the thermal conductivity of solid ThO_2 and the parameter *P* in Equation (4.8) denotes the fraction of porosity in solid ThO_2. Likewise, the total thermal conductivity K_L (*T*) is multiplied by the F factor to account for the effect of porosity on thermal conductivity of ThO_2 after an appropriate porosity fraction P has been chosen.

4.3 Results and Discussion

The thermal conductivity of UO_2 fuel as a function of temperature and increasing porosity (5% and 10%) is calculated using the semi-empirical equation proposed by Popov *et al*. [81], Equations (4.4) and (4.6), Figure 4.1.

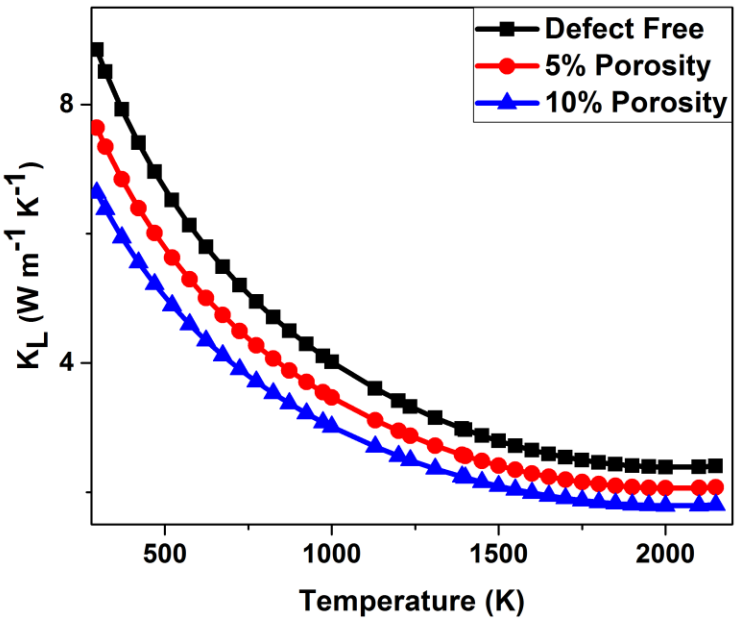

Figure 4.1: The calculated thermal conductivity of UO_2 fuel as a function of temperature and porosity using the semi-empirical equation proposed by Popov *et al*. [81]. The black, red and blue curves correspond to no porosity, 5% and 10% of porosity, respectively

The trend of data in the figure reveals that thermal conductivity of UO_2 fuel decreases at higher temperatures and porosity of fuel. These are the conditions, increasing temperature and porosity, that occur during the reactor operation and they affect both the efficiency and performance of the

UO_2 nuclear fuel. According to Figure 4.1, the fuel with porosity has a degraded thermal conductivity. The 5% porosity of the fuel reduced the thermal conductivity by 14% and the reduction due to 10% porosity is 25%. These thermal conductivity calculations approximate the changes in the conductivity of the nuclear fuel during reactor operation as irradiation and nuclear fission processes change the structure of the nuclear fuel.

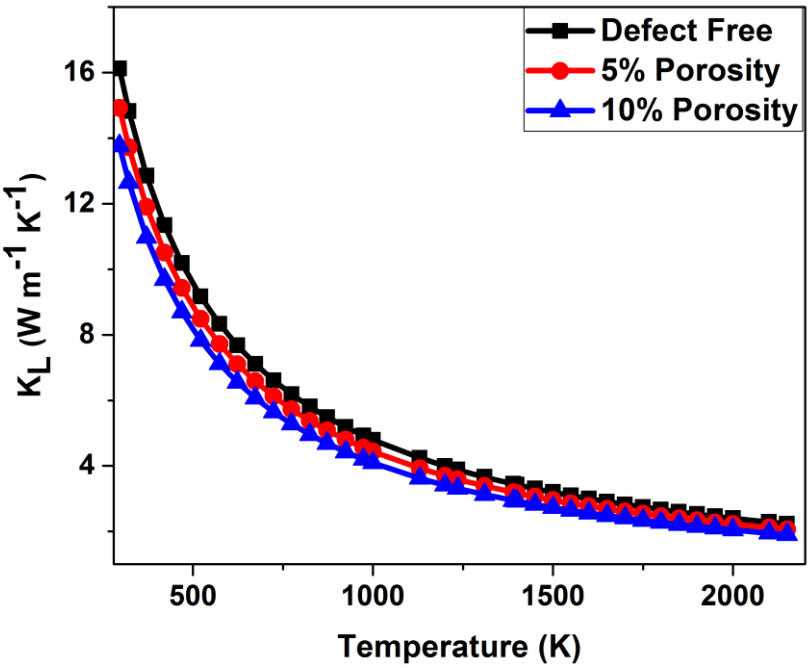

Figure 4. 2: The calculated thermal conductivity of ThO_2 as a function of temperature and porosity using the correlation equation proposed by Bakker *et al*. [57]

As a possible replacement for UO_2 fuel for future generations of nuclear reactors, the behavior of ThO_2 must also be studied under the same conditions as UO_2 fuel. ThO_2 is known to possess a better thermal conductivity than presently used UO_2 nuclear fuel. Nuclear fission process is expected to have a similar effect on ThO_2 as UO_2. However, it will be interesting to evaluate if ThO_2 have a better thermal conductivity characteristic when responding to increasing porosity. Figure 4.2 reveals the variation of calculated thermal conductivity of ThO_2 with temperature and porosity derived from Equations (4.7) and (4.8). The percentage porosity effect on ThO_2 thermal conductivity was also calculated. As expected, the porous ThO_2 also has degraded thermal

conductivity but not as strongly observed in UO_2. ThO_2 do not only have a better thermal conductivity at zero porosity but also at 5% and 10% porosity. The calculated effect of 5% porosity on ThO_2 is evaluated to be 7% reduction in thermal conductivity and the effect of 10% porosity is associated with 15% reduction in thermal conductivity. The observed percentage degradation for ThO_2 halves that of UO_2 nuclear fuel; this implies that ThO_2 is a better material under porosity investigation.

CeO_2 is a perfect nonradioactive surrogate material for predicting the structural and thermal properties of both ThO_2 and UO_2, and as such, it can be theoretically and experimentally deployed to evaluate the properties of both materials under extreme conditions (at high temperature and when the structure is defective) [82,40]. Additionally, understanding the properties of CeO_2 under extreme conditions will be meaningful for further applications of ThO_2 and UO_2 as nuclear fuel. Therefore, the thermal conductivity of CeO_2 is also calculated using correlation equation as a function of porosity. This is also accomplished by comparing its calculated thermal conductivity with those of ThO_2 and UO_2. Khafizov *et al*. [50] have previously reported the experimental determination of the thermal conductivity of 100% dense CeO_2. In this work, the effect of porosity on its thermal conductivity is calculated using Equation (4.8) by Bakker *et al*. [57]. Figure 4.3 presents the variation of thermal conductivities of 100% dense CeO_2, ThO_2, and UO_2 as a function of temperature. It is revealed that CeO_2, ThO_2, and UO_2 possess a similar thermal behavior. As the temperature increases, the thermal conductivity of the three materials decreases in a similar fashion. Their thermal conductivity exhibits a decreasing relationship with increasing temperature which can be partly linked to the relationship between thermal conductivity and lattice vibrations (phonon contribution) [83]. As the temperature is increased the atoms in the lattice vibrate with a higher amplitude which results in higher phonon scattering and structural disorder. Since lattice vibrations behave in a wave-like manner and are impeded by structural disorder, thus, the thermal conductivity will decrease with increasing temperature.

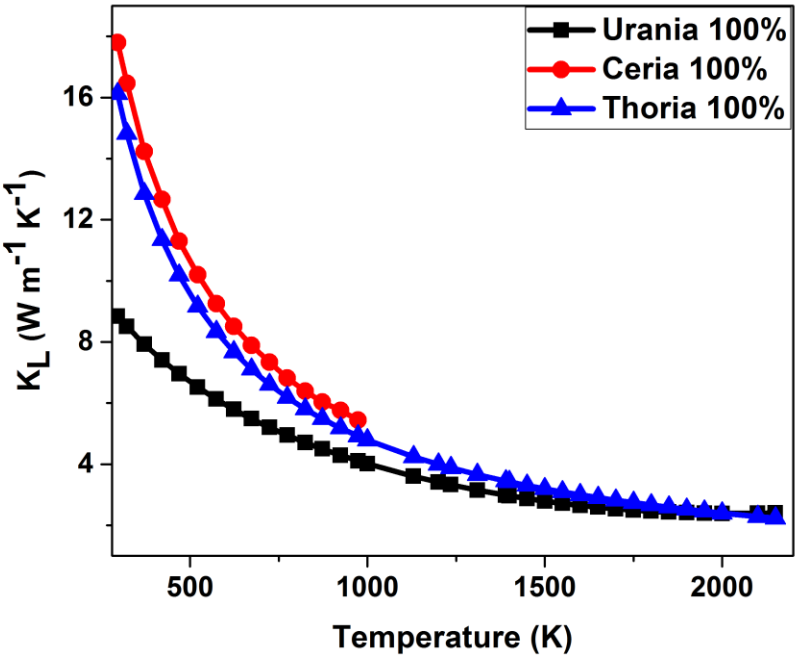

Figure 4. 3: The comparison between the calculated thermal conductivity of 100% dense CeO_2, ThO_2, and UO_2 using the semi-empirical /correlation equation proposed by Bakker *et al*. [57] and Popov *et al*. [81]

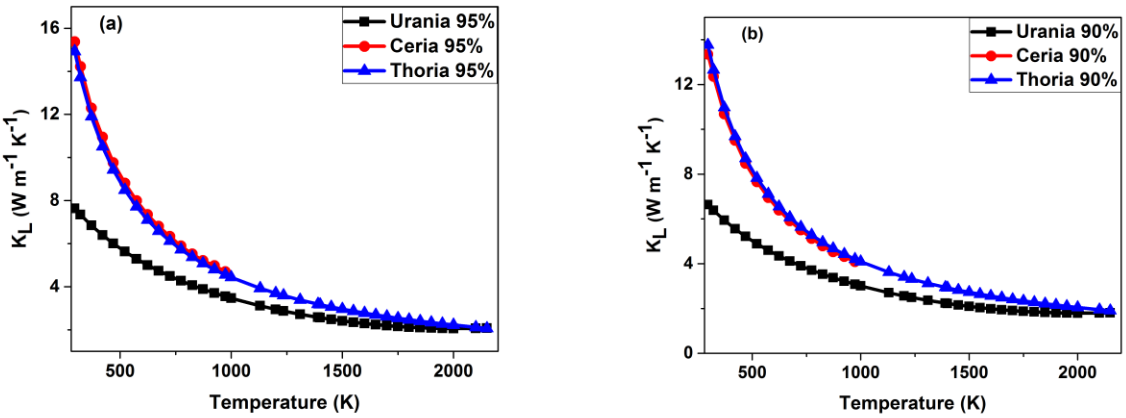

Figure 4. 4: The comparison between the calculated thermal conductivity of CeO_2, ThO_2, and UO_2 with (a) 5% porosity and (b) 10% porosity using the semi-empirical /correlation equations

The thermal conductivity of CeO_2 as a function of 5% and 10% porosity is calculated and compared to the thermal conductivity of ThO_2, and UO_2 (Figure 4.4 (a) and (b)). As similarly observed for ThO_2 and UO_2, the thermal conductivity of CeO_2 also decreases with increasing porosity.

4.4 Summary

The thermal conductivities of CeO_2, ThO_2 and UO_2 have been investigated using semi-empirical/correlation equations. It is obvious that CeO_2 does not only mimic the thermal conductivity of ThO_2 and UO_2 as a function of temperature but also as a function of porosity. Since this is well established using semi-empirical/correlation equations, simulating the thermal properties of CeO_2 using computational methods becomes a fundamental way forward to understanding better the behavior of UO_2 nuclear fuel. The next chapter will focus mainly on properties of CeO_2 as a representative of UO_2 nuclear fuel. The study highlights the conditions that cause degradation in the properties of UO_2 nuclear fuel in the nuclear reactor.

CHAPTER 5

MOLECULAR DYNAMICS STUDY OF THE PROPERTIES OF CeO_2

5.1 Brief introduction

The structural and thermal properties of CeO_2 is studied using integrated computer simulations requiring a set of computer models; lattice and classical molecular dynamics. These models allow for several theoretical analyses, including but not limited to, the computation of interactions between atoms, the description of atomic motions and analysis of the relationship of these motions to the macroscopic quantities of interest. Different potential models are verified with series of calculations and the predicted properties are then compared with available experimental data. This operation is similarly conducted in comparison with other available theoretical data in order to establish the suitable potential for the theoretical CeO_2 study. The potential comparison is carried out between the EAM many body potentials by Cooper *et al*. [75] and Buckingham two body potentials by Woodley *et al*. [84] by predicting lattice parameters, thermal expansion, and thermal conductivity. The degrading effects of porosity and fission gases on the thermal conductivity of CeO_2 are studied using the suitable potentials. This is a representative study to investigate the thermal conductivity and its degradation by porosity and fission gases in UO_2 nuclear fuel. Section 5.1 gives a brief introduction while section 5.2 deals with the methodology employed to investigate the material. The results obtained from this study are discussed in section 5.3. Finally, section 5.4 contains the summary of this chapter.

5.2 Methodology

The fluorite FCC cubic structure of CeO_2 with 12 atoms (4 Ce and 8 O atoms) and equal lattice parameters ‘a’, ‘b’, and ‘c’, are widely reported [85]. In this work, the geometry of the structure was first optimized at the ground state level and at room temperature using both GULP and LAMMPS codes. A Buckingham forcefield generated by Woodley *et al*. [84] using a generic algorithm was optimized for CeO_2. The optimization of the forcefield was performed using GULP which ensured the atomic positions and cell parameters were relaxed in order to obtain the required lattice parameters of the CeO_2 structure at the minimum energy level. The optimized Buckingham forcefield was converted to an LAMMPS useable Buckingham interatomic two body potential and geometry optimization was performed once again at the ground state level (O K). The lattice

parameter of the CeO_2 fluorite structure was optimized at room temperature by raising the temperature of the system to 300 K as the atomic positions and cell parameters are varied. The room temperature structural optimization calculation was carried out in the NPT ensemble with Nose-Hoover thermostat and barostat [86–88] where temperature and pressure were kept constant as the volume of the structure is allowed to change. The MD simulations were carried out on an 8 x 8 x 8 CeO_2 fluorite unit supercell (6144 atoms) with a fixed time step of 5 fs. A large number of atoms make the calculations more accurate however consumes much more simulation time. The NPT calculation was carried out for 2500 ps thereby ensuring enough time for the large system to reach equilibrium and the calculated volume is averaged over the total time of the simulation. The obtained lattice parameters are listed in Table 5.1.

Series of NPT calculations were further conducted on the heated CeO_2 fluorite unit supercell to estimate the response of the structure to heat using the EAM potential. The system is heated from 100 K to 2100 K temperature at 200 K intervals to estimate the inherent thermal expansion. For every simulation, the systems of 5 x 5 x 5 supercell (1500 atoms) were held for 250 ps to minimize the simulation time and the volume was averaged over the simulation period. The calculated volume at each temperature was used to determine the lattice parameter as a function of temperature. The thermal expansion results obtained from these calculations are presented in section 5.3.2.

The thermal conductivity of CeO_2 is predominantly from phonon contributions alone and as such do not have any electronic contributions. The lattice thermal conductivity of CeO_2 can be adequately determined using the equilibrium classical MD techniques together with the Green-Kubo linear response formalism [89] as implemented in LAMMPS MD simulation code. The Green-Kubo Heat Current Autocorrelation Function (HCACF) decay along a particular direction is expressed as

$$K_{l,\alpha} = \frac{V}{k_B T^2} \int_0^\infty \langle J_\alpha(0) * J_\alpha(t) \rangle \, dt, \quad \alpha = x, y, z, \tag{5.1}$$

while the total HCACF decay averaged over the three (x, y, and z) directions is given by

$$K_{l,\alpha} = \frac{V}{3k_B T^2} \int_0^\infty \langle \boldsymbol{J}(0) * \boldsymbol{J}(t) \rangle \, dt, \tag{5.2}$$

where the parameter V represent the volume of the simulation domain, T is the temperature, $\langle J_\alpha(0) * J_\alpha(t) \rangle$ is the HCACF along a particular direction and $\langle \boldsymbol{J}(0) * \boldsymbol{J}(t) \rangle$ is the total HCACF in all directions. The heat current vector **J** is fully expressed as

$$\mathbf{J} = \frac{1}{\mathrm{V}} \left[\sum_i e_i \mathbf{v}_i - \sum_i \mathbf{S}_i \mathbf{v}_i \right] = \frac{1}{\mathrm{V}} \left[\sum_i e_i \mathbf{v}_i - \sum_{i<j} \left(\mathbf{f}_{ij} \cdot \mathbf{v}_j \right) \mathbf{X}_{ij} \right], \tag{5.3}$$

$$\mathbf{J} = \frac{1}{\mathrm{V}} \left[\sum_i e_i \mathbf{v}_i - \frac{1}{2} \sum_{i<j} \left(\mathbf{f}_{ij} \cdot (\mathbf{v}_i + \mathbf{v}_j) \right) \mathbf{X}_{ij} \right]. \tag{5.4}$$

where e_i and $\mathbf{v}_i$ are the energy and velocity of particle (atom) *i* respectively, and $\mathbf{X}_{ij}$, and $\mathbf{f}_{ij}$ are the interatomic separation and the forces between two particles *i* and *j*, respectively. Equation (5.2) is the expression for Green-Kubo lattice thermal conductivity $K_{l,\alpha}$ for an equilibrium structure and it is used in this work to predict the thermal conductivity of CeO_2 as implemented in LAMMPS using both the EAM and Buckingham interatomic potentials. A system consisting of 8 x 8 x 8 conventional unit cell involving 6144 atoms was considered for performing the LAMMPS MD simulations. The system is heated between 300 K and 1500 K temperature at 200 K intervals to calculate the thermal conductivity. The Verlet leapfrog algorithm was adopted for the calculation while the Nose-Hoover thermostat and barostat was used to control the system temperature and pressure. The system was first simulated in a constant number of atoms, pressure, and temperature (NPT) ensemble for 2500 ps to ensure it reached equilibrium at the desired temperatures; then the ensemble was switched into a constant volume and temperature NVT ensemble and ran for 2500 ps. The HCACFs were computed along with an NVE ensemble calculation which generate 12500 ps raw heat current data at every calculation. The thermal conductivity value is computed, averaged, and outputted at the end of each simulation process. The calculated thermal conductivity values are discussed in section 5.3.3.

Mean-Squared Displacement (MSD) is the measure of the average distance an atom or group of atoms in a crystal lattice is displaced from its original position. MSD for an atom or group of atoms is computed by LAMMPS including some complicated events that pushes atoms out of limits of the periodic boundaries set in the simulation. Computing MSD requires the computation of a vector of four quantities where the first three elements are the square of the displacements of the atoms in the three dx, dy, and dz directions. The displacements are summed and averaged over the atoms in the group. The total squared displacement, (dx*dx + dy*dy + dz*dz), which is the fourth component is also summed and averaged over the atoms in the diffusion group. The diffusion coefficient (D) of the diffusing atoms which is related to the Einstein relation is shown as

$$D = \lim_{t\to\infty} \frac{\langle R^2(t)\rangle}{2dt}, \tag{5.5}$$

$$\langle R^2(t)\rangle = \langle |[R(t+t_0) - R(t_0)]^2| \rangle_{t_0}, \tag{5.6}$$

where t indicates time, t_0 is the average over all possible initial times, $\langle R^2(t)\rangle$ is the Mean-Squared Displacement (MSD) and d is the dimensionality of space (d = 3 for bulk diffusion). Equation (5.5) can be evaluated from the respective slope of the MSD versus time plot. MedeA interface post-process the Mean-Squared Displacement (MSD) data as the average overall initial times (t_0) such that time t does not exceed 50% of the total time length. The dependence of the diffusion coefficients on temperature can be described by the Arrhenius equation as follows:

$$D_i = D_o e^{-E_A/(RT)}, \tag{5.7}$$

$$InD_i = InD_o + \left[\frac{-E_A}{RT}\right], \tag{5.8}$$

$$InD_i = \frac{-E_A}{R}\left[\frac{1}{T}\right] + InD_o, \tag{5.9}$$

where D_i is the diffusion coefficient of a species i, D_o is the maximum diffusion coefficient at infinite temperature, $E_A$is the activation energy, and R is the universal gas constant (8.314 J mol^{-1} K^{-1}). The Arrhenius equation can be verified by plotting the natural logarithm of the diffusion

coefficients against the reciprocal of temperature and fitting Equation (5.9) to a linear equation of the plot to evaluate the value of the activation energy E_A of the diffusing atoms.

An 8 x 8 x 8 supercell of the conventional unit cell of a CeO_2 system consisting of 6144 atoms (2048 Ce and 4096 O atoms) was used for the diffusion calculations. The CeO_2 system was optimized and thermalized to raise the temperature of the system to the desired level. The calculations were performed at a lower temperature to gradually observe the movement of the atoms up to a temperature close to melting temperature (2750 K) of the CeO_2 system. The system is heated between 400 K and 2600 K temperature at 200 K intervals using the Verlet leapfrog algorithm, Nose-Hoover thermostat and barostat at a constant number of atoms, pressure, and temperature (NPT) ensemble for 2500 ps before calculating the diffusion behavior of the atoms. The EAM many-body potential was utilized for this study and the MSD calculations for the diffusing atoms was set to run for 7500 ps at the end of every thermalization run. The Mean-Squared Displacement (MSD) data of every calculation is post-processed to average the overall initial times (t_0) and the time t does not exceed 50% of the total time length. The MedeA diffusion module calculates the diffusivity using the middle 50% of the MSD value such that first 25% and the last 25% of the MSD values are thrown away. Additionally, the best MSD data are believed to be the middle 50% data because it is expected that they capture the real condition of the diffusing atoms and as such a very large total simulation time is used. Section 5.3.7 contains the results obtained from these calculations.

5.3 Results and Discussion

5.3.1 Structural properties of CeO_2

Geometry optimization was carried out in LAMMPS code using both the EAM many body and Buckingham two body potentials at the ground state level and at room temperature. The Buckingham forcefield was first optimized for CeO_2 using GULP code before converting it to a LAMMPS useable Buckingham two body potentials. The forcefield optimization in GULP also produces a lattice parameter for CeO_2 at the ground state level. The calculated lattice parameters are presented in Table 5.1. As revealed within this result, the lattice parameters prediction from LAMMPS MD simulation from the two set of potential compared well. The EAM potential predicted a lattice constant of a = 5.413 Å and the magnitude of this parameter is in good agreement

with the experimentally measured value (5.410 Å) reported by Duclos *et al*. [90] at room temperature (300 K).

Table 5.1: The calculated lattice parameter of CeO_2 from MD simulations in comparison with the experimental value

Temperature	Buckingham forcefield	Buckingham potential	EAM potential	Experiment [90]
0 K	5.411 Å	5.411 Å	5.397 Å	-
300 K	-	5.424 Å	5.413 Å	5.410 Å

However, the Buckingham potential has slightly overestimated the lattice parameter of CeO_2 in comparison with the lattice parameter measured experimentally. The lattice parameter prediction is only the first step in potential comparison as other calculations were carried out to choose the best potential suitable for this computational study.

5.3.2 Thermal expansion

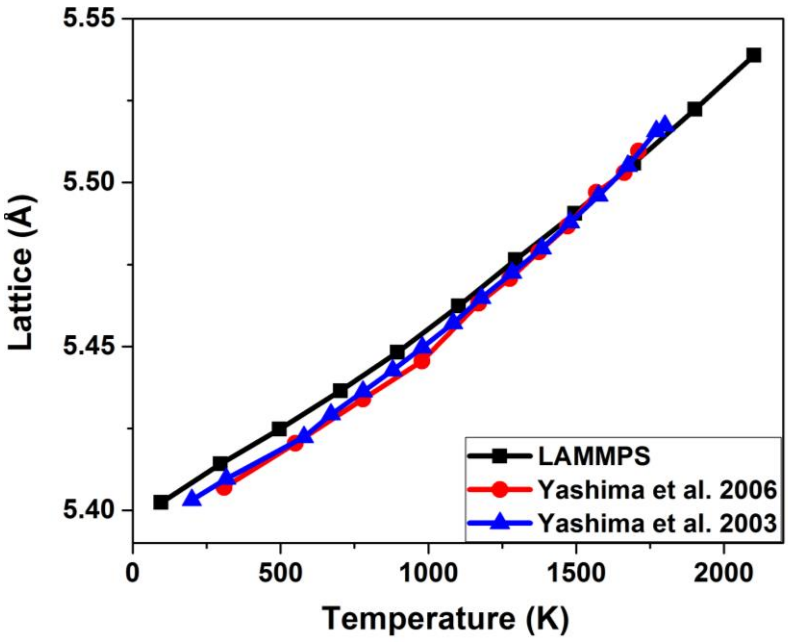

Figure 5.1: Comparison of the LAMMPS calculated thermal expansion of CeO_2 with experimental (blue line) and theoretical (red line) work by Yahsima *et al*. [91,92]

Series of NPT calculations were further conducted on the heated CeO_2 fluorite unit supercell to estimate the response of the structure to heat using the EAM many body potentials. A lattice parameter closer to the experiment was obtained from the EAM many body potentials before being deployed for the prediction of other associated parameters at varying temperatures. It is expected that the lattice parameter of the CeO_2 fluorite structure will change with temperature. From the results of the calculations, it can be revealed that the calculated lattice parameters of CeO_2 are comparable with those previously reported in experimental [91] and theoretical [92] studies (Figure 5.1). The prediction of lattice parameter by LAMMPS MD using the EAM potential up to 2200 K temperature have a good agreement with Yashima's work [91,92] (showing validation of this thermal expansion prediction) except for slight differences. The prediction slightly overestimated the lattice parameters at low temperatures but shows an excellent agreement at high temperatures.

5.3.3 Thermal conductivity

The EAM many body potentials and the Buckingham two body potentials both predicted the temperature dependence of lattice thermal conductivity for CeO_2 structure and the predictions indicate a reduction in thermal conductivity with increase in temperature as expected. Figure 5.2 presents the comparison of the results obtained from the MD simulation using the EAM and Buckingham potentials with the experimentally measured thermal conductivity of CeO_2 by Khafizov *et al*. [50]. The Buckingham two body potentials overestimated the lattice thermal conductivity of CeO_2 when compared with the available experimental data [50] and this is so because the two body potentials do not cater for the long-range phonon interactions within the CeO_2 lattice. However, the EAM many body potentials accurately predicted the lattice thermal conductivity of CeO_2 as the result obtained from the MD simulation using this potential have a good agreement with the experimental data. The results are compared up to 1000 K temperature to match the available experimental data but results at a higher temperature up to 1500 K are presented in the later section of this chapter. It is evident, from Figure 5.2, that the EAM many body potentials have a better thermal conductivity prediction than the two body Buckingham potential and as such, it is then considered for other thermal conductivity studies. However, it does not necessarily mean that two body potentials have a generally poor thermal conductivity

prediction capability as many two body potentials have predicted accurately the properties of materials in previous studies.

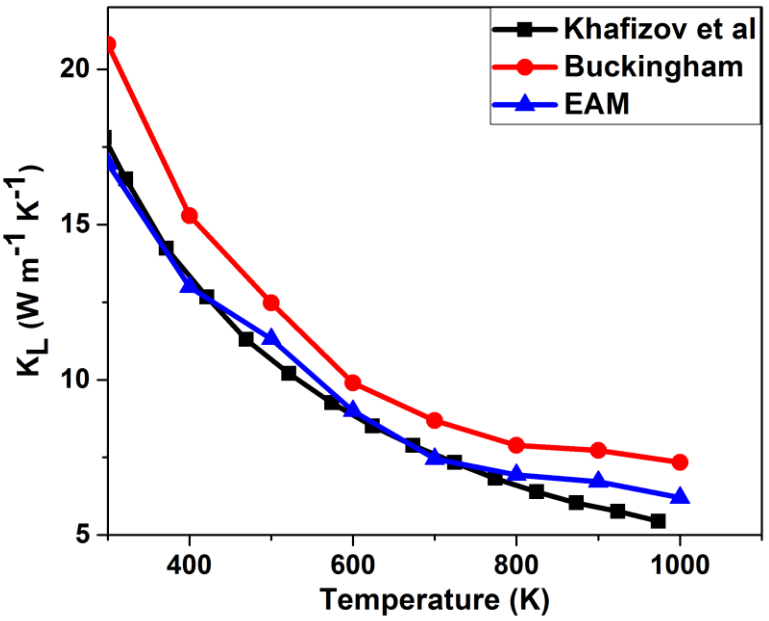

Figure 5.2: The temperature-dependent of the LAMMPS calculated lattice thermal conductivity of CeO_2 using both the EAM and Buckingham potential compared with experimental data reported by Khafizov *et al*. [50]

It is then important to perform an adequate potential comparison to choose the best potential possible rather than making inaccurate assumptions. After the EAM potential has been established as the better potential for CeO_2, the calculations to investigate the degradation in thermal conductivity of CeO_2, as a representative of UO_2, by structural defect is performed using the EAM potential. The investigation into degrading thermal conductivity of CeO_2 by porosity, fission gases and dissolved fission products is discussed in the next sections.

5.3.4 Degradation of thermal conductivity by porosity

Porosity has been observed in UO_2 nuclear fuel as a result of sintering practice, irradiation defects, and fission gas release. Due to irradiation, the physical state of the UO_2 nuclear fuel is affected as pores are generated in the fuel. The porosity increases over few years and the performance of the fuel is declined. As an important UO_2 fuel property, the thermal conductivity is affected by

porosity but it is not well understood how badly it is affected. For experimental purpose, CeO_2 is employed as a representative of UO_2 fuel to study the effect of porosity on thermal conductivity. Therefore, the effect of porosity on the thermal conductivity of CeO_2 is studied using both experimental and theoretical approach, and the results obtained will be discussed.

A molecular dynamics study to relate the effect of porosity on the thermal conductivity of CeO_2 is implemented in LAMMPS. The effect of porosity on the thermal conductivity of CeO_2 was simulated using an 8 x 8 x 8 supercell with a resulting 6144 atoms, and porosity was induced on the large CeO_2 system by carefully removing an appropriate number of atoms in a proper proportion, between 1% and 5% at interval of 1%, to mimic porosity evolution in the UO_2 nuclear fuel. Figure 5.3 presents a typical defective CeO_2 structure with 5% porosity.

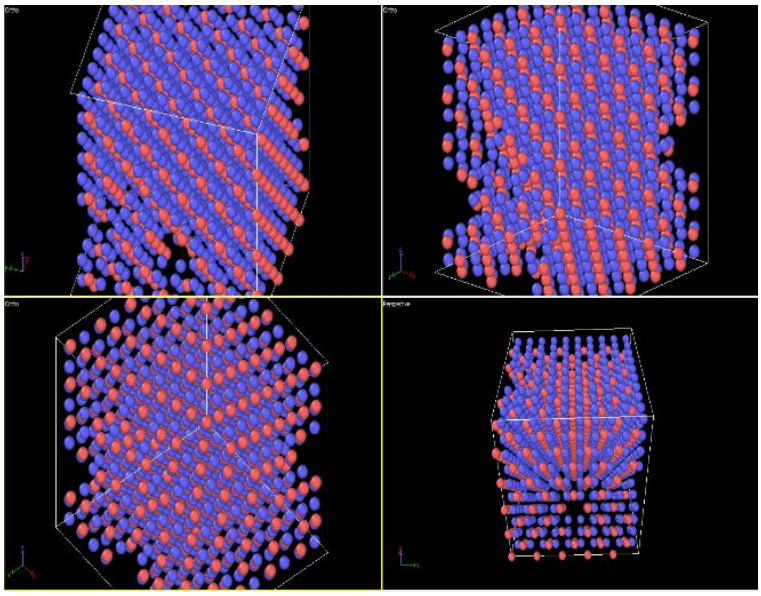

Figure 5.3: The crystal structure of CeO_2 + 5% porosity

The 6144 systems of atomic coordinates were generated and CeO_2 atoms were removed to generate pores in the system. The atoms were removed in such a way to generate charge neutrality, where for every single cerium (Ce) atom two oxygen (O) atoms were removed to balance the charge difference. The percentage porosity was calculated over the total number of atoms to know exactly how many atoms to remove for each percentage porosity evolution. The system was equilibrated after every porosity change to see if the porosity is stable. The pores were carefully monitored throughout the calculations to ascertain that they remain in the structure during the thermal conductivity calculations. The sizes of the pores may change at extremely high temperature

because of oxygen diffusion. The EAM many-body potential was utilized for this study, which enabled a good reproduction of a range of thermal conductivity property up to the melting temperature for CeO_2. The system is heated from 300 K to 1500 K temperature at 200 K intervals using the steps and time previously described in section 5.2 and the thermal conductivity is calculated using the Green-Kubo formalism as previously illustrated. The thermal conductivity is theoretically calculated for CeO_2 with 1% to 5% porosity and the thermal conductivity for CeO_2 pellet samples with 37.88%, 39.17%, and 42.80% porosity were experimentally measured.

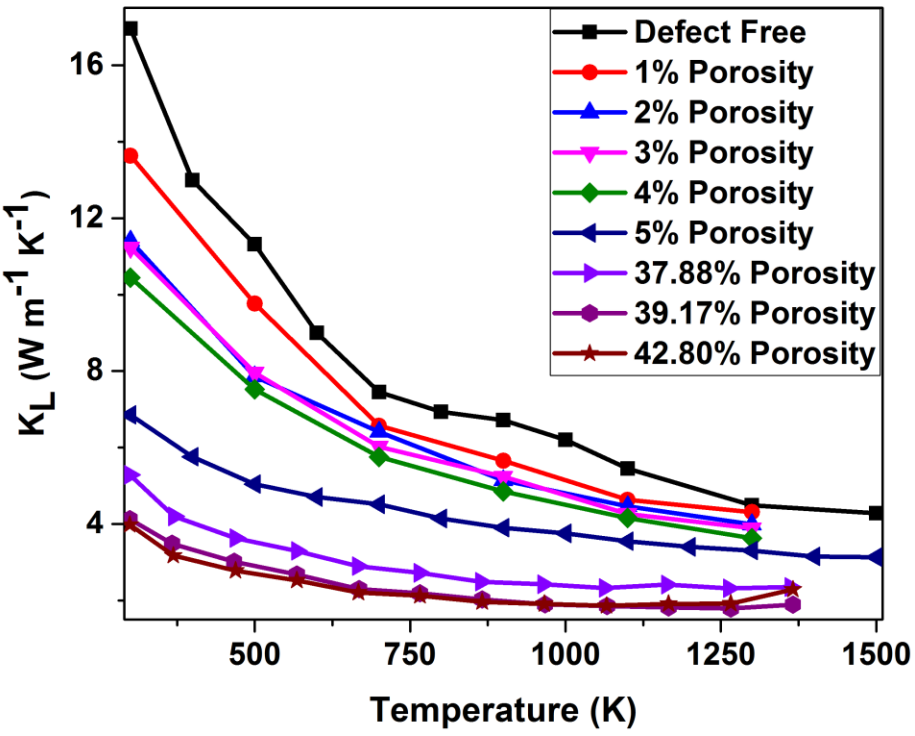

Figure 5.4: The calculated and measured thermal conductivities of CeO_2 at eight different levels of porosity. The 1%, 2%, 3%, 4% and 5% porosity concentration were calculated using LAMMPS and the 37.88%, 39.17% and 42.80% were measured using the Laser flash technique

The pure CeO_2 powdered sample was sintered using the Spark Plasma Sintering (SPS) technique as briefly described in chapter 3. The CeO_2 pellet samples were sintered to have different porosities. The samples have regular shape sizes, with the length of 1.27 cm, width of 1.27 cm and varying thickness, to fit the thermal conductivity sample holder. The porosity of the samples was

studied using the Archimedes principle and three samples with 37.88%, 39.17%, and 42.80% porosity were prepared for thermal conductivity measurements by applying a graphite spray to the surfaces of the sample and leaving the sample to dry before measuring the thermal conductivity. The thermal conductivity of CeO_2 pellet sample was measured using the Direct Laser Flash (DLF) methods as implemented in the discovery laser flash thermal conductivity machine. The results of the computational and experimental studies are presented in Figure 5.4.

The results from the two studies were compared with the calculated thermal conductivity of defect free CeO_2. The result from both computational and experimental studies clearly suggests that the thermal conductivity of CeO_2 is degraded with increasing porosity. As presented in Figure 5.4, the thermal conductivity of CeO_2 is drastically reduced as the percentage of porosity is increasing in the material. The thermal conductivity of CeO_2 is dependent on the phonon group velocity of the atoms in the crystal and it is impeded by crystal disorderliness. The degraded thermal conductivity due to porosity can be centered on the deviation of the CeO_2 lattice from a clean lattice due to porosity; that is, thermal conductivity is reduced with an increase in lattice disorder. This disorder generates an additional phonon scattering that hinders heat transport mechanism and lowers the phonon mean free path causing degraded thermal conductivity in the non-uniform lattice. In Figure 5.4, the thermal conductivity of CeO_2 is degraded at 300 K by 20%, 28%, 60%, 69%, and 77% for materials with 1%, 4%, 5%, 37.88% and 42.80% porosity, respectively. The porosity effect is reduced at high temperatures as percentage comparison of the degraded thermal conductivity becomes smaller. The effect of 1%, 4%, and 5% porosity on the thermal conductivity of CeO_2 at 1300 K temperature is estimated to be 4%, 19%, and 27% respectively. This result mimics the behavior of UO_2 fuel in the nuclear reactor. The performance of the fuel is deteriorated by increasing porosity in the fuel due to irradiation process during service. The effect of fission gases on thermal conductivity is also studied as one of the conditions that affect the performance of the UO_2 nuclear fuel.

5.3.5 Degradation of thermal conductivity by fission gases (Xe and Kr)

To make a proper assessment of the present UO_2 nuclear fuel and to better correlate the degrading condition and thermal conductivity, the effect of fission gases (e.g. Xe and Kr) on the thermal conductivity of CeO_2 is studied. It is well known that during fission process in the nuclear reactor, fission gases are generated as the fuel is irradiated and these gases are known to collect inside the

pores generated in the nuclear fuel. They have a direct effect on the performance of the fuel. The thermal conductivity of CeO_2 is now investigated with the fission gases in the CeO_2 cubic system to account for the effect of these gases on the thermal conductivity. The Xe and Kr fission gases were placed in the pores earlier generated in the CeO_2 structure to mimic the fission gases collected in the pores of the nuclear fuel. Figure 5.5 (a) and (b) present the structural image for CeO_2+Kr and CeO_2+Xe respectively. The system remains charge neutral after the gases were introduced into the structure as the gases are charge neutral. The amount Xe and Kr in the system were also in percentages as MD simulations were performed and the thermal conductivity calculated for the system. The system of 6144 atoms altogether was equilibrated and thermalized before thermal conductivity was calculated using the EAM many-body potential. For the Xe and Kr gases in the system, the newly developed tabulated empirical potential by Cooper *et al*. [93] was employed. The tabulated empirical potential describes the fission gases behavior and their impact on thermal conductivity of the CeO_2 structure. Thermal conductivity, Green-Kubo formalism, was calculated for a CeO_2 system with 1% Kr, 5% Kr and 5% Xe using the EAM many body potentials and the Xe and Kr empirical potential. The results of this calculation are presented in Figure 5.6 in comparison with the defect-free structure.

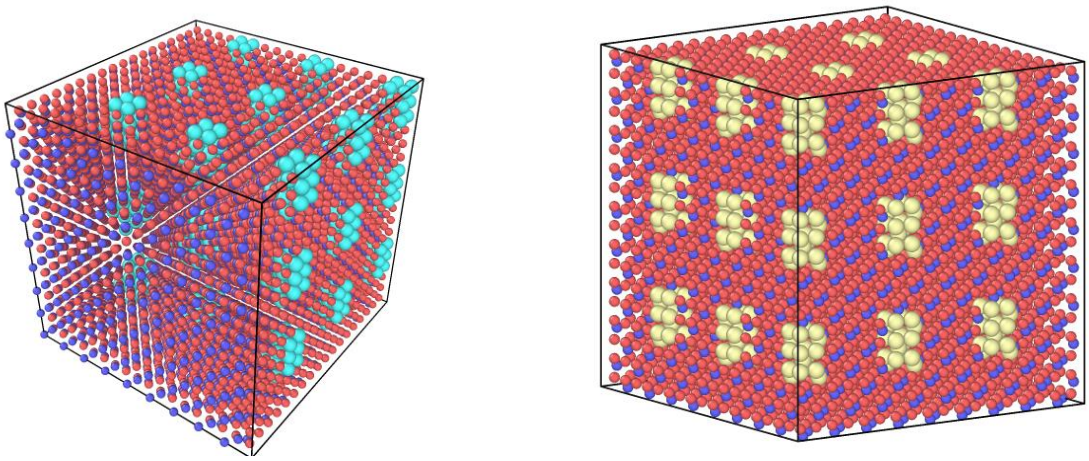

Figure 5.5: The crystal structure of CeO_2 + (a) 5% Kr (b) 5% Xe where the light blue and yellow spheres are the Kr and Xe atoms, respectively

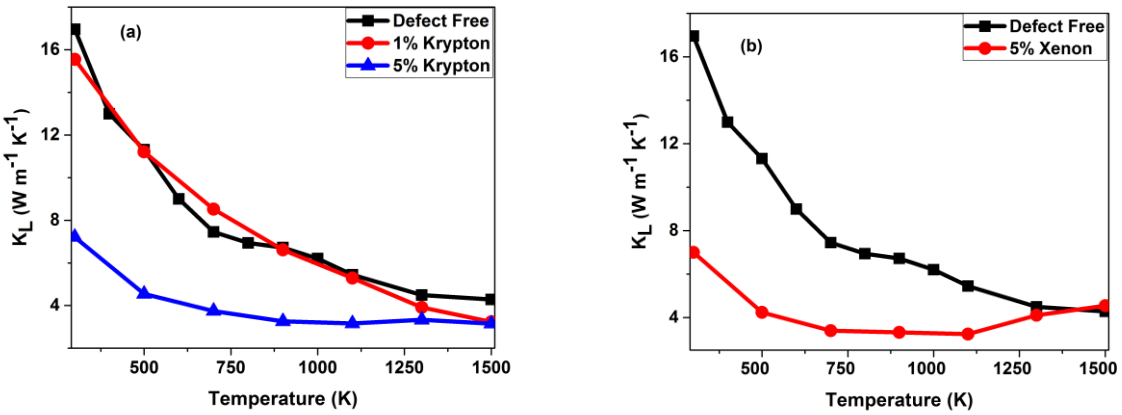

Figure 5.6: The LAMMPS calculated thermal conductivities of CeO_2 with (a) two different concentrations of Kr gas and (b) one concentration of Xe gas

Figure 5.6 (a) presents the thermal conductivity of a perfect CeO_2 structure in comparison with 1% and 5% Kr gas structure. The Kr fission gas in the CeO_2 lattice degraded thermal conductivity when compared with the thermal conductivity of the defect free CeO_2 lattice. The thermal conductivity of CeO_2 is reduced by 8% with 1% Kr gas inclusion and by 57% with 5% Kr gas inclusion in the CeO_2 lattice at 300 K temperature. At high temperature, 1100 K, the percentage thermal conductivity degradation is estimated to be 3% for 1% Kr and 42% for 5% Kr. In Figure 5.6 (b), the inclusion of 5% Xe gas degraded the CeO_2 thermal conductivity by 59% at 300 K temperature and by 41% at 1100 K temperature. The degradation in the thermal conductivity CeO_2 with the inclusion of 5% Kr and Xe gases is comparably smaller when compared to the thermal conductivity of the CeO_2 structure with empty pores. At 1300 K temperature, the thermal conductivity CeO_2 is degraded by 5% porosity, 5% Kr gas, and 5% Xe gas by 27%, 26%, and 9%, respectively. This comparison suggests that the thermal conductivity of CeO_2 is slightly enhanced when the pores are filled with fission gases in comparison with the CeO_2 structure with empty pores. However, the thermal conductivity is degraded when compared with a perfect CeO_2 lattice. The thermal conductivity of CeO_2 samples with fission gases cannot be measured as it is difficult to trap the fission gases in the samples for thermal conductivity measurement and as such, there is no experimentally measured thermal conductivity value for the comparison.

From this representative CeO_2 study, it is clearly evident that the performance of UO_2 nuclear fuel in nuclear reactors are affected by several factors. Discussing the effect of the earlier stated fission

conditions on thermal conductivity present a vivid understanding as to what happened to the nuclear fuel in a nuclear reactor and to clearly establish the factors to consider when building a safer nuclear fuel for present and future generation of nuclear reactors. Having a safer nuclear fuel will ensure that nuclear accidents are averted in nuclear reactors during operations. However, nuclear accidents in nuclear reactor occur at a very high temperature beyond reactor operating temperature and it is important to also understand what happens to the nuclear fuel at this temperature before the fuel finally melt the core of the reactor to cause an accident. The circumstances of the UO_2 nuclear fuel, using CeO_2 as a representative, at extremely high temperatures and a moment away from the nuclear reactor accident where thermal conductivity can no longer control the fuel behavior will be discussed in the following section.

5.3.6 Oxygen pre-melting in CeO_2 lattice

During nuclear reactor accident, at an extremely high temperature (near UO_2 nuclear fuel melting temperature), the physical and chemical states of nuclear fuel begin to change. Later scenarios lead to total melt of the nuclear reactor core and accidents are imminent. Oxygen (O) pre-melting will be initiated within the UO_2 lattice at a certain temperature; this process involves the bond breakage (by the O atoms) from uranium atoms while also diffusing within the UO_2 crystal lattice. To better understand this phenomenon, the diffusion of O atoms in CeO_2 lattice is studied using MD simulation. This study provides vivid information about the required energy and temperature for O atoms to break bonds and start to diffuse in the CeO_2 lattice. In order to properly examine the diffusion of O atoms in CeO_2 lattice, the Mean-Squared Displacement (MSD) method, as implemented in LAMMPS MD code, was employed to monitor the motion of the O atoms. However, results from standalone LAMMPS are not accurate enough to predict oxygen diffusion as LAMMPS does not properly average the position of the atoms over the total time of simulations and as such good number of data are thrown away. MedeA [78], a computational modular interface that is impacted with LAMMPS diffusion module which calculates the motion of a group of atoms in a crystal structure is employed. The MedeA LAMMPS diffusion module features powerful post-processing ability and as such covers for the inability of standalone LAMMPS to do proper averaging. The oxygen diffusion calculation was ran using MedeA interface with its inbuilt LAMMPS MD code and all results are post-processed after each run to obtain a properly averaged

data. The computational methodology of the Mean Squared Displacement (MSD) method has been previously discussed in section 5.2.

It is observed that at temperatures below 2000 K the oxygen atoms only move about their respective position, that is they do not dissociate themselves from the cerium atoms, and as such diffusion of oxygen atoms is yet to occur. Figure 5.7 shows that diffusivity of oxygen atoms has not yet occurred at temperatures between 400 K and 1800 K.

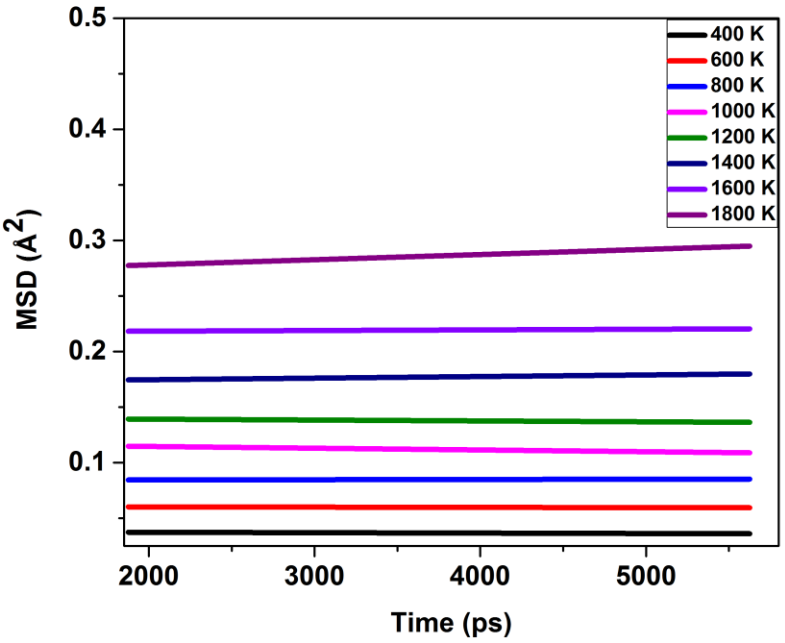

Figure 5.7: The LAMMPS calculated Mean-Squared Displacement (MSD) of oxygen in CeO_2 lattice for a temperature range of 400 – 1800 K

The horizontal lines for each temperature in Figure 5.7 indicate that the group of O atoms does not leave their respective position throughout the time of simulation. The position of the O atoms is constant at temperature below 1800 K. However, at 1800 K the position of the O atom begins to experience a slight change as few O atoms begin to jump from their initial position but the majority of the atoms still remain at their initial position as they have not acquired enough energy to break bonds from the cerium (Ce) atoms. From 2000 K to 2600 K temperature it was found out that the MSD of O atoms were linearly dependent on time which indicates that O atoms are mobile. The

diffusion of O atoms in CeO_2 lattice started occurring at 2000 K temperature and the diffusivity increases as temperature increased up to 2600 K. The MSD data for temperature range (2000 to 2600 K) are presented in Figure 5.8.

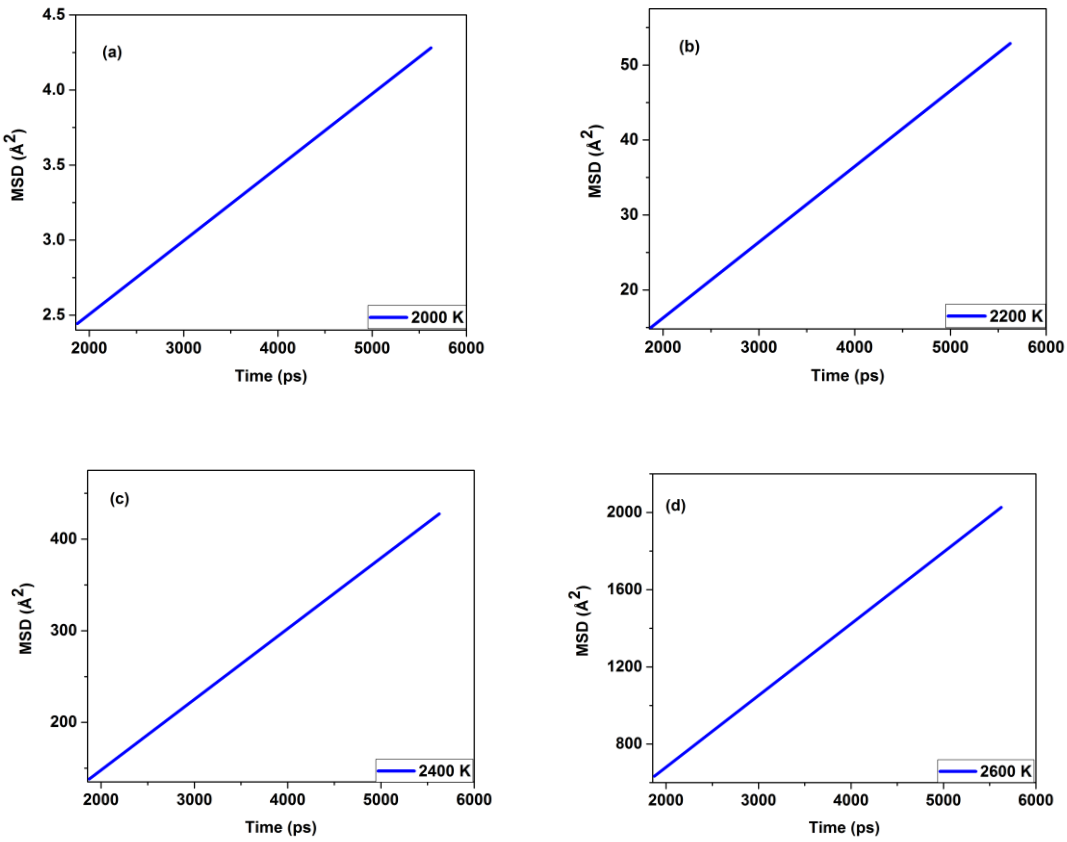

Figure 5.8: The LAMMPS calculated Mean-Squared Displacement (MSD) of oxygen atoms in the CeO_2 lattice for (a) 2000 K, (b) 2200 K, (c) 2400 K, and (d) 2600 K temperature

Figure 5.8 indicates that as temperature increases the rate of diffusion of O atoms increased also and the coefficient of this diffusion is expected to follow the same trend. The O diffusion coefficients for the 2000-2600 K temperature range is evaluated using the MSD relation obtained from the respective slopes of the MSD versus time plots. The evaluated diffusion coefficients for the temperature range is presented in Table 5.2.

Table 5.2: The calculated diffusion coefficients as function of temperature

Property	2000 K	2200 K	2400 K	2600 K
D x 10^{10} (m^2 s^{-1})	0.0082	0.1682	1.2852	6.1906

The O atoms diffusion temperature dependence is verified using the Arrhenius equation (Eq. 5.7) by plotting the natural logarithm of diffusion coefficients against the reciprocal of temperature. The plot which is fitted to a linear equation is presented in Figure 5.9.

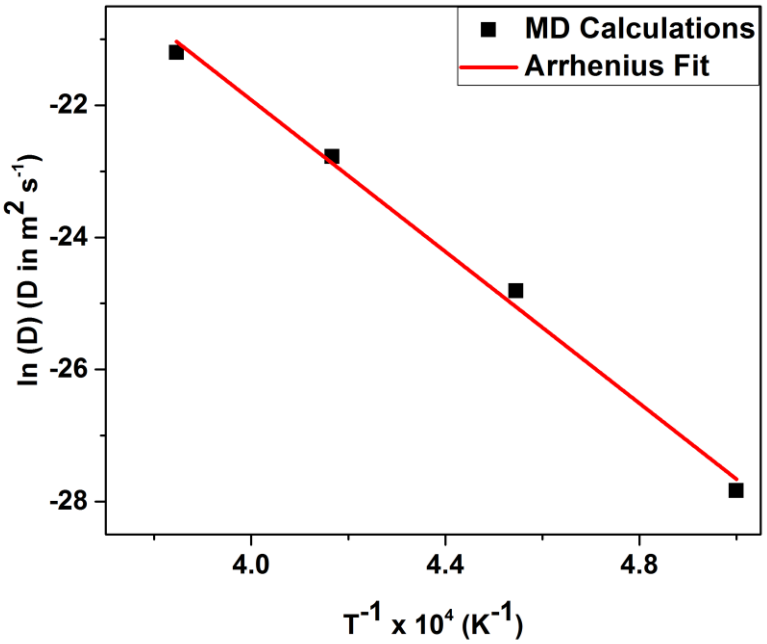

Figure 5.9: The Arrhenius plot for oxygen diffusion in CeO_2 lattice

The linear equation, with R^2 equal to 0.99, obtained from the plot is equated to Equation (5.9) where the $\frac{E_A}{R}$ is the slope of the plot and InD_o is the intercept. The activation energy E_A and the pre-factor D_o is estimated to be 4.9477 eV and 2.8554 m^2 s^{-1} respectively. Also, the condition of the Cerium atoms is examined as O atoms diffuse. Diffusion calculation is performed for Ce using the same method as earlier described for oxygen atoms diffusion. The unprocessed MSD data are

presented in Figure 5.10 to clearly see the movement of the Ce atoms in the presence of oxygen diffusion.

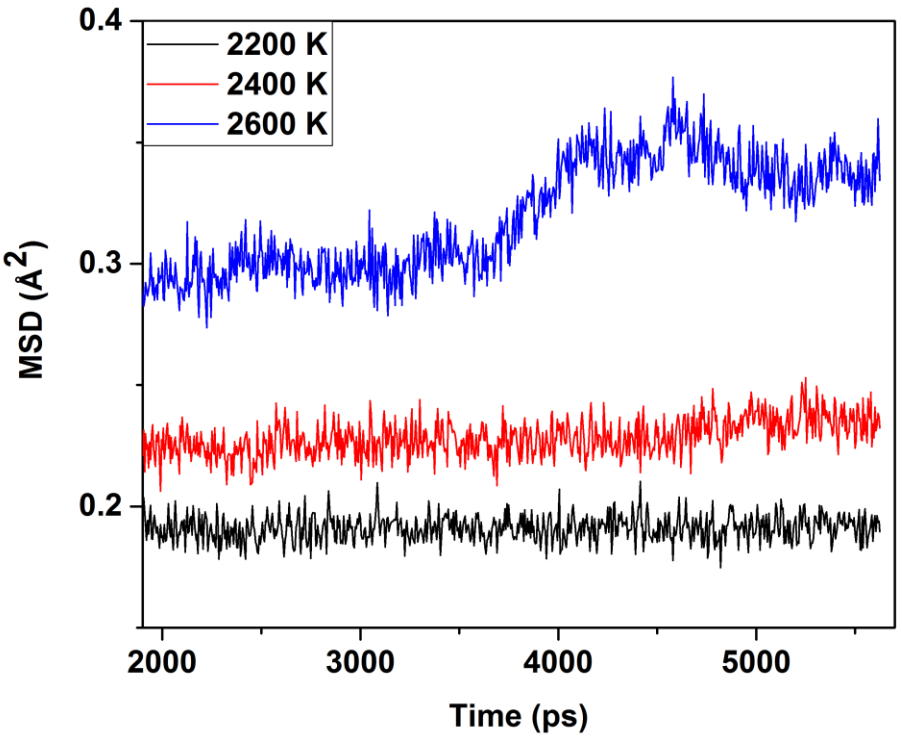

Figure 5.10: The LAMMPS calculated Mean-Squared Displacement (MSD) of cerium in CeO_2 lattice for a temperature range of 2200 – 2600 K

The cerium atoms show no sign of diffusing at 2200 K and 2400 K as presented in Figure 5.10. However, at 2600 K the Ce atoms experienced a sudden jump in the middle of the simulation time and then continue to follow its formal straight horizontal trend. The sudden Ce atoms jump is expected as the CeO_2 lattice is at extremely high temperature (2600 K) and O atoms already gained enough energy to break bonds from the Ce atoms. This study explains what happens in the UO_2 lattice at an extremely high temperature in the nuclear reactor during a nuclear accident as the fuel prepares to melt nuclear reactor core.

5.4 Summary

The structural and thermal properties of CeO_2 have been extensively studied using computational methods. The lattice parameters have been predicted using LAMMPS molecular dynamics code and the calculated parameters are in good agreement with the available data. The thermal expansion and conductivity of defect free CeO_2 lattice have been calculated. Comparisons were made between two different potentials; the EAM many body potentials and Buckingham two body potential. The calculated thermal properties of defect free CeO_2 lattice were also in agreement with the available theoretical and experimental data. The degrading effect of porosity and fission gases (Xe and Kr) on the thermal conductivity of CeO_2 has been investigated using molecular dynamics. The correlation between these factors (temperature, porosity, and fission gases) and thermal conductivity have been critically discussed in this study. This study revealed that thermal conductivity is an important property of UO_2 nuclear fuel (using CeO_2 as a surrogate material). A lot of activities happening in the nuclear reactor during operation as a result of fission process degrade thermal conductivity and limit performance. Also, the degraded thermal conductivity limits the ability of the fuel to dissipate heat faster and as such cannot withstand the loss of coolant for a longer period of time during a nuclear reactor accident. The diffusion of oxygen atoms in the CeO_2 lattice was also investigated and the results obtained revealed that oxygen atoms diffusion begin at temperature around 2000 K. During nuclear accident such as loss of coolant at Fukushima nuclear power plant where the condition of the fuel becomes extremely hot, the oxygen atoms in the fuel lattice break bond and roam about as the fuel prepares to melt and damage the reactor core. To overcome these challenges and prevent such accident as Fukushima from reoccurring, the thermal conductivity of the fuel must be improved. Improving the thermal conductivity of nuclear fuel will, in turn, improve its performance during nuclear reactor operation. It will also help the fuel to dissipate heat and recover faster during a loss of coolant accident. Additionally, an improved thermal conductivity will increase the lifespan of the nuclear fuel.

CHAPTER 6

EFFECT OF DISSOLVED ZrO_2 ON THE MICROSTRUCTURE AND THERMAL CONDUCTIVITY OF CeO_2

6.1 Brief introduction

During fission processes, dissolved fission products are generated in the nuclear fuel and the presence of these products do not only alter the physical property of the fuel but also its chemistry. Fission product like ZrO_2 dissolve in the fuel matrix to form a solid solution and as such changes the fuel composition and performance. The evolution of dissolved ZrO_2 in the fuel matrix during reactor operation results in complex microstructural changes and thus fuel restructuring is imminent. The microstructural evolution of the fuel depends on the dissolved additive and thus the fuel performance is different for different dissolved additive. To better understand the effect of dissolved ZrO_2 on the performance of the UO_2 nuclear fuel, 25% of ZrO_2 is added to CeO_2 to form a solid solution which mimics the condition of the UO_2 fuel in the nuclear reactor. The effect of the 25% dissolved ZrO_2 on the microstructure of CeO_2 is studied by characterizing the CeO_2 + 25% ZrO_2 pellet samples using the experimental procedure. Also, the thermal conductivity of the CeO_2 + 25% ZrO_2 sample is studied using both experimental and computational model. The methodology employed in this investigation is discussed in section 6.2. The results of this investigation, including discussion, are presented in section 6.3 while section 6.4 is the summary of this investigation.

6.2 Methodology

The CeO_2 + 25% ZrO_2 sample was made and sintered at Queens University, Kingston using the SPS technique. The sample was sintered at a 1460 ^oC temperature to form a perfect pellet sample. The density of the sample was measured using the Archimedean immersion technique and compared with calculated density from the GULP MD study. The theoretical density was calculated to be 97%, and the sample is considered to have about 3% porosity in it. Before performing microstructural analysis of the sample, the compound composition of the sample was first studied to reveal the ultimate quality diffraction data of the pellet sample using a Bruker D8 Discover X-ray diffractometer (XRD) analysis. The importance of the XRD data is to unfold the structure and the lattice parameter of the new system formed by adding ZrO_2 to CeO_2. The CeO_2

and Ce_3ZrO_8 samples were finely polished to about 1 µm with a polishing solution to achieve a clearly smooth surface for microstructural analysis. The Ce_3ZrO_8 pallet sample had a completely perfect surface for the analysis due to its compactness but there were several problems trying to polish the CeO_2 pellet sample. The CeO_2 seems to be too brittle because of its high porosity. The thermal conductivity of Ce_3ZrO_8 solid solution pellet sample was measured using the Direct Laser Flash (DLF) methods as implemented in the discovery laser flash thermal conductivity machine. The 1.27 cm x 1.27 cm with varying thickness cube sized pellet samples were prepared for thermal conductivity measurements by applying a graphite spray to the surfaces of the sample and leaving the sample to dry before measuring the thermal conductivity.

6.3 Results and Discussion

To investigate the effect of 25% dissolved ZrO_2 on the microstructure and thermal conductivity of CeO_2, the density of the CeO_2 + 25% ZrO_2 pellet samples sample was measured, to begin with. The measured density is compared to the calculated density from the GULP MD study. The measured density is 6.776 g/cm^3 and the MD calculated density is 6.949 g/cm^3 with an optimized lattice constant of 5.347 Å for an FCC cubic structure as predicted by GULP code. A study by Akio *et al.* [94] revealed that two compounds exist in the system of ZrO_2-CeO_2 which are known to be solid solutions of $Ce_2Zr_3O_{10}$ (tetragonal) and $Ce_{0.75}Zr_{0.25}O_2$ (Ce_3ZrO_8, Cubic). Crystalline Ce_3ZrO_8 solid solutions are formed in as prepared powders between 30-75 mol % CeO_2, but specifically, $Ce_{0.75}Zr_{0.25}O_2$ (Ce_3ZrO_8, Cubic) is formed with 75 mol % of CeO_2 and 25 mol % ZrO_2. The XRD diffraction peaks obtained in this work from the CeO_2 + 25% ZrO_2 pellet sample was analyzed using the Xpert HighScore XRD post-processing software. The XRD characterization of the sample was performed and it was observed that the XRD pattern obtained from the CeO_2 + 25% ZrO_2 pellet sample is consistent with the pattern of a well-crystallized Ce_3ZrO_8 when compared to the Ce_3ZrO_8 reference pattern in the Powder Diffraction File (PDF) database. The PDF crystallographic database is the only analysis system comprised of crystallographic and diffraction data that is designed for material identification and characterization. Table 6.1 presents the comparison between the measured diffraction peaks and the reference peaks from the PDF database for the Ce_3ZrO_8 sample. The reference crystallographic pattern in the PDF database that matches the Ce_3ZrO_8 pellet sample produced the PDF index name of the pellet sample to be Cerium Zirconium Oxide ($Ce_{0.75}Zr_{0.25}$ O_2) with a conventional unit cell of 12 atoms (Ce_3ZrO_8).

Table 6.1: Comparison of the PDF reference pattern with measured diffraction peaks of the Ce_3ZrO_8 sample. The interplanar spacing (d) is in Å, the position (2θ) is in deg, the relative intensity (I) is measured in percentages (%) and the (h k l) are the Miller indices of the crystallographic planes

				Reference Pattern			Sample Pattern		
No.	h	k	l	d [A]	2θ[deg]	I [%]	d [Å]	2θ [deg]	I [%]
1	1	1	1	3.09	43.49	100.00	3.08	43.64	86.19
2	2	0	0	2.68	50.68	35.00	2.67	50.88	35.71
3	2	2	0	1.89	74.47	60.00	1.89	74.58	72.27
4	3	1	1	1.61	90.36	50.00	1.61	90.64	100.00
5	2	2	2	1.54	95.72	12.00	1.54	95.79	24.40

The crystal system of the sample is predicted to the cubic structure with a space group Fm-3m (225), the lattice constant 5.349 Å and density of 6.940 g/cm^3. As previously reported by Akio *et al*. [94], the XRD measurement confirmed that the pellet sample of CeO_2 + 25% ZrO_2 is a solid solution of Cerium Zirconium Oxide $Ce_{0.75}Zr_{0.25}O_2$ (Ce_3ZrO_8, Cubic). Additionally, the lattice constant 5.347 Å earlier calculated using GULP code is also in good agreement with the value obtained from the XRD measurement. Also, the measured density of the sample using Archimedean immersion technique and GULP code reported earlier have an excellent agreement with density obtained from the XRD measurement. This XRD analysis was carried out to ascertain that the 25% ZrO_2 dissolved in the CeO_2 matrix to form a solid solution of Ce_3ZrO_8, which mimics the interaction of the UO_2 with the dissolved fission product in the nuclear reactor during reactor operation as one of the conditions that affect the nuclear fuel performance.

To further characterize the Ce_3ZrO_8 sample, the XRD diffraction data for pure CeO_2 samples had to be obtained to establish the effect of the dissolved ZrO_2 in the CeO_2 matrix. The graphical representation of the XRD diffraction data of Ce_3ZrO_8 and CeO_2 samples are presented in Figure 6.1 (a) and (b). The XRD peaks are labeled with their corresponding crystallographic plane. It is certain that as this fission product dissolves in the fuel matrix a number of structural adjustment will occur within the fuel as the chemical composition of the fuel is already changed.

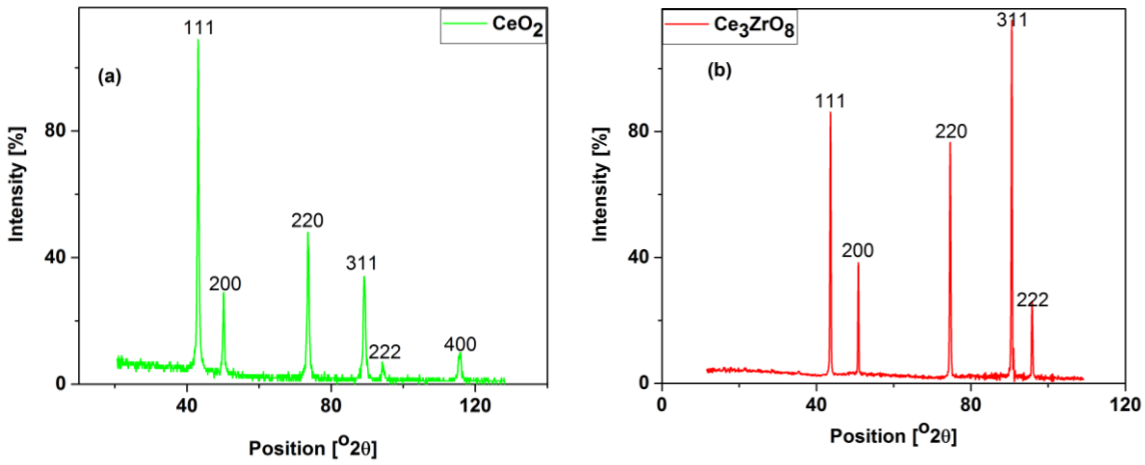

Figure 6.1: The measured XRD diffraction pattern of (a) pure CeO_2 sample (b) Ce_3ZrO_8 sample

This latter part of the XRD analysis described the trend which the fuel restructuring follows as the orientation of the Ce_3ZrO_8 pellet sample is compared with that of a pure CeO_2 sample. It has been established that the crystal system, FCC cubic with space group Fm-3M, of the newly formed Ce_3ZrO_8 solid solution remain the same as that of a pure CeO_2 sample even after a certain amount of ZrO_2 additive had dissolved in the CeO_2 matrix, but the same cannot be said about the structural parameter like lattice constant. The lattice constant, 5.349 Å, of the newly formed Ce_3ZrO_8 solid solution is different when compared with the lattice constant of CeO_2 of 5.410 Å as earlier reported.

The change in lattice parameter of the two materials can be well explained by the comparison of the diffraction data. Figure 6.2 gives a vivid information as to what happened to the CeO_2 lattice as 25% ZrO_2 additive dissolved in it. The diffraction peaks are labeled with their corresponding planes and the intensity of the peaks are different for the two materials. Most of the diffraction peaks in the Ce_3ZrO_8 sample, except for the (111) plane, have higher intensities than that of the CeO_2 samples. The significance of this higher intensity in Ce_3ZrO_8 sample is that the planes with the higher intensity are predominant in the sample. The CeO_2 samples are predominantly (111) plane-orientated material but with the addition of the ZrO_2 additive, the (311) plane becomes predominant in the resulting Ce_3ZrO_8 material.

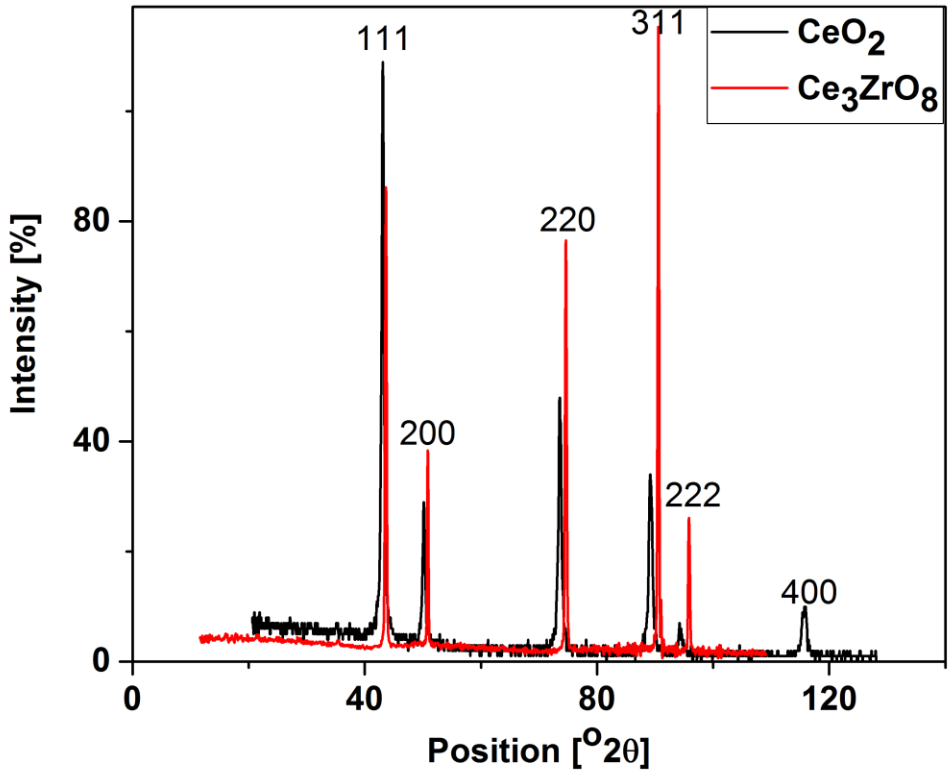

Figure 6.2: The comparison of the measured XRD diffraction pattern of CeO_2 and Ce_3ZrO_8 sample

Also, the peaks in the Ce_3ZrO_8 sample experience a shift to the right when compared to the peaks in the CeO_2 sample. The observed shift is consistent with Ce_3ZrO_8 sample contraction which in turn accounts for the change in lattice parameter as earlier noticed. This contraction in the Ce_3ZrO_8 sample is said to occur because of a smaller mass Zr atom displacing a larger mass Ce atom in the conventional unit cell of Ce_3ZrO_8. The lattice is expected to contract to eliminate the space created from this displacement and form a compact material. The XRD diffraction data have revealed a significant of the ZrO_2 additive on the structure and lattice of CeO_2 as it forms a solid solution of Ce_3ZrO_8. However, to properly examine the effect of the dissolved ZrO_2 additive on the microstructure of the CeO_2 the samples must be further characterized using EBSD.

First, the EDS information of the Ce_3ZrO_8 sample was obtained to confirm the phase present in the sample. Since the Ce_3ZrO_8 sample composes of two different similar structure of ZrO_2 and CeO_2, it is reasonable to assume that are two different phases present in the sample. The EDS image of

the Ce_3ZrO_8 sample was obtained to see the number of phases present and how they are distributed in the sample. It would be interesting to know how the dissolved ZrO_2 additive is distributed in the Ce_3ZrO_8 system as the solid solution is formed.

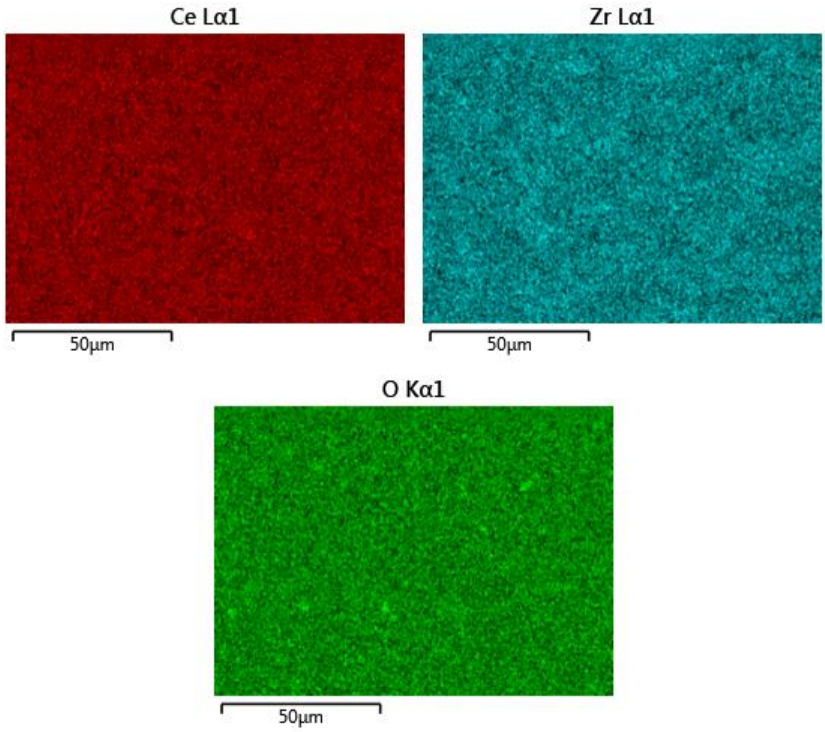

Figure 6.3: The EDS image of Ce_3ZrO_8 pallet sample obtained from the microstructural measurements

Figure 6.3 presents the concentration of each element in the Ce_3ZrO_8 system; each color represents each element and how they are distributed in the Ce_3ZrO_8 sample. The EDS information shows that all the elements in the sample are evenly distributed throughout the sample. The rectangular box represents the surface of the sample and each color represents each element and the position which they occupy in the sample. The information provided in Figure 6.3 implies that there is a homogenous phase present in the Ce_3ZrO_8 sample since Zr content is not found segregating at one corner of the sample. This result is further supported by the XRD diffraction analysis which earlier reported that as the ZrO_2 additive dissolved in the CeO_2 matrix to form Ce_3ZrO_8 solid solution the crystal system (FCC cubic) of the sample remains unchanged. Additionally, the EDS information further stressed that there is a chemical reaction between CeO_2 and ZrO_2 additive to form Ce_3ZrO_8 solid solution which has its own ideal structure and phase. It is easy to conclude from the EDS

image that the sample has a homogeneous microstructure with just one phase of Ce_3ZrO_8 and as such, it is impossible to observe ZrO_2 phase distribution separately in the sample.

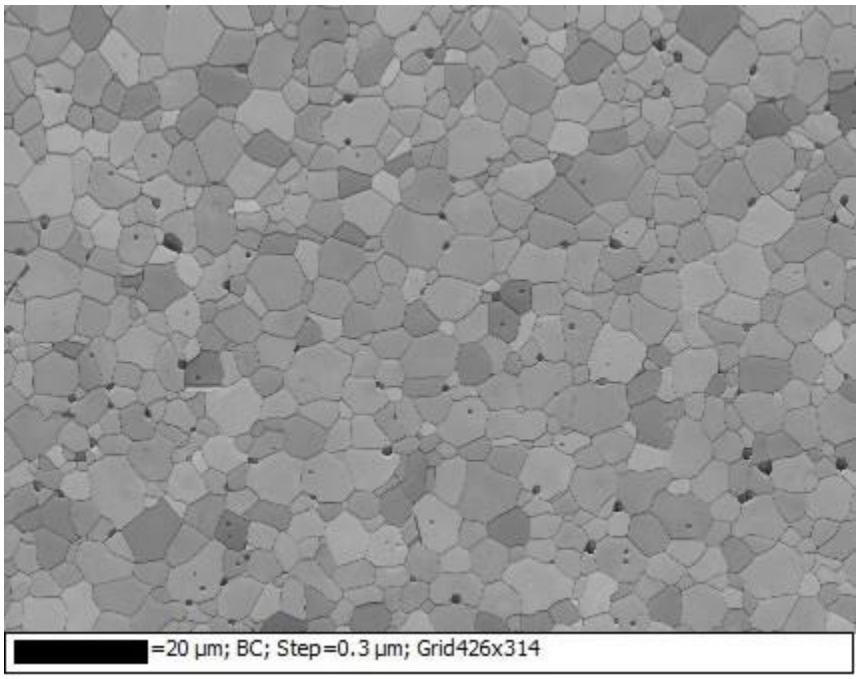

Figure 6.4: Grains alignment in Ce_3ZrO_8 pellet sample obtained from the EBSD scans

EBSD information of the of Ce_3ZrO_8 sample was obtained in order to probe the grain size and boundary distribution. It is important to understand the effect ZrO_2 additive on the grain size and boundary distribution of CeO_2. Grains are part of the major component of a material that determine the mechanical and thermal properties (Figure 6.4). It is certain that if the grains of the sample are affected by the additive, the thermal properties of the sample are expected to change. The degradation of the thermal property of the CeO_2 sample by the ZrO_2 additive can be equally attributed to the changes in the Ce_3ZrO_8 microstructure and one of those changes is the grain size distribution. The EBSD image for gain alignment in the Ce_3ZrO_8 sample is presented in Figure 6.4.

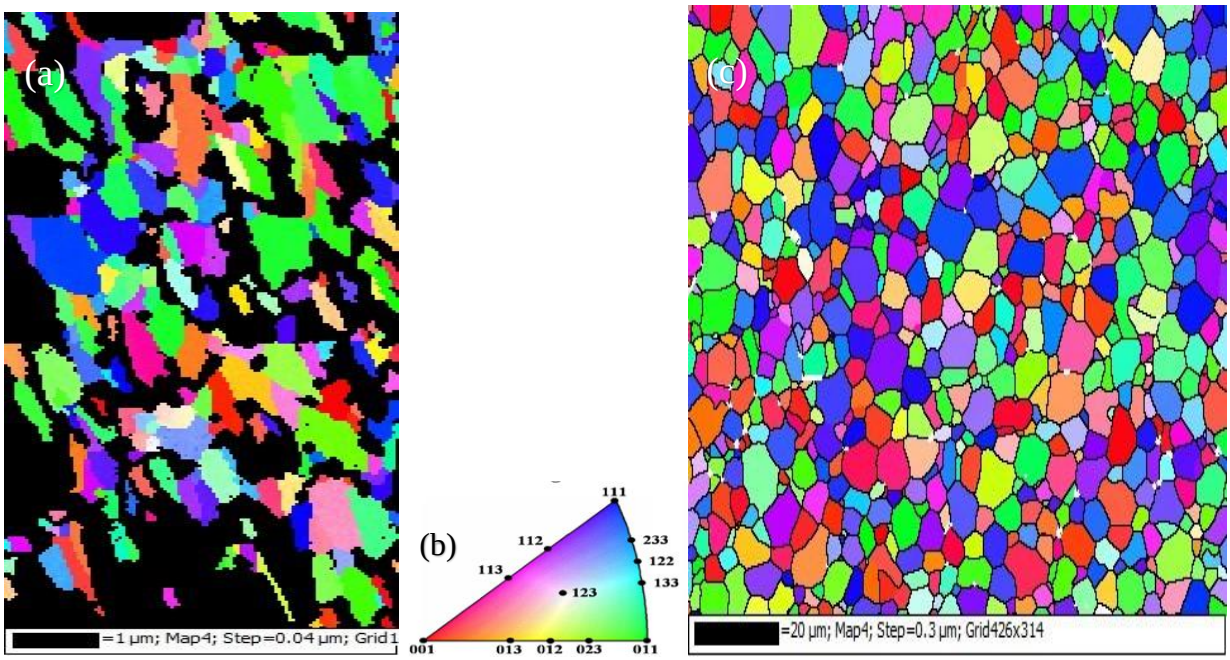

Figure 6.5: (a) EBSD Inverse Pole Figure (IPF) map of CeO_2 pellet sample (b) IPF coloring scheme and (c) IPF map of Ce_3ZrO_8 pellet sample

Figure 6.5 (a) and (c) shows the EBSD mapping of both CeO_2 and Ce_3ZrO_8 pellet samples. The Inverse Pole Figure (IPF) images in Figure 6.5 (a) and (c) show the orientation of the CeO_2 and Ce_3ZrO_8 pellet samples. Each grain color in the map corresponds to a specific crystallographic plane as illustrated by the IPF coloring scheme in Figure 6.5 (b). These images give a vivid information about how the grains in the Ce_3ZrO_8 pellet sample are changing when compared to results from CeO_2 microstructural studies. The IPF image of Ce_3ZrO_8 pellet sample was taken at a 20 µm distance while the CeO_2 sample image was shot at about 1 µm distance, as stated on the two images. The distance at which these images are taken suggests that the sizes of grains in each sample are different. The CeO_2 pellet sample used in this study was sintered at 1100^oC temperature and has a theoretical density of 94% (6% porosity). The effect of ZrO_2 additive on the grain size of CeO_2 microstructure in Ce_3ZrO_8 solid solution is then calculated from the IPF data using an EBSD post-processing software.

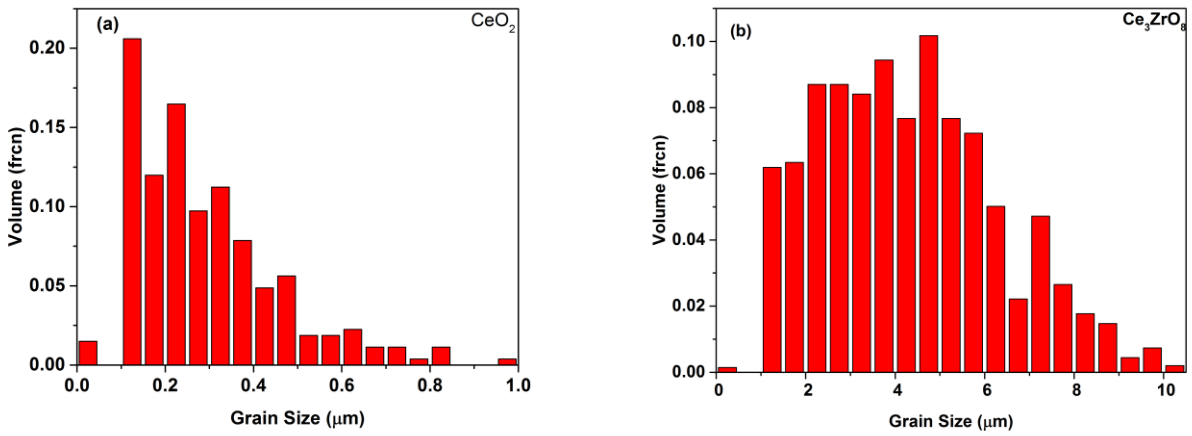

Figure 6.6: Grain size distribution of (a) CeO_2 (b) Ce_3ZrO_8 pellet sample. The grain volume is expressed in fraction (frcn) and the grain size in micro meters (μm)

The evaluated grain size distribution in the two samples are presented in Figure 6.6 (a) and (b). The results from the CeO_2 and Ce_3ZrO_8 pellet sample cannot be directly compared because of their different sintering conditions and porosity. The CeO_2 pellet sample was sintered at an 1100^{o}C temperature and has 6% porosity while the Ce_3ZrO_8 pellet sample was sintered at a 1460^{o}C temperature and has 3% porosity. Previous studies [95–98] have reported that temperature and porosity affect grain growth in sintered CeO_2 pellet sample. Grain size is reported to be bigger in samples that are sintered at a higher temperature than those that are sintered at a lower temperature. Additionally, samples with higher porosity are expected to possess smaller grain sizes compared to the pellet samples with lower porosity. An increase in porosity has been known to decrease grain size and increase grain boundaries in pellet samples. The EBSD result from the Ce_3ZrO_8 pellet sample must be compared with the CeO_2 sample with similar sintering condition to better understand the effect of the dissolved ZrO_2 additive on the grain size of CeO_2. But the synthesis of pure CeO_2 using Spark Plasma Sintering (SPS) has been extremely challenging due to the reduction of Cerium (IV) oxide into Cerium (III) oxide (Ce_3O_4), high porosity in the resulting pellet sample and stability. Zhang *et al.* [99] reported that a CeO_2 sample with about 1461^{o}c sintering temperature has about 1% porosity and average grain size of 8.52 μm which implies that the CeO_2 sample is a material with grain in few micrometers. The grains size distribution curve in Figure 6.6 (b), obtained from the EBSD data, shows that the Ce_3ZrO_8 pellet sample has an average grain size of 5.25 μm. The grain size in Ce_3ZrO_8 pellet sample is reduced because of dissolved

ZrO_2 additive in the CeO_2 matrix, when compared to 8.52 µm grain size reported by Zhang *et al.* [99] for CeO_2. This change in the microstructure of Ce_3ZrO_8 pellet sample is also expected to affect the thermal property of the material in comparison to CeO_2. As earlier reported, the thermal conductivity of non-metallic materials depends on phonon mean free path, that is, the distance traveled by scattered phonons before hitting an obstruction which causes further scattering. In materials with large grains, the number of grain boundaries is less and phonon travels a long distance before hitting a grain boundary, the frequency of phonon scattering is less and heat conduction is high compared to materials with small grains. Materials with smaller grain sizes have more grain boundaries and phonon are scattered after traveling short distance which degrades thermal conductivity because of the high frequency of phonon scattering. The dissolved ZrO_2 additive has caused grain size reduction in the resulting Ce_3ZrO_8 solid solution pellet sample and this grain size effect is expected to degrade the thermal conductivity of the Ce_3ZrO_8 solid solution pellet sample when compared to the thermal conductivity CeO_2. This study explains the microstructural fuel restructuring process that happens to UO_2 nuclear fuel in the nuclear reactor as fission product like ZrO_2 dissolves in the fuel matrix to form a solid solution. Figure 6.6 (a) presents the grain size distribution of the CeO_2 pellet sample and the average grain size of the sample is about 0.4 µm. The CeO_2 pellet sample has small gain size because it was sintered at a lower temperature which provides adequate knowledge to how temperature affects grain size in non-metallic materials.

Since the Ce_3ZrO_8 pellet sample retains 3% porosity in it and as such cannot be considered as a fully dense sample with no defect, a computational simulation was carried out to predict the thermal conductivity of a Ce_3ZrO_8 with no defect. A Ce atom is replaced by Zr atom in the conventional unit cell of CeO_2 involving 12 atoms to account for the dissolved ZrO_2 additive in the CeO_2 matrix. The thermal conductivity calculation was carried out using a Buckingham pairwise potential. A system consisting of 8 x 8 x 8 conventional unit cell involving 6144 atoms, as presented in Figure 6.7, was considered for performing the LAMMPS MD simulations.

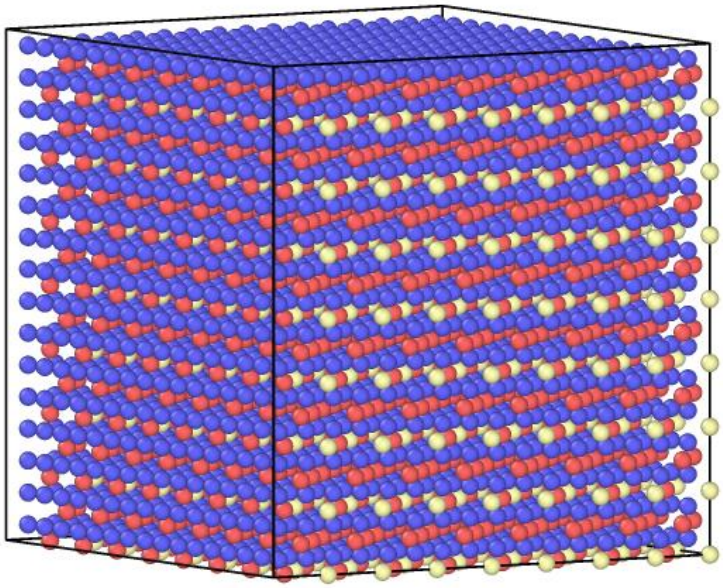

Figure 6.7: The crystal structure of 8 x 8 x 8 Ce_3ZrO_8 system where the purple, red and yellow spheres are the Ce, O and Zr atoms, respectively

The system was heated between 300 K and 1000 K temperature at 100 K intervals to calculate the thermal conductivity. The system was first simulated in the NPT ensemble for 2000 ps before switching to a constant volume and temperature NVT ensemble and ran for another 2000 ps. The HCACFs were computed along with an NVE ensemble calculation which generates a 10000 ps raw heat current data at every calculation. The results of the experimentally measured and LAMMPS calculated thermal conductivity of Ce_3ZrO_8 system are compared in Figure 6.8. The thermal conductivity of Ce_3ZrO_8 system is significantly degraded at low temperature compared to CeO_2 but the degrading effect begins to vanish as the temperature increases. At 300 K, 500 K, and 1000 K temperatures, with the inclusion of dissolved ZrO_2 fission product, the thermal conductivity of CeO_2 is degraded by 48%, 41%, and 12% respectively. The degrading effect is reduced at high temperature because the thermal conductivity of CeO_2 decreases drastically as temperature increases but the thermal conductivity of Ce_3ZrO_8 system respond significantly different to temperature. The thermal conductivity of Ce_3ZrO_8 system has a slight decreasing response to temperature and as such it is not heavily affected by temperature. Additionally, the thermal conductivity of Ce_3ZrO_8 system became almost constant at temperatures beyond 750 K. From this comparison, the dissolved ZrO_2 fission product seems to have the least degrading effect

on the thermal conductivity of CeO_2 when compared to statistics from the other fission process caused defect earlier discussed, considering the fact that the Ce_3ZrO_8 system has 25% ZrO_2 and 75% CeO_2 composition.

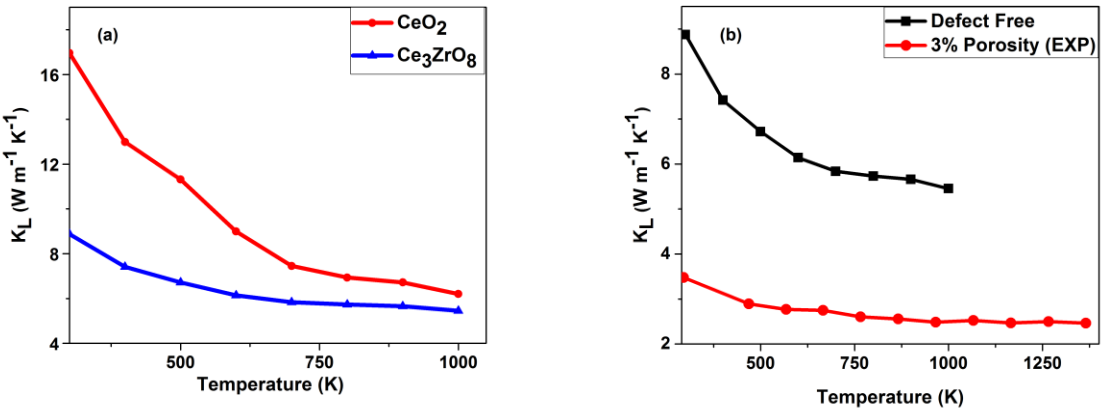

Figure 6.8: (a) The LAMMPS calculated thermal conductivity of defect free Ce_3ZrO_8 system in comparison with CeO_2 (b) The LAMMPS calculated thermal conductivity of defect free Ce_3ZrO_8 system in comparison with the measured thermal conductivity Ce_3ZrO_8 pellet sample with 3% porosity

Figure 6.8 (b) presents the effect of porosity on the thermal conductivity of Ce_3ZrO_8 system where the calculated thermal conductivity of the defect free Ce_3ZrO_8 is compared to the experimentally measured thermal conductivity of 3% porous Ce_3ZrO_8 pellet sample. The result shows that unlike temperature, porosity has a powerful degrading effect on the thermal conductivity of Ce_3ZrO_8. With just 3% porosity in the Ce_3ZrO_8 sample, the thermal conductivity is degraded by 61% and 55% at 300K and 1000 K temperatures, respectively. The experimentally measured thermal conductivity of Ce_3ZrO_8 pellet sample also exhibits the same behavior to increasing temperature as earlier experienced in the theoretically predicted thermal conductivity of defect free Ce_3ZrO_8 system.

6.4 Summary

The microstructural effect of dissolved ZrO_2 on CeO_2 has been experimentally investigated. The XRD analysis shows that a Ce_3ZrO_8 solid solution system is formed as ZrO_2 dissolve in the CeO_2 matrix. The change in lattice parameter of the Ce_3ZrO_8 when compared to CeO_2 is accounted for

by the crystallographic peak shift observed in the sample. The EDS result revealed that there is only one FCC phase observed in the Ce_3ZrO_8 solid solution system in contrast to the two different phases of ZrO_2 and CeO_2 expected. The grains size distribution of the Ce_3ZrO_8 solid solution sample revealed the presence of dissolved ZrO_2 in CeO_2 matrix as grains are smaller in Ce_3ZrO_8 solid solution sample compared to CeO_2 sample. The degrading effect of dissolved ZrO_2 on the thermal conductivity of CeO_2 was also investigated in Ce_3ZrO_8 using molecular dynamics study and experimental measurements. The thermal conductivity of Ce_3ZrO_8 is degraded compared to CeO_2 and the observed degradation is accounted for by the presence of ZrO_2. However, the measured thermal conductivity of the 3% porous Ce_3ZrO_8 sample in comparison with that of the calculated defect free sample shows a further conductivity degradation.

CHAPTER 7

SUMMARY, CONCLUSION AND FUTURE WORK

7.1 Summary and Conclusion

The thermal conductivity of nuclear fuel is an important property that determines the performance of the fuel. It has been identified as a significant attribute of the nuclear fuel which can be tailored to stop loss of coolant accident such as Fukushima from reoccurring in the future. However, thermal conductivity is degraded by a lot of processes that occur in the nuclear reactor during operation. Porosity and fission products have been considered as a major cause of such degradation in nuclear fuel.

Thermal conductivity and its degradation in nuclear fuels have been investigated using both analytical and atomistic modeling techniques. The thermal conductivity of pure UO_2, ThO_2, and CeO_2 was calculated using semi-empirical/correlation equations and it is observed that thermal properties of pure UO_2, ThO_2, and CeO_2 decrease as temperature increases. The semi-empirical/correlation equations were modified to account for the effect of porosity on the three materials. The thermal conductivity of UO_2, ThO_2, and CeO_2 with increasing porosity is also calculated using correlation equations and it is observed that thermal conductivity does not only degrade with increasing temperature but also with increasing porosity. The semi-empirical/correlation equations confirmed that thermal conductivity depends strongly on porosity in the fuels.

Thermal conductivity and its degradation in UO_2 nuclear fuel, using CeO_2 as a representative of UO_2 nuclear fuel, is critically investigated using atomistic modeling method. Effect of porosity, Xenon (Xe) fission gas, krypton (Kr) fission gas and ZrO_2 dissolved fission product on the thermal conductivity of CeO_2 is investigated using MD approach as implemented in LAMMPS. Lattice parameters minimization, thermal expansion, and thermal conductivity as a function of temperature calculations were performed to test two different potentials; many-body EAM and two body Buckingham potentials. The increasing lattice parameters with increasing temperature that is observed in CeO_2 using the many-body EAM potential agrees well with experimental data. Also, the values of decreasing thermal conductivity with increasing temperature predicted by the

EAM potentials excellently agree with experimental data, unlike, the overestimated values obtained using the two body Buckingham potentials. The many-body EAM potential is established as the best potentials for this research and it is used for other calculations involving thermal properties of CeO_2.

Porosity is induced into the CeO_2 lattice in percentages, up to 5% porosity, by strategically removing an appropriate number of atoms to mimic the porosity evolution in the nuclear fuel. The thermal conductivity of the porous CeO_2 structure is calculated using the equilibrium classical MD techniques together with the Green-Kubo linear response formalism. Also, the thermal conductivities of heavily porous CeO_2 pellet, up to 48.80% porosity, samples were experimentally measured. The results of the experimentally measured and theoretically predicted thermal conductivity of CeO_2 clearly ascertain that thermal conductivity is densely degraded as porosity increases in the CeO_2 lattice. The effect of Xe and Kr fission gases on the thermal conductivity of CeO_2 is calculated and compared to the thermal conductivity of a defect free CeO_2 lattice. The Xe and Kr gases were carefully placed into the pores created in the CeO_2 lattice to clearly mimic the collection of fission gases in the lattice of nuclear fuel during reactor operation. It turns out that 5% Xe results in more decrease in thermal conductivity compared to 5% Kr in the CeO_2 matrix at 300 K and vice versa at 1100 K.

The effect of dissolved ZrO_2 fission product on the microstructure and thermal properties of CeO_2 is also investigated. A Ce_3ZrO_8 solid solution pellet sample consisting of 25% ZrO_2 and 75% CeO_2 is sintered to mimic the condition of the nuclear fuel as ZrO_2 dissolve in the fuel matrix to form a solid solution. The pellet sample is characterized using the XRD equipment to obtain the crystallographic diffraction patterns. The obtained diffraction peaks were matched with the reference patterns in the Powder Diffraction File (PDF) database to ascertain the nature of the pellet sample. The CeO_2 sample diffraction peaks were also obtained and compared to the Ce_3ZrO_8 diffraction pattern to establish the effect of the dissolved ZrO_2 fission product in the CeO_2 matrix. The orientation of the sample changes with the addition of dissolved ZrO_2 from predominantly (111) plane in CeO_2 to (311) plane in Ce_3ZrO_8 solid solution. Also, the Ce_3ZrO_8 lattice experienced a contraction, as revealed by the XRD result, when its lattice parameter is compared to CeO_2. The contraction observed in the Ce_3ZrO_8 sample occurred because of the difference in the atomic radius of Ce (248 pm) in comparison with Zr (230 pm). The microstructure of the Ce_3ZrO_8 sample is

studied using EBSD technique to better understand the microstructural evolution as a function of dissolved ZrO_2 fission product. In the presence of ZrO_2, the grain sizes of the Ce_3ZrO_8 sample becomes smaller when compared to the grain sizes in pure CeO_2. Grain sizes in nonmetallic materials affect thermal conductivity because they control the scattering frequency in the material. Materials with smaller grain sizes are known to have lower thermal conductivity. The thermal conductivity of the Ce_3ZrO_8 sample is experimentally and theoretically measured. The theoretically measured thermal conductivity of the Ce_3ZrO_8 system is compared to the thermal conductivity of a pure CeO_2 system and it is observed that thermal conductivity is reduced as 25% ZrO_2 dissolved in the CeO_2 matrix to form Ce_3ZrO_8 solid solution as earlier predicted by the grain size study. Additionally, the experimentally measured thermal conductivity of 3% porous Ce_3ZrO_8 solid solution pellet sample is further reduced when compared to the theoretically measured thermal conductivity of the pure Ce_3ZrO_8 system. Hence, the thermal conductivity of CeO_2 is continuously degraded by increasing presence of products from burnup due to radiation conditions. In terms of radiation effect, porosity results in more decrease in the thermal conductivity when compared to Kr, Xe gas in the range of 1-5% and ZrO_2 in CeO_2 matrix.

Diffusion of oxygen in CeO_2 as a function of temperature is calculated using the EAM many-body potentials. The diffusion of oxygen increases with increase in temperature from 400 K to 2600 K temperature. The oxygen diffusion coefficients are plotted against the inverse temperature in an Arrhenius plot to see the diffusion dependence of the parameters and calculate the activation energy. The results of this investigation clearly revealed that O atoms are more mobile in the CeO_2 lattice when compared to Ce atoms. The Ce atoms can barely move from their respective positions due to their atomic sizes. The diffusion calculation gives a vivid understanding as to what happens in the fuel lattice at a higher temperature, that is, the O atoms break bonds with the U atoms at high temperature.

7.2 Future work

Thermal conductivity and its degradation by fission products have been critically investigated. This research has described the effect of radiation conditions like porosity, fission gases and dissolved fission product on the thermal conductivity of nuclear fuel. However, a lot of other conditions affect the thermal conductivity of nuclear fuel in the nuclear reactor. Effect of fission products like metallic precipitate and oxide precipitate on thermal conductivity has not been

studied. It will be interesting to know how nuclear fuel behavior are altered when these fission products are produced. The future work of this research can be extended to studying the effect of metallic precipitate and oxide precipitate fission products on the thermal conductivity of nuclear fuel. These fission products change the structural, physical and the thermal properties of the fuel as they modify the fuel to occupy a certain percentage of the fuel matrix.

Oxygen diffusion occurs in the perfect fuel lattice at a high temperature close to the melting temperature. However, the diffusion properties of the fuel lattice with defect inclusion has not be studied. Future work can investigate how a defect in nuclear fuel affects the diffusion behavior of the fuel. The diffusion of oxygen atoms in the presence of fission product can be studied. Also, the diffusion of fission gases in the nuclear fuel lattice can be investigated.

REFERENCES

[1] Ian Hore-Lacy, Nuclear Energy in the 21st Century, 3rd editio, World Nuclear University Press, 2012.

[2] P.D. Wilson, The nuclear fuel cycle, from ore to waste. Oxford University press, Oxford University Press inc, New York, 1996.

[3] W. Peiman, I.L. Pioro, K. Gabriel, M. Hosseiny, Thermal aspects of conventional and alternative fuels, in: I.L. Pioro (Ed.), Handb. Gener. {IV} Nucl. React., Woodhead Publishing, 2016: pp. 583–635.

[4] H. Khartabil, D. Brady, T. Schulenberg, Supercritical water-cooled reactor (SCWR) development through GIF collaboration, (2009) 1–9.

[5] M.W.D. Cooper, Atomic scale simulation of irradiated nuclear fuel, Imperial College London, 2015.

[6] A.P. Meshik, The Workings of an Ancient Nuclear Reactor, Sci. Am. 293 (2005) 56–63.

[7] G.F. Hewitt, J.G. Collier, Introduction to Nuclear Power, Taylor & Francis, 2000.

[8] M.A. Miller, Sketching, (1946).

[9] Nuclear Decomissioning Authority, Oxide Fuels, (2012) 1–21.

[10] Gen IV International Forum, Gas-Cooled Fast Reactor (GFR), (n.d.) 50044. https://www.gen-4.org/gif/jcms/c_9357/gfr.

[11] Gen IV International Forum, Very High Temperature Reactor (VHTR), (n.d.) 50044. https://www.gen-4.org/gif/jcms/c_9362/vhtr.

[12] Sodium-Cooled Fast Reactor (SFR), Gen IV Int. Florum. (2016) 50044. https://www.gen-4.org/gif/jcms/c_42152/sodium-cooled-fast-reactor-sfr.

[13] T. Fanning, Sodium as a Fast Reactor Coolant, Top. Semin. Ser. Sodium Fast React. US. (2007). http://www.nuclear.energy.gov/pdfFiles/SodiumCoolant_NRCpresentation.pdf.

[14] T. Universit, Lead-cooled fast reactor, (n.d.) 50044.

https://inlportal.inl.gov/portal/server.pt/community/nuclear_energy/277/lfr/2254.

[15] O.R.N. Laborartory, Historic_Molten_Salt_Reactor_Experiment_Brochure_ORNL_1965-1972.pdf, (1965).

[16] Nuclear Energy Research Advisory Committee and the Generation IV International Forum, A technology roadmap for generation IV nuclear energy systems, (2002).

[17] S. Williams, How Molten Salt Reactors Might Spell a Nuclear Energy Revolution, ZME Sci. (2016). http://www.zmescience.com/ecology/what-is-molten-salt-reactor-424343/.

[18] Ima Ituen, Comparing the Risk of the Pressure Tube-Scwr To the Candu Using Probabilistic Risk Assessment, McMaster Universsity, MSc Thesis (2012).

[19] T. Generation, I. V International, G.I.F. Charter, G. Iv, GIF Portal, (2016) 1–2.

[20] J. Mahaffey, Atomic Accidents: A History of Nuclear Meltdowns and Disasters: From the Ozark Mountains to Fukushima, Pegasus, 2014.

[21] A. Marks, Physics of Uranium and Nuclear Energy - World Nuclear Association, (2014) 1–9.

[22] H.L. Anderson, E.T. Booth, J.R. Dunning, E. Fermi, G.N. Glasoe, F.G. Slack, The fission of uranium [14], Phys. Rev. 55 (1939) 511–512.

[23] S.C. Middleburgh, Atomistic Scale Simulation of Materials for Future Nuclear Reactors, Imp. Coll. PhD Thesis (2012).

[24] A. Einstein, Ist die Trägheit eines Körpers von seinem Energieinhalt abhängig?, Ann. Phys. 323 (1905) 639–641.

[25] Nuclear Energy, Chalk River Nuclear Accident, Nucl. Energy. (2015) 1–2. http://nuclear-energy.net/nuclear-accidents/chalk-river.html.

[26] I. Gray, Mike and Rosen, The Warning ACCIDENT AT THREE MILE ISLAND: A NUCLEAR OMEN FOR THE AGE OF TERROR, W. W. Norton & Company, New York, 2003.

[27] D. Wordsworth, Atomic Accidents, 2999.

[28] S. Nenova, Nuclear Energy, Eur. Parliam. Brief. Notes. 7 (2012) 1–7. http://www.europarl.europa.eu/ftu/pdf/fr/FTU_4.13.5.pdf.

[29] J. Tokai, Fukushima Accident, (2014) 1–26. http://www.world-nuclear.org/info/safety-and-security/safety-of-plants/fukushima-accident/.

[30] D.Wojtaszek, Future Nuclear Power Generation in Canada: Transition to Thorium Fuelled SCWRs, in: International Conference on Modelling and Simulation in Nuclear Science and Engineering (7ICMSNSE), Ottawa, Ontario, Canada, 2015.

[31] B. Szpunar, L. Malakkal, E. Jossou, D. Oladimeji, J. Ranasinghe, I. Rossland, J.A.Szpunar, First Principle Studies of Thermal Conductivity of Nuclear Fuel Materials, in: 13th International Conference on CANDU Fuel, Kingston, Canada, 2016.

[32] S. Yeo, E. McKenna, R. Baney, G. Subhash, J. Tulenko, Enhanced thermal conductivity of uranium dioxide-silicon carbide composite fuel pellets prepared by Spark Plasma Sintering (SPS), J. Nucl. Mater. 433 (2013) 66–73.

[33] R.G. Cochran, N. Tsoulfanidis, The nuclear fuel cycle : analysis and management, La Grange Park, Ill., USA : American Nuclear Society, 1999. http://www.torontopubliclibrary.ca/detail.jsp?Entt=RDM1857475&R=1857475&print=true.

[34] P.G. Lucuta, H. Matzke, R.A. Verrall, Modelling of UO2-based SIMFUEL thermal conductivity, At. Energy Canada Limited, AECL. 3115 (1994) 1–17.

[35] V. V. Rondinella, T. Wiss, The high burn-up structure in nuclear fuel, Mater. Today. 13 (2010) 24–32.

[36] U.S.E.P.A. USEPA, Toxicological Review of Cerium Oxide and Cerium Compounds, (2009) 118. http://www.epa.gov/iris/toxreviews/1018tr.pdf.

[37] M. Mogensen, N.M. Sammes, G.A. Tompsett, Physical, chemical and electrochemical properties of pure and doped ceria, Solid State Ionics. 129 (2000) 63–94.

[38] S. Gangopadhyay, D.D. Frolov, A.E. Masunov, S. Seal, Structure and properties of cerium oxides in bulk and nanoparticulate forms, J. Alloys Compd. 584 (2014) 199–208.

[39] A.T. Nelson, D.R. Rittman, J.T. White, J.T. Dunwoody, M. Kato, K.J. Mcclellan, An Evaluation of the Thermophysical Properties of Stoichiometric CeO2 in Comparison to UO2 and PuO2, J. Am. Ceram. Soc. 97 (2014) .

[40] H.X. Song, L. Liu, H.Y. Geng, Q. Wu, First-principle study on structural and electronic properties of CeO2 and ThO2 under high pressures, Phys. Rev. B. 87 (2013) 184103.

[41] D. Haslam, M. Poise *et al.* Thermal conductivity, (2008). http://www.zircotec.com

[42] J. Bates, Thermal diffusivity of UO2, Ceram. Res. Dev. Q. Rep. (1965).

[43] R.L. Gibby, The effect of plutonium content on the thermal conductivity of (U, Pu)O2 solid solutions, J. Nucl. Mater. 38 (1971) 163–177.

[44] T.G. Godfrey, W. Fukerson, T.G. Kollie, J.P. Moore, D.L. McElroy, Thermal conductivity of uranium dioxide and ARMCO iron by an improved radial heat flow technique, 4500 (1964).

[45] J. Conway, A. Feith, An Interim Report on a Round Robin Experimental Program to Measure the Thermal Conductivity of Stoichiometric Uranium Dioxide, Gen. Electr. Rep. (1969).

[46] C. Ronchi, M. Sheindlin, M. Musella, G.J. Hyland, Thermal conductivity of uranium dioxide up to 2900 K from simultaneous measurement of the heat capacity and thermal diffusivity, J. Appl. Phys. 85 (1999) 776–789.

[47] J.W.L. Pang, W.J.L. Buyers, A. Chernatynskiy, M.D. Lumsden, B.C. Larson, S.R. Phillpot, Phonon lifetime investigation of anharmonicity and thermal conductivity of UO2 by neutron scattering and theory, Phys. Rev. Lett. 110 (2013) 1–5.

[48] B.T. Wang, J.J. Zheng, X. Qu, W.D. Li, P. Zhang, Thermal conductivity of UO2 and PuO2 from first-principles, J. Alloys and Compounds. 628 (2015) 261–271.

[49] H. Kim, M.H. Kim, M. Kaviany, Lattice thermal conductivity of UO2 using ab-initio and classical molecular dynamics, J. Appl. Phys. 115 (2014).

[50] M. Khafizov, I.W. Park, A. Chernatynskiy, L. He, J. Lin, J.J. Moore, D. Swank, T. Lillo, S.R. Phillpot, A. El-Azab, D.H. Hurley, Thermal conductivity in nanocrystalline ceria thin

films, J. Am. Ceram. Soc. 97 (2014) 562–569.

[51] Y. Lu, Y. Yang, P. Zhang, Thermodynamic properties and structural stability of thorium dioxide, J. Phys. Condens. Matter. 24 (2012) 225801.

[52] B. Szpunar, J. Szpunar, Thoria Ehancement of Nuclear Reactor Safety, Phys. Int. 4 (2013) 110–119.

[53] G.W. Bradshaw, C.O. Mathews, Properties of refractory materials, Technical report, LMSD-2466. (1958). https://www.osti.gov/scitech/biblio/4253795

[54] J.P. Moore, R.S. Graves, T.G. Kollie, D.L. McElroy, Thermal conductivity measurements on solids between 20 and 150 C using a comparative longitudinal apparatus, Oak Ridge Natl. Lab. Rep. (1967).

[55] M. Murabayashi, Thermal Conductivity of Ceramic Solid Solutions, J. Nucl. Sci. Technol. 7 (1970) 559–563.

[56] C.G.S. Pillai, P. Raj, Thermal conductivity of ThO 2 and Th 0.98 U 0.02 O 2, J. Nucl. Mater. 277 (2000) 116–119.

[57] K. Bakker, E.H.P. Cordfunke, R.J.M. Konings, R.P.C. Schram, Critical evaluation of the thermal properties of Th02 and Th1−yUy02 and a survey of the literature data on Th1−yPuy02, J. Nucl. Mater. 250 (1997) 1–12.

[58] J.C. Weilbacher, Measurement of the thermal diffusivity of mixed uranium plutonium oxides, High Temp High Press. 4 (1972).

[59] M.R. Tonks, X.Y. Liu, D. Andersson, D. Perez, A. Chernatynskiy, G. Pastore, C.R. Stanek, R. Williamson, Development of a multiscale thermal conductivity model for fission gas in UO2, J. Nucl. Mater. 469 (2016) 89–98.

[60] H. Kleykamp, The chemical state of the fission products in oxide fuels, J. Nucl. Mater. 131 (1985) 221–246.

[61] S.C. Middleburgh, D.C. Parfitt, R.W. Grimes, B. Dorado, M. Bertolus, P.R. Blair, L. Hallstadius, K. Backman, Solution of trivalent cations into uranium dioxide, J. Nucl. Mater. 420 (2012) 258–261.

[62] H. Kleykamp, J.O. Paschoal, R. Pejsa, F. Thümmler, Composition and structure of fission product precipitates in irradiated oxide fuels: Correlation with phase studies in the Mo-Ru-Rh-Pd and BaO-UO2-ZrO2-MoO2 Systems, J. Nucl. Mater. 130 (1985) 426–433.

[63] M.W.D. Cooper, S.C. Middleburgh, R.W. Grimes, Swelling due to the partition of soluble fission products between the grey phase and uranium dioxide, Prog. Nucl. Energy. 72 (2014) 33–37.

[64] K.A. Romberger, C.F.J. Baes, H.H. Stone, Phase equilibrium studies in the UO2-ZrO2 system, J. Inorg. Nucl. Chem. 29 (1967) 1619–1630.

[65] A. Jelea, M. Colbert, F. Ribeiro, G. Tréglia, R.J.M. Pellenq, An atomistic modelling of the porosity impact on UO2 matrix macroscopic properties, J. Nucl. Mater. 415 (2011) 210–216.

[66] A. Loeb, Thermal Conductivity: VIII, A Theory of Thermal Conductivity of Porous Materials, J. Am. Ceram. Soc. 37 (1954) 96.

[67] M. Murabayashi, Y. Takahashi, T. Mukaibo, Effect of Porosity on the Thermal Conductivity of ThO 2, J. Nucl. Sci. Technol. 6 (1969) 657–662.

[68] C.W. Lee, A. Chernatynskiy, P. Shukla, R.E. Stoller, S.B. Sinnott, S.R. Phillpot, Effect of pores and He bubbles on the thermal transport properties of UO2 by molecular dynamics simulation, J. Nucl. Mater. 456 (2015) 253–259.

[69] M. Allen, Introduction to molecular dynamics simulation, Comput. Soft Matter. 23 (2004) 1–28.

[70] L. Verlet, Computer Experiments on Classical Fluids. I. Thermodynamical Properties of Lennard-Jones Molecules, Phys. Rev. 159 (1967) 98–103.

[71] Umaine, Theory of molecular dynamics simulations, (2017) 1–9. http:/chemistry.umeche.maine.edu/CHY431/MolDyn2.html.

[72] R.K. Siripurapu, Molecular Dynamics Study of Zirconium and Zirconium Hydride, University of Sascatchewan, Msc Thesis. (2013).

[73] M.S. Daw, M.I. Baskes, Embedded-atom method: Derivation and application to impurities,

surfaces, and other defects in metals, Phys. Rev. B. 29 (1984) 6443–6453.

[74] M.S. Daw, S.M. Foiles, M.I. Baskes, The Embedded-Atom Method - A Review of Theory and Applications, Mater. Sci. Reports. 9 (1993) 251–310.

[75] M.W.D. Cooper, M.J.D. Rushton, R.W. Grimes, A many-body potential approach to modelling the thermomechanical properties of actinide oxides, J. Phys. Condens. Matter. 26 (2014) 105401.

[76] M.J. Qin, M.W.D. Cooper, E.Y. Kuo, M.J.D. Rushton, R.W. Grimes, G.R. Lumpkin, S.C. Middleburgh, Thermal conductivity and energetic recoils in UO2 using a many-body potential model, J. Phys. Condens. Matter. 26 (2014) 495401.

[77] S.N. Laboratories, LAMMPS Users Manual, J. Infect. Dis. 209 (2014).

[78] MeDeA, MedeA LAMMPS, Mater. Des. (2009) 87501.

[79] J.D. Gale, General Utility Lattice Program - Manual, Dep. Chem. Curtin Univ. Technol. (2012) 148.

[80] R.A. Serway, J.W. Jewett, Physics for Scientists and Engineers with Modern, Chapters 1-46, Cengage Learning, 2009.

[81] S.G. Popov, V.K. Ivanov, J.J. Carbajo, G.L. Yoder, Thermophysicial Properties of MOX and UO2 Fuels Including the Effects of Irradiation, ORNL. 0 (2000) 9–12.

[82] L. Shi, E. Vathonne, M. Freyss, M. Bertolus, V. Oison, R. Hayn, First-principles study of point defects in cerium dioxide and comparison to uranium dioxide, MRS Proc. 1743 (2015).

[83] Z.W. Niu, Y. Cheng, H.-Y. Zhang, G.F. Ji, First-Principles Investigations on Structural, Phonon, and Thermodynamic Properties of Cubic CeO2, Int. J. Thermophys. 35 (2014) 1601–1612.

[84] S. M. Woodley, P. D. Battle, J. D. Gale, C. Richard A. Catlow, The prediction of inorganic crystal structures using a genetic algorithm and energy minimisation, Phys. Chem. Chem. Phys. 1 (1999) 2535–2542.

[85] Z.-W. Niu, Y. Cheng, H.-Y. Zhang, G.-F. Ji, First-Principles Investigations on Structural,

Phonon, and Thermodynamic Properties of Cubic CeO2, Int. J. Thermophys. 35 (2014) 1601–1612.

[86] S. Nosé, A molecular dynamics method for simulations in the canonical ensemble, Mol. Phys. 52 (1984) 255–268.

[87] S. Nosé, A unified formulation of the constant temperature molecular dynamics methods, J. Chem. Phys. 81 (1984) 511–519.

[88] W.G. Hoover, Canonical dynamics: Equilibrium phase-space distributions, Phys. Rev. A. 31 (1985) 1695–1697.

[89] R. Kubo, M. Toda, N. Hashitsume, Statistical Physics II. Nonequilibrium Statistical Mechanics, 1995. https://link.springer.com/book/10.1007%2F978-3-642-58244-8.

[90] S.J. Duclos, Y.K. Vohra, A.L. Ruoff, A. Jayaraman, G.P. Espinosa, High-pressure x-ray diffraction study of CeO2 to 70 GPa and pressure-induced phase transformation from the fluorite structure, Phys. Rev. B. 38 (1988) 7755–7758.

[91] M. Yashima, D. Ishimura, Y. Yamaguchi, K. Ohoyama, K. Kawachi, High-temperature neutron powder diffraction study of cerium dioxide CeO2 up to 1770 K, Chem. Phys. Lett. 372 (2003) 784–787.

[92] M. Yashima, S. Kobayashi, T. Yasui, Crystal structure and the structural disorder of ceria from 40^{o}C to 1497 °C, Solid State Ionics. 177 (2006) 211–215.

[93] M.W.D. Cooper, N. Kuganathan, P.A. Burr, M.J.D. Rushton, R.W. Grimes, C.R. Stanek, D.A. Andersson, Development of Xe and Kr empirical potentials for CeO2, ThO2, UO2 and PuO2, combining DFT with high temperature MD, J. Phys. Condens. Matter. 28 (2016) 405401.

[94] S. Hirano, K.E.N. Hirota, O. Yamaguchi, Solid solutions of metastable tetragonal Zr02 and Ce3ZrO8 in the system ZrO2-Ce02, 31 (1996) 4945–4949.

[95] Y. Chiang, E.B. Lavik, I. Kosacki, H.L. Tuller, J.Y. Ying, Defect and transport properties of nanocrystalline CeO 2-x, Appl. Phys. Lett. 69 (1996) 185–187.

[96] R. Podor, N. Clavier, J. Ravaux, L. Claparede, N. Dacheux, D. Bernache-Assollant,

Dynamic aspects of cerium dioxide sintering: HT-ESEM study of grain growth and pore elimination, J. Eur. Ceram. Soc. 32 (2012) 353–362.

[97] K.R. Lee, J.H. Lee, H.I. Yoo, Grain size effect on the electrical properties of nanocrystalline ceria, J. Eur. Ceram. Soc. 34 (2014) 2363–2370.

[98] M. Coster, X. Arnould, J.L. Chermant, L. Chermant, T. Chartier, The use of image analysis for sintering investigations: The example of CeO2 doped with TiO2, J. Eur. Ceram. Soc. 25 (2005) 3427–3435.

[99] T. Zhang, P. Hing, H. Huang, J. Kilner, Sintering study on commercial CeO2 powder with small amount of MnO2 doping, Mater. Lett. 57 (2002) 507–512.

APPENDIX 1

The research reported in this thesis is a result of collaboration between the author, Dotun J. Oladimeji, supervisor Dr. Barbara Szpunar of the Department of Physics and Engineering Physics and co-supervisor Prof. Jerzy Szpunar of the Department of Mechanical Engineering at the University of Saskatchewan. Other works listed below have also been performed, but are not included in this thesis.

1. **D. Oladimeji**, L. Malakkal, B. Szpunar, E. Jossou, J. A. Szpunar "First principles study of thermo-mechanical properties of gallium phosphide" International Journal of Metallurgy and Metal Physics, 2017. (Under Review)
2. E. Jossou, L. Malakkal, B. Szpunar, **D. Oladimeji**, J.A. Szpunar, A first principles study of the electronic structure, elastic and thermal properties of UB2, J. Nucl. Mater. 490 (2017) 41–48.
3. E. Jossou, **D. Oladimeji**, L. Malakkal, S. Middleburgh, B. Szpunar, J.A. Szpunar, First-principle study of defects and fission product behaviour in uranium diboride, J. Nucl. Mater. 494 (2017) 147–156.
4. B. Szpunar, L. Malakkal, J. C. Zuniga, R. K. Siripurapu, **D. Oladimeji**, J. A. Szpunar" Safer Nuclear Reactors with Enhanced Thermal Conductivity for Clean Energy". Presented at the 14th International Conference on Clean Energy 2015 (ICCE-2015), Published.
5. E. E. Jossou, **D. J. Oladimeji,** J. I. Ranasinghe, L. Malakkal, B. Szpunar, J. A. Szpunar "First Principle Studies of Electronics Structure of U3O8" Poster presented at 23rd International WIEN2K Workshop, June 3rd -7th, 2016, Hamilton, Canada.
6. B. Szpunar, L. Malakkal, E. Jossou, **D. Oladimeji,** J. Ranasinghe, I. Rossland, J. A. Szpunar" First Principle Studies of Thermal Conductivity of Nuclear Fuel Materials**".** Presented at the 13th International Conference on CANDU Fuel August 15th -18th, 2016, Kingston, Canada, Published.
7. E. Jossou, L. Malakkal, **D. Oladimeji**, B. Szpunar, J. A. Szpunar "First Principles Study of Electronic Structure and Thermal Properties of Accident Tolerant Nuclear Fuel: UO2 and UB2" Presented at the 2017 TMS Annual Meeting & Exhibition, February 26th – March 3rd, 2017, San Diego, CA, USA.

APPENDIX 2

All the results presented in this thesis are stored in the computer Canada storage computer (dtn.sfu.computecanada.ca) with descriptions for future reference. The results and python script used in the calculations involving thermal expansion and thermal conductivity are stored in the same folder with a readme file with descriptions. The location of all results is provided.

1. **Location of results on computer Canada storage computer (**dtn.sfu.computecanada.ca)

Thermal conductivity results of CeO_2 with and without defect are stored in **/home/dotway/wg-jerzy/data/Dotun/ceria/Conductivity** and the list of folders in the directory is provided below with the name of each folder corresponding to percentage defect:

drwxr-xr-x. 3 dotway dotway 4096 May 8 15:07 **1%Kr**

drwxr-sr-x. 3 dotway wg-jerzy 4096 May 10 11:02 **1%Porosity**

drwxr-xr-x. 3 dotway dotway 4096 May 8 15:08 **1%Xe**

drwxr-sr-x. 3 dotway wg-jerzy 4096 May 10 11:02 **2%Porosity**

drwxr-sr-x. 3 dotway wg-jerzy 4096 May 10 11:02 **3%Porosity**

drwxr-sr-x. 3 dotway wg-jerzy 4096 May 10 11:02 **4%Porosity**

drwxr-xr-x. 4 dotway dotway 4096 May 8 15:08 **5%Kr**

drwxr-sr-x. 15 dotway wg-jerzy 4096 Feb 5 14:54 **5%Porosity**

drwxr-xr-x. 3 dotway dotway 4096 Feb 5 14:50 **CeriaZirconia**

drwxr-sr-x. 4 dotway wg-jerzy 4096 Feb 5 14:54 **DefectFree**

Thermal expansion results of CeO_2 is stored in **/home/dotway/wg-jerzy/data/Dotun/ceria/Expansion** and the list folders in the directory is provided below:

drwxr-sr-x. 18 dotway wg-jerzy 4096 May 10 12:00 **Lattice**

drwxr-sr-x. 18 dotway wg-jerzy 4096 May 10 12:01 **Volume**

The Oxygen diffusion results of CeO_2 is stored in **/home/dotway/wg-jerzy/data/Dotun/ceria/Diffusion/O_Diff** and the list folders in the directory is provided below:

drwxr-sr-x. 2 dotway wg-jerzy 4096 May 10 12:07 **1000K**

drwxr-sr-x. 2 dotway wg-jerzy 4096 May 10 12:07 **1200K**

drwxr-sr-x. 2 dotway wg-jerzy 4096 May 10 12:07 **1400K**

drwxr-sr-x. 2 dotway wg-jerzy 4096 May 10 12:07 **1600K**

drwxr-sr-x. 2 dotway wg-jerzy 4096 May 10 12:07 **1800K**

drwxr-sr-x. 2 dotway wg-jerzy 4096 May 8 15:01 **2000K**

drwxr-sr-x. 2 dotway wg-jerzy 4096 May 8 15:01 **2200K**

drwxr-sr-x. 2 dotway wg-jerzy 4096 May 8 15:01 **2400K**

drwxr-sr-x. 2 dotway wg-jerzy 4096 May 8 15:01 **2600K**

drwxr-sr-x. 2 dotway wg-jerzy 4096 May 10 12:07 **400K**

drwxr-sr-x. 2 dotway wg-jerzy 4096 May 10 12:07 **600K**

drwxr-sr-x. 2 dotway wg-jerzy 4096 May 10 12:07 **800K**

All the notebooks used in the process of calculations involving CeO_2 are store in **/home/dotway/wg-jerzy/data/Dotun/ceria/notebooks** and the list of the notebooks in the directory is provided below:

-rw-r--r--. 1 dotway wg-jerzy 13812 Dec 30 21:45 **1%Kr.ipynb**

-rw-r--r--. 1 dotway wg-jerzy 39418 Dec 21 12:43 **1%Porosity.ipynb**

-rw-r--r--. 1 dotway wg-jerzy 13812 Dec 30 21:46 **1%Xe.ipynb**

-rw-r--r--. 1 dotway wg-jerzy 39418 Dec 21 12:49 **2%Porosity.ipynb**

-rw-r--r--. 1 dotway wg-jerzy 39418 Dec 21 12:56 **3%Porosity.ipynb**

-rw-r--r--. 1 dotway wg-jerzy 39418 Dec 21 12:58 **4%Porosity.ipynb**

-rw-r--r--. 1 dotway wg-jerzy 13623 Dec 30 21:42 **5%Kr.ipynb**

-rw-r--r--. 1 dotway wg-jerzy 43263 Sep 21 2016 **5%Porosity.ipynb**

-rw-r--r--. 1 dotway wg-jerzy 37363 Nov 6 2015 **ceriaukltc2.ipynb**

-rw-r--r--. 1 dotway wg-jerzy 37408 Nov 6 2015 **ceriaukvol2.ipynb**

-rw-r--r--. 1 dotway wg-jerzy 39564 May 23 2016 **DefectFree.ipynb**

All results from GaP calculations are store in /**home/dotway/wg-jerzy/data/Dotun/GaP/calc** and the list of folders are presented below.

drwxr-sr-x. 3 dotway wg-jerzy 4096 May 10 10:13 **Gap-Elect**

drwxr-sr-x. 2 dotway wg-jerzy 4096 May 10 10:13 **GaP-LatDyn.Lgv7CR**

drwxr-sr-x. 270 dotway wg-jerzy 4096 May 10 10:21 **QHA**

drwxr-sr-x. 2 dotway wg-jerzy 4096 May 10 10:21 **SGaP-elastic.40GVuw**

drwxr-sr-x. 2 dotway wg-jerzy 4096 May 10 10:21 **SGaP-structure.605itU**

drwxr-sr-x. 2 dotway wg-jerzy 4096 May 10 10:22 **SGaP-structure.BPWF0w**

drwxr-sr-x. 2 dotway wg-jerzy 4096 May 10 10:22 **SGaP-structure.hnzLh7**

drwxr-sr-x. 2 dotway wg-jerzy 4096 May 10 10:22 **SGaP-structure.WbaMzo**

drwxr-sr-x. 2 dotway wg-jerzy 4096 May 10 10:22 **SGaP-structure.WbMho2**

drwxr-sr-x. 2 dotway wg-jerzy 4096 May 10 10:22 **SGaP-structure.yN4g93**

All the ipython notebooks of the GaP calculations are stored in **/home/dotway/wg-jerzy/data/Dotun/GaP/notebook** and the list of files is presented below.

-rw-r--r--. 1 dotway wg-jerzy 110736 Mar 22 2016 **Crystal_structure_advanced0-100101010.ipynb**

-rw-r--r--. 1 dotway wg-jerzy 46860 Mar 22 2016 **Elastic_constants_loc_full_advanced0.ipynb**

-rw-r--r--. 1 dotway wg-jerzy 31718 Mar 22 2016 **Electronic_structure.ipynb**

-rw-r--r--. 1 dotway wg-jerzy 161887 Mar 22 2016 **PHONONLattice_dynamics_advanced - Copy.ipynb**

-rw-r--r--. 1 dotway wg-jerzy 161887 Mar 22 2016 **PHONONLattice_dynamics_advanced.ipynb**

-rw-r--r--. 1 dotway wg-jerzy 592308 Apr 7 2016 **QHA-example_advanced-5kpoint.ipynb**

2. Description of LAMMPS input scripts

All the scripts used for LAMMPS molecular dynamic calculations are presented and described herein. Also, the input script, generated by MedeA, used in diffusion calculations is provided here. The scripts were run on westgrid computers and University of Saskatchewan super computer (Plato).

- **LAMMPS script for variation of lattice parameters with temperature (thermal expansion) calculation**

The thermal expansion script is labeled accordingly as it performs each stage of calculation. The first stage is the initialization stage, where the boundary condition is set to be periodic with metal units and atomic style full is applied to study CeO_2. The next stage describes the atomic configuration where the CeO_2 structure is imported from a separate structure.u file after which types and charges are assigned to the atoms in the structure. The interatomic potential is imported and described in the next stage as coulumbic and embedded atom method. The structure is first minimized at the minimization stage to achieve the lattice parameter at the lowest energy possible. The structure is the replicated after minimization stage and the temperature is raised to the desired level to study the variation of lattice parameters with temperature. The pressure along each direction is set to 0 atm and the temperature used in the script below is 300 K. Initial velocity is chosen like the temperature required and any angular momentum is removed. Thermodynamic variables which were outputted are temperature, pressure, volume, their values are used to check for convergence and lx, ly and lz box lengths are used to calculate lattice parameters.

#Sample script to calculate lattice parameters at different temperatures

```
# ---------- Initialization ----------
units metal
boundary p p p
atom_style full
# ---------- Atomic configuration ----------
read_data /global/scratch/dotway/lammps/python/structure.u
# import CeO2 single cell fluorite structure and assign atom labels
group Ce type 2
group O type 1
# set charges
set type 2 charge 2.2208
set type 1 charge -1.1104
# ---------- Interatomic potential ----------
# define interatomic potential via coulombic and embed tabulation
kspace_style pppm 1.0e-5
variable SR_CUTOFF equal 11.0
pair_style hybrid/overlay coul/long ${SR_CUTOFF} eam/alloy
pair_coeff   *    *    coul/long
pair_coeff   *    *    eam/alloy /global/scratch/dotway/lammps/python/CeThUNpPuAmCmO.eam.alloy O
Ce
#.................Perform minimization.....................
fix boxrelax_fix all box/relax aniso 0.0 vmax 0.001
thermo 1
thermo_style custom step cpu press etotal lx cella cellb cellc cellalpha cellbeta cellgamma
min_style sd
min_modify line quadratic dmax 0.05
minimize 1.0e-25 1.0e-25 1000 10000
unfix boxrelax_fix
reset_timestep 0
# Create 5x5x5 supercell containing 1500 atoms
replicate 5 5 5
# ---------- Variables to write to LAMMPS output file ----------
variable tstep equal step
variable T equal temp
variable LX equal lx
variable LY equal ly
variable LZ equal lz
variable nAtoms equal count(all)
# ---------- Log, timestep ----------
thermo 1000
thermo_style custom step temp pe ke etotal lx ly lz pxx pyy pzz pyz pxz pxy
timestep 0.005
neigh_modify delay 0 every 1 check yes
# ---------- Initialize velocity (uniform distribution) ----------#
velocity all create 300.000000 398165
# ---------- Isothermal-isobaric ensemble ----------
fix npt all npt temp 300.000000 300.000000 0.1 aniso 0.0 0.0 0.5
# ---------- Write thermodynamic information to file during run----------
fix print_thermo all print 100 "${tstep} ${T} ${LX} ${LY} ${LZ}" append thermo.log
fix print_nAtoms all print 50000 "${nAtoms}" append nAtoms.txt
run 50000
```

- **LAMMPS script for thermal conductivity as a function of temperature calculation**

Complex problems like the thermal conductivity of CeO_2 as a function of temperature is calculated using the equilibrium molecular dynamic with Green-Kubo formalism. The LAMMPS units are first converted to SI units after the initialization stage. The script equilibrates CeO_2 structure using the NPT ensemble after completing the preliminary stages (initialization and minimization). The thermalization and equilibration stage is the process where the temperature of the system is raised to the desired level and before using the NPT and NVT ensemble to equilibrate the system. The system is equilibrated for a long period of time to achieve a well-optimized system before thermal conductivity calculation is started. The thermal conductivity is started after the NVT run is finished and the HCACFs were computed along with an NVE ensemble calculation which generates a 12500 ps raw heat current data at every calculation. The thermal conductivity value in the x, y, and z-direction are evaluated from the heat current data. The average thermal conductivity is outputted and printed at the end of the script.

```
# Sample LAMMPS input script for thermal conductivity of Ceria

# ---------- Initialization ----------
boundary     p p p
atom_style   full
units        metal
variable     T equal 300.000000
variable     V equal vol
variable     dt equal 0.005
variable     p equal 100     # correlation length
variable     s equal 10      # sample interval
variable     d equal $p*$s   # dump interval
# convert from LAMMPS metal units to SI
variable     kB equal 1.3806504e-23    # [J/K] Boltzmann
variable     kCal2J equal 1.6021765e-19
variable     A2m equal 1.0e-10
variable     ps2s equal 1.0e-12
variable     convert equal ${kCal2J}*${kCal2J}/${ps2s}/${A2m}
# ---------- Atomic configuration ----------
read_data        /home/dotway/lammps/python/structure.u
group   Ce type 2
group   O type 1
# set charges
set     type 2 charge 2.2208
```

```
set     type 1 charge -1.1104
replicate      8 8 8
# ---------- Interatomic potential ----------
kspace_style     pppm 1.0e-5
variable         SR_CUTOFF equal 11.0
pair_style       hybrid/overlay coul/long ${SR_CUTOFF} eam/alloy
pair_coeff   *    *    coul/long
pair_coeff   *    *    eam/alloy /home/dotway/lammps/python/CeThUNpPuAmCmO.eam.alloy O Ce
neigh_modify     delay 0 every 1 check yes
#.....Perform minimization.....
fix boxrelax_fix all box/relax aniso 0.0 vmax 0.001
thermo 1
thermo_style custom step cpu press etotal lx cella cellb cellc cellalpha cellbeta cellgamma
min_style sd
min_modify line quadratic dmax 0.05
# ---------- Dump coordinates ----------
dump 1 all custom 100 ceria.coordinate id type x y z
dump_modify 1 every 100000
minimize 1.0e-25 1.0e-25 1000 10000
unfix boxrelax_fix
reset_timestep 0
# equilibration and thermalization
velocity     all create $T 160278
fix          1 all npt temp $T $T 0.1 aniso 0.0 0.0 0.9
timestep     ${dt}
thermo         $d
thermo_style custom step temp pe lx ly lz press pxx pyy pzz
run          500000
unfix        1
fix          NVT all nvt temp $T $T 0.01 drag 0.2
run          500000
# thermal conductivity calculation, switch to NVE if desired
#unfix       NVT
#fix         NVE all nve
reset_timestep 0
compute      myKE all ke/atom
compute      myPE all pe/atom
compute      myStress all stress/atom NULL virial
compute      flux all heat/flux myKE myPE myStress
variable     Jx equal c_flux[1]/vol
variable     Jy equal c_flux[2]/vol
variable     Jz equal c_flux[3]/vol
fix          JJ all ave/correlate $s $p $d &
c_flux[1] c_flux[2] c_flux[3] type auto file J0Jt.dat ave running
variable     scale equal ${convert}/${kB}/$T/$T/$V*$s*${dt}
variable     k11 equal trap(f_JJ[3])*${scale}
variable     k22 equal trap(f_JJ[4])*${scale}
variable     k33 equal trap(f_JJ[5])*${scale}
thermo_style custom step temp v_Jx v_Jy v_Jz v_k11 v_k22 v_k33
run 1500000
variable     k equal (v_k11+v_k22+v_k33)/3.0
```

```
variable    ndens equal count(all)/vol
print       "average conductivity: $k[W/mK] @ $T K, ${ndens} /A^3"
print       $k append conductivity.txt
```

- **Mean Square Displacement script used for Oxygen diffusion calculation**

The MedeA software writes the input script with appropriate labeling. The first stage of the script is the initialization stage where units, structure file, variables and potential file are assigned. Also, the subset of all atoms in the structure is created to be able to monitor the movements of atoms during calculations. The next stage describes the custom code where the many-body potential is properly expressed for interactions of atoms. The structure is minimized after the custom stage to obtain the lattice parameter at the minimum energy. Initial velocity is set for the system and NPT ensemble is invoked after the minimization stage. The temperature of the system rises using the NPT ensemble and the system is allowed to equilibrate for long period of time before diffusion integration starts for the specified group of atoms.

```
#  This is the control script for LAMMPS

echo                            both
log                     3.1_Initialize.out

#-----------------------------------------------------------------------------
# Stage 3.1: Initialize LAMMPS run for 3-d periodic
#-----------------------------------------------------------------------------

units                           metal
neighbor                2.0 bin
neigh_modify                    delay 0 every 1 check yes
boundary                p p p
atom_style              full


box             tilt large
read_data               structure.dat

pair_style              eam/alloy
pair_coeff              * * parameters.dat Ce O

variable                R                       equal 8.6173844e-05
variable                sysvol                  equal vol
variable                sysmass                 equal mass(all)/6.0221367e+23
variable                sysdensity      equal v_sysmass/v_sysvol/1.0e-24
variable                coulomb                 equal ecoul+elong
variable                etotal                  equal etotal
variable                pe                      equal pe
variable                ke                      equal ke
variable                evdwl                   equal evdwl
variable                epair                   equal epair
variable                ebond                   equal ebond
```

```
variable                eangle                  equal eangle
variable                edihed                  equal edihed
variable                eimp                    equal eimp
variable                lx                      equal lx
variable                ly                      equal ly
variable                lz                      equal lz
variable                Nthermo                 equal 0
variable                cella                   equal lx
variable                cellb                   equal sqrt(ly*ly+xy*xy)
variable                cellc                   equal sqrt(lz*lz+xz*xz+yz*yz)
variable                cellalpha       equal acos((xy*xz+ly*yz)/(v_cellb*v_cellc))
variable                cellbeta        equal acos(xz/v_cellc)
variable                cellgamma       equal acos(xy/v_cellb)
variable                p                       equal press
variable                pxx                     equal pxx
variable                pyy                     equal pyy
variable                pzz                     equal pzz
variable                pyz                     equal pyz
variable                pxz                     equal pxz
variable                pxy                     equal pxy
variable                sxx                     equal -pxx
variable                syy                     equal -pyy
variable                szz                     equal -pzz
variable                syz                     equal -pyz
variable                sxz                     equal -pxz
variable                sxy                     equal -pxy
variable                fmax                    equal fmax
variable        fnorm           equal fnorm
variable                time equal step*dt+0.000001
variable                surfacetension equal 0.5*v_lz*(0.5*(v_sxx+v_syy)-v_szz)

thermo_style            custom step v_time press vol v_sysdensity temp ebond eangle edihed eimp evdwl ecoul etail elong pe
ke
thermo_modify                   flush yes


#
# Set up the fixed and movable groups
#

group                   movable union all
group                   fixed subtract all movable

#
# Subsets
#

group                   subset_Ce id 1 2 3 4 13 14 15 16 25 26
group                   subset_Ce id 27 28 37 38 39 40 49 50 51 52
group                   subset_Ce id ……..
……..
……..
group                   subset_Ce id 6061 6062 6063 6064 6073 6074 6075 6076 6085 6086
group                   subset_Ce id 6087 6088 6097 6098 6099 6100 6109 6110 6111 6112
group                   subset_Ce id 6121 6122 6123 6124 6133 6134 6135 6136

group                   subset_O id 5 6 7 8 9 10 11 12 17 18
group                   subset_O id 19 20 21 22 23 24 29 30 31 32
group                   subset_O id ……..
……..
……..
```

```
group                   subset_O id 6033 6034 6035 6036 6041 6042 6043 6044 6045 6046
group                   subset_O id 6047 6048 6053 6054 6055 6056 6057 6058 6059 6060
group                   subset_O id 6065 6066 6067 6068 6069 6070 6071 6072 6077 6078
group                   subset_O id 6079 6080 6081 6082 6083 6084 6089 6090 6091 6092
group                   subset_O id 6093 6094 6095 6096 6101 6102 6103 6104 6105 6106
group                   subset_O id 6107 6108 6113 6114 6115 6116 6117 6118 6119 6120
group                   subset_O id 6125 6126 6127 6128 6129 6130 6131 6132 6137 6138
group                   subset_O id 6139 6140 6141 6142 6143 6144

log                     3.2_Custom.out
#-------------------------------------------------------------------------------
# Stage 3.2: Additional lines require for coul/long
#-------------------------------------------------------------------------------

kspace_style            pppm 1.0e-5
pair_style              hybrid/overlay coul/long 11 eam/alloy
pair_coeff    *         *             coul/long
pair_coeff    *         *             eam/alloy parameters.dat Ce O

log                     3.3_Minimization.out
#-------------------------------------------------------------------------------
# Stage 3.3: Minimization
#-------------------------------------------------------------------------------

min_style               cg
min_modify              dmax 0.05 line quadratic
reset_timestep                  0
thermo_style            custom step fmax fnorm press vol v_sysdensity v_sxx v_syy v_szz v_syz v_sxz v_sxy pe v_cella
v_cellb v_cellc v_cellalpha v_cellbeta v_cellgamma
fix                             3_3_1 all box/relax iso 0.000 vmax 0.01 dilate all
dump                            sci all custom 100000 3.3.xyz id mol type q xs ys zs
thermo                          100
dump                            trj all custom 100 3.3.Trajectory.xyz id mol type q xs ys zs
fix                             3_3_2 fixed setforce 0.0 0.0 0.0
minimize                0.0 1.0 100000 1000000
undump                          trj

undump                          sci
unfix                   3_3_2
unfix                           3_3_1

log                     3.4_Velocities.out
#-------------------------------------------------------------------------------
# Stage 3.4: Set the initial velocities for $T
#-------------------------------------------------------------------------------

velocity                all create 2600 72489 dist gaussian mom yes rot no

log                     3.5_NPT.out
#-------------------------------------------------------------------------------
# Stage 3.5: NPT integration for 500000 steps with a timestep of 0.005 ps
#         Temperature 2600 K
#         Pressure 0 atm
#-------------------------------------------------------------------------------

reset_timestep                  0
thermo_style            custom step v_time press vol v_sysdensity temp ebond eangle edihed eimp evdwl ecoul etail elong pe
ke
thermo                          ${Nthermo}
fix                             1 movable npt temp 2600 2600 0.1 iso 0 0 1 drag 0 mtk yes nreset 10000
```

```
fix                             2 movable ave/time 1 49999 50000 v_time c_thermo_temp c_thermo_press v_sysvol
v_sysdensity v_etotal v_cella v_cellb v_cellc v_cellalpha v_cellbeta v_cellgamma v_pe v_ke v_evdwl v_coulomb v_sxx v_syy
v_szz v_syz v_sxz v_sxy file 3.5_averages.txt off 1
fix                             3 movable ave/time 200  1     200 v_time  c_thermo_temp c_thermo_press v_sysvol
v_sysdensity v_etotal v_cella v_cellb v_cellc v_cellalpha v_cellbeta v_cellgamma v_pe v_ke v_evdwl v_coulomb v_sxx v_syy
v_szz v_syz v_sxz v_sxy file 3.5_instantaneous.txt off 1
restart                         500000 3.5.restart
dump                            trj all custom 100 3.5.Trajectory.xyz id mol type q xs ys zs
fix                             trjE all ave/time 100 1 100 v_etotal v_pe v_ke file 3.5.energies.txt

timestep        0.005
run                             500000
undump                          trj
unfix                           trjE

restart                         0
dump                            sci all custom 500000 3.5.xyz id mol type q xs ys zs
run                             0
undump                          sci


unfix                           1
unfix                           2
unfix                           3

log             3.6_Diffusion.out
#---------------------------------------------------------------------------
# Stage 3.6: Diffusion integration for 1500000 steps with a timestep of 0.005 ps
#---------------------------------------------------------------------------

reset_timestep                  0

group           msdGroup id     5    6    7    8    9   10   11   12
group           msdGroup id    17   18   19   20   21   22   23   24
group           msdGroup id    29   30   31   32   33   34   35   36
group           msdGroup id    41   42   43   44   45   46   47   48
group           msdGroup id    53   54   55   56   57   58   59   60
group           msdGroup id    65   66   67   68   69   70   71   72
group           msdGroup id    77   78   79   80   81   82   83   84
group           msdGroup id    ……...
……
group           msdGroup id  6101 6102 6103 6104 6105 6106 6107 6108
group           msdGroup id  6113 6114 6115 6116 6117 6118 6119 6120
group           msdGroup id  6125 6126 6127 6128 6129 6130 6131 6132
group           msdGroup id  6137 6138 6139 6140 6141 6142 6143 6144


thermo_style    custom step v_time press vol v_sysdensity temp ebond eangle edihed eimp evdwl ecoul etail elong pe
ke
thermo                          ${Nthermo}
compute                         msdData msdGroup msd
fix                             1 movable nve
fix                             2 movable ave/time 1 150000 150000 v_time c_thermo_temp c_thermo_press v_sysvol
v_sysdensity v_etotal v_pe v_ke v_evdwl v_coulomb file 3.6_averages.txt
fix                             3 movable ave/time 1000  1     1000 v_time  c_thermo_temp c_thermo_press v_sysvol
v_sysdensity v_etotal v_pe v_ke v_evdwl v_coulomb file 3.6_instantaneous.txt
fix                             4 movable ave/time 1000  1     1000 c_msdData[1] c_msdData[2] c_msdData[3]
c_msdData[4] file 3.6_msd.txt
restart                         1500000 3.6.restart
dump                            trj all custom 1000 3.6.Trajectory.xyz id mol type q xs ys zs
fix                             trjE all ave/time 1000 1 1000 v_etotal v_pe v_ke file 3.6.energies.txt
timestep        0.005
```

```
run             1500000
undump          trj
unfix           trjE

restart         0
dump            sci all custom 1500000 3.6.xyz id mol type q xs ys zs
run             0
undump          sci
unfix           1
unfix           2
unfix           3
unfix           4
```

PERMISSIONS

Figure 2.3 is partly reprinted with the permission from Y. Lu, Y. Yang, P. Zhang, J. Phys. Condens. Matter. 24 (2012) 225801. Copyright 2012 by the Journal of Physics: Condensed Matter.

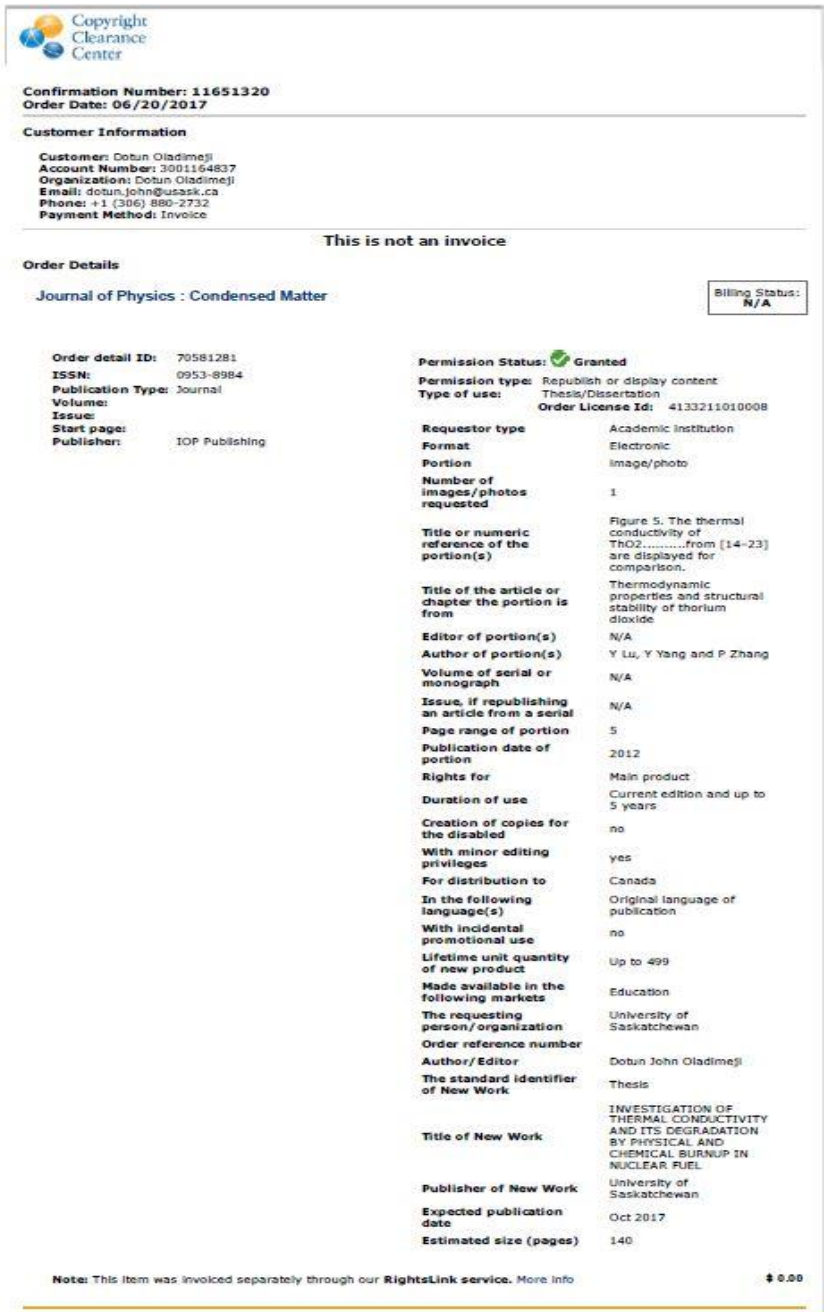

Copyright Clearance Center

Confirmation Number: 11651320
Order Date: 06/20/2017

Customer Information

Customer: Dotun Oladimeji
Account Number: 3001164837
Organization: Dotun Oladimeji
Email: dotun.john@usask.ca
Phone: +1 (306) 880-2732
Payment Method: Invoice

This is not an invoice

Order Details

Journal of Physics : Condensed Matter

Billing Status: N/A

Order detail ID:	70581281
ISSN:	0953-8984
Publication Type:	Journal
Volume:	
Issue:	
Start page:	
Publisher:	IOP Publishing

Permission Status: Granted
Permission type: Republish or display content
Type of use: Thesis/Dissertation
Order License Id: 4133211010008

Requestor type	Academic institution
Format	Electronic
Portion	image/photo
Number of images/photos requested	1
Title or numeric reference of the portion(s)	Figure 5. The thermal conductivity of ThO2.....from [14-23] are displayed for comparison.
Title of the article or chapter the portion is from	Thermodynamic properties and structural stability of thorium dioxide
Editor of portion(s)	N/A
Author of portion(s)	Y Lu, Y Yang and P Zhang
Volume of serial or monograph	N/A
Issue, if republishing an article from a serial	N/A
Page range of portion	5
Publication date of portion	2012
Rights for	Main product
Duration of use	Current edition and up to 5 years
Creation of copies for the disabled	no
With minor editing privileges	yes
For distribution to	Canada
In the following language(s)	Original language of publication
With incidental promotional use	no
Lifetime unit quantity of new product	Up to 499
Made available in the following markets	Education
The requesting person/organization	University of Saskatchewan
Order reference number	
Author/Editor	Dotun John Oladimeji
The standard identifier of New Work	Thesis
Title of New Work	INVESTIGATION OF THERMAL CONDUCTIVITY AND ITS DEGRADATION BY PHYSICAL AND CHEMICAL BURNUP IN NUCLEAR FUEL
Publisher of New Work	University of Saskatchewan
Expected publication date	Oct 2017
Estimated size (pages)	140

Note: This item was invoiced separately through our **RightsLink service.** More info

$ 0.00